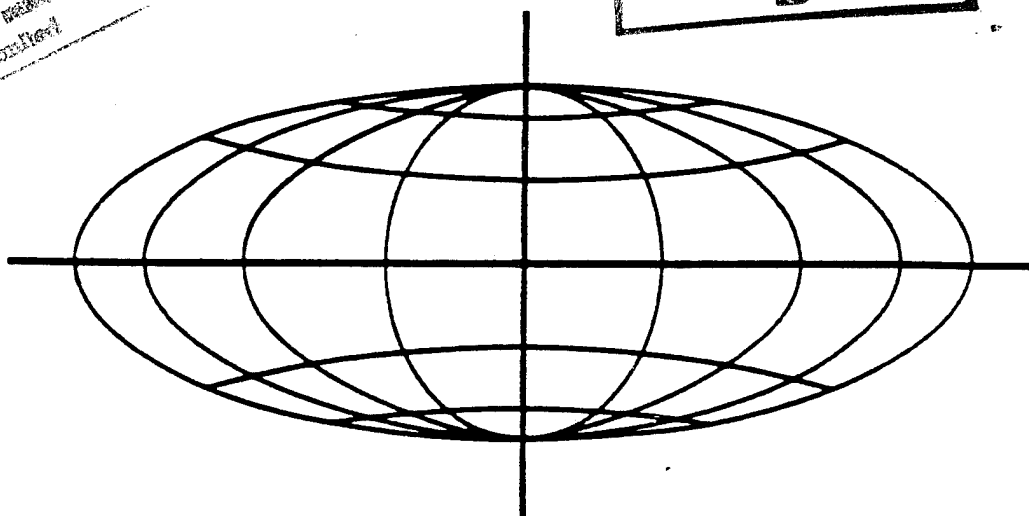
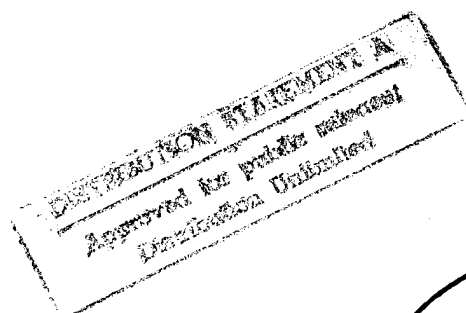
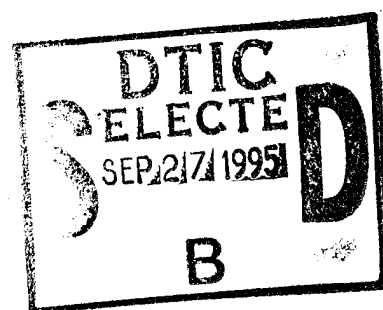


LWIR SUPERCONDUCTING QUANTUM DETECTORS

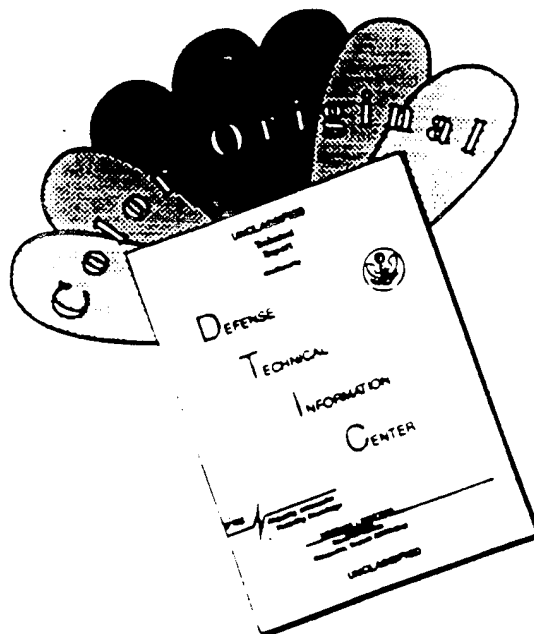


WESTINGHOUSE ELECTRIC CORPORATION
ADVANCED TECHNOLOGY CENTER
WINTERSON & NURSERY RDS.
LINTHICUM, MARYLAND 2190

19950922 083

DTIC QUALITY INSPECTED 5

DISCLAIMER NOTICE



THIS DOCUMENT IS BEST QUALITY AVAILABLE. THE COPY FURNISHED TO DTIC CONTAINED A SIGNIFICANT NUMBER OF COLOR PAGES WHICH DO NOT REPRODUCE LEGIBLY ON BLACK AND WHITE MICROFICHE.

LWIR SUPERCONDUCTING QUANTUM DETECTORS

FINAL REPORT

PERIOD OF PERFORMANCE 6-92 TO 2-95

CONTRACT No. N00014-92-C-2033

AUGUST 1995

AUTHORS

NATHAN BLUZER and MARTIN G. FORRESTER

**PRESENTED TO
DEPARTMENT OF THE NAVY
NAVAL RESEARCH LABORATORIES
WASHINGTON, D.C. 20375**

BY

**WESTINGHOUSE ELECTRIC CORPORATION
ADVANCED TECHNOLOGY CENTER
WINTERSON and NURSERY ROADS
LINTHICUM, MARYLAND 21090**

Unclassified

SECURITY CLASSIFICATION OF THIS PAGE

REPORT DOCUMENTATION PAGE				
1a. Report Security Classification Unclassified		1b. Restrictive Markings None		
2a. Security Classification Authority N/A		3. Distribution/Availability of Report Unlimited		
2b. Declassification/Downgrading Schedule N/A				
4. Performing Organization Report Number (s) N/A		5. Monitoring Organization report Numbers N/A		
6a. Name of Performing Organization Westinghouse Electric Corp.	6b. Office Symbol (If applicable) Elect. Sys. Group	7a. Name of Monitoring Organization None		
6c. Address (City, State and Zip Code) Winterson and Nursery Rd. Linthicum, MD 21090		7b. Address (City, State and Zip Code) N/A		
8a. Name of Funding/Sponsoring Organization Naval Research Laboratory	8b. Office Symbol (If applicable) Code 6830	9. Procurement Instrument Identification Number N00014-92-C-2033		
8c. Address (City, State, and Zip Code) 4555 Overlook Ave. Washington, DC 20375-5347		10. Source of Funding Nos.		
		Program Element No.	Project No.	Task No.
11. Title (Include Security Classification) LWIR Superconducting Quantum Detectors (u)				
12. Personal Author(s) Nathan Bluzer and Martin G. Forrester				
13a. Type of Report Technical, Final	13b. Time Covered 6/92 - 2/95	14. Date of Report (Yr,Mo, Day) August, 1995	15. Page Count 67	
16. Supplementary Notation				
17. Cosatl Codes			18. Subject Terms (Continue on reverse if necessary and identify a block number. Superconductivity, Quantum Detectors	
Field	Group	Sub. Gr.		
19. Abstract (Continue on reverse if necessary and identify by block number. A superconducting Quantum detector has been formulated and analyzed. The detector made in YBCO is based on the change in Kinetic Inductance of the condensate. Analysis projects on $NEP \approx 10^{-17}$ watts/ $\sqrt{\text{Hz}}$ at 9K.				
20. Distribution/Availability of Abstract Unclassified/Unlimited <input checked="" type="checkbox"/> Same as Rpt. <input type="checkbox"/> DTIC Users <input type="checkbox"/>		21. Abstract Security Classification Unclassified		
22a. Name of Responsible Individual Dr. Martin Nisenoff	22b. Telephone Number (Include Area Code) (202) 767-3099	22c. Office Symbol Code 6850		

LWIR SUPERCONDUCTING QUANTUM PHOTODETECTORS

1.0	Executive Summary	1
2.0	Quantum Superconducting Kinetic Inductance Photodetectors	
2.1	Background	3
2.2	Theory of Operations	4
	2.2.1 The QSKIP Energy Minimum	8
	2.2.2 The QSKIP Photoresponse	11
	2.2.2.1 Photocurrent Calculations	11
	2.2.2.2 Photoinduced Quasiparticle Population	13
	2.2.2.3 Effective Quasiparticle Lifetime	16
	2.2.3 Noise Levels in QSKIP	19
	2.2.4 Responsivity and NEP of QSKIP	22
	2.2.5 The NEP of a YBCO QSKIP	23
	2.2.6 Conclusions on QSKIP operation	28
2.3	Detector Fabrication	29
	2.3.1 Magnetically Coupled Detector	30
	2.3.2 Directly Coupled Detector	32
2.4	References	35
3.0	Experimental Approach and Measurements	37
3.1	Optical Setup	37
3.2	Electrical Setup	46
3.3	Cryogenic Setup	53
3.4	Detector Packaging	57

3.5 Detector Testing and Results

62

4.0 Published Papers

4.1 Superconducting Quantum Detectors

4.2 Superconducting Quantum Detectors in YBCO

4.3 Quantum Detectors in Superconducting YBCO

Accession For	
NTIS GRA&I	<input checked="checked" type="checkbox"/>
DTIC TAB	<input type="checkbox"/>
Unannounced	<input type="checkbox"/>
Justification	
By	
Distribution/	
Availability Codes	
Dist	Avail and/or Special
A-1	

1.0 EXECUTIVE SUMMARY

DoD has a need for very sensitive midwave and long wave Infrared photodetectors. It has long been recognized that, theoretically, above 1K quantum photodetectors offer superior performance over thermal photodetectors (bolometers). Accordingly, with the discovery of high temperature superconductivity (HTS) efforts were started to use these new materials for making sensitive midwave and long wave Infrared quantum photodetectors. These efforts reflect the technological difficulty and high cost of making IR photodetectors in semiconductors. Consequently, the expectation is that with superconductor materials more sensitive photodetectors with longer cut-off wavelength will become feasible.

This program was started with the goal of demonstrating Long Wave Infrared quantum photodetectors made in the newly discovered HTS materials. Given the relative immaturity of the HTS field, we encountered many different theoretical and experimental problems and had to formulate many solutions to these.

We have formulated a quantum photodetector based on the kinetic inductance of a superconductor and named it the Quantum Superconducting Kinetic Inductance Photodetector (QSKIP). The performance of this QSKIP is analyzed in section 2.2. The analysis reveals that the QSKIP photoresponse will be limited by the Cooper pair binding energy 2Δ , believed to be about $32\mu\text{m}$, 2Δ of YBCO. The QSKIP photoresponse and sensitivity are computed from the minimum of the Hamiltonian energy functional and *linearized* Rothwarf-Taylor equations. Photoresponse and sensitivity expressions are computed in terms of the quasiparticle lifetime and indicate Background Limited Infrared Performance (BLIP) at very low photon flux levels. At low temperatures and under

BLIP conditions, the photoresponse is proportional to the number of absorbed photons. Operating the QSKIP below H_{C1} and $0.5 J_C$ limits the noise sources to fluctuations in the condensate population. A Noise Equivalent Power estimate for a YBCO QSKIP is about 7×10^{-17} Watts at 9K. These predictions are based on characteristic lifetimes for quasiparticle generation, quasiparticle recombination, anharmonic phonon decay and phonon trapping in a BCS type superconductor.

The QSKIP fabrication is described in section 2.3. The experimental approach and measurements for the QSKIP are presented in section 3.0. To minimize development and fabrication risk, we decided to use a YBCO photodetector with a niobium based SQUID readout circuit. A generic experimental set up was developed for measuring photoresponse of superconducting photodetectors from $1\mu\text{m}$ - $100\mu\text{m}$ over a very wide temperature range (5-300K) and this is presented in section 3.0.

We have measured the characteristics of the Nb SQUID, which operated properly with a critical current of 0.2mA at 5K. The YBCO photodetector material was superconducting at a reduced temperature. The as deposited YBCO had a transition temperature of about 90K and this was reduced to about 60K after the addition of the Niobium SQUID readout circuits. We have investigated the cause of reduction in the transition temperature and concluded that silicon dioxide insulators are leaching oxygen and poisoning the YBCO. Reoxygenation of the YBCO did not recover the 90K transition temperature. It is concluded that the quasiparticle lifetime in the processed YBCO was too degraded to show photoresponse. We are in the process of replacing the silicon dioxide insulator with epitaxial SrTiO_3 . This work is continuing on Westinghouse IR&D with the expectation that the new QSKIP structure will produce the projected performance of about 10^{-17} Watts NEP.

2.0 QUANTUM SUPERCONDUCTING KINETIC INDUCTANCE PHOTODETECTORS

In this chapter we provide a theoretical framework for superconducting quantum photodetectors and introduce a photodetector structure suitable for making superconducting quantum photodetectors.

2.1 BACKGROUND

The pursuit and the development of photodetectors is a very active area of research. This research covers a very broad spectral band, from γ -ray all the way up to very long wave infrared. The operating conditions and performance of photodetectors operating in these bands varies according to the photodetector materials, photodetection method, and the operating spectrum. Of particular interest are photodetectors operating in the midwave 3-5 μm (MWIR) and longwave 8-12 μm (LWIR) infrared spectra. Interest in these spectral bands is large because: (1) the atmosphere is transparent in these spectral bands, and (2) objects at 300K produce significant black body photon radiation in the MWIR and LWIR spectral bands. With a significant black body photon radiation, passive night imaging and target discrimination are possible, making MWIR and LWIR sensor very important for DoD and commercial applications.

Detectors fall into two broad categories:^{1,2} (1) thermal photodetectors and (2) quantum photodetectors. Thermal photodetectors absorb the incident photon flux energy with an optically “black” coating and hence are sensitive over a very broad spectral band. Thermal photodetectors are equilibrium photodetectors where the lattice and the electrons are in thermal equilibrium. The properties of the photodetector are very temperature dependent and photoabsorption produces a temperature change that generates a signal. Quantum photodetectors require an energy quanta to

produce an excitation and the value of this energy quantum translates to photoresponse over a limited spectral band. Quantum photodetectors are nonequilibrium photodetectors where the electrons are not in thermal equilibrium with the lattice. The photodetector properties are not very temperature dependent and photoabsorption produces quantum excitations in the electronic states and thus a photosignal. Theoretically, above 1K, quantum photodetectors are more sensitive than thermal photodetectors because the noise level in quantum photodetectors is smaller. The noise in quantum photodetectors corresponds to Poisson fluctuations in the number of absorbed photons, whereas the noise in thermal photodetectors corresponds to fluctuations in the absorbed energy. This basic difference in noise mechanism can make quantum photodetectors potentially 10^5 more sensitive than thermal photodetectors.

The pursuit of better quantum photodetectors has been an ongoing endeavor and the discovery of High Temperature Superconductivity (HTS) widens the possibilities. Just before the discovery of HTS, Enomoto and Murakami³ made photoresponse measurements on granular $\text{BaPb}_{0.7}\text{Bi}_{0.3}\text{O}_3$, and reported encouraging results. With the discovery of HTS by Bednorz and Muller⁴ in 1986, many proposals were submitted for applying this discovery to MWIR and LWIR photodetectors operating at liquid nitrogen temperatures. More experimental results^{5,6,7} followed reporting on the photoresponse of various HTS photodetector structures. Forrester et al.⁸ showed that the reported photoresponse signals were consistent with a bolometric response, much less sensitive than quantum IR photodetectors.^{1,2} However, because of technological limitations in existing semiconductor based quantum photodetectors, in particular beyond $12\mu\text{m}$, the search for a superior superconducting photodetector persists.^{9,10,11} The cited approaches for realizing superconducting photodetectors have limitations that include poor area efficiency¹¹ (or quantum

efficiency), complicated readout circuits,¹⁰ and speculative photodetection mechanism.⁹ To overcome these limitations, a simple photodetector structure and readout circuit are needed. These issues were addressed in this program and are reported on in this final report.

2.2 THEORY OF OPERATION

We describe a photodetector structure which overcomes the aforementioned limitations and is projected to achieve Background Limited Infrared Performance (BLIP) for very low background radiation, with an NEP of less than 10^{-16} Watts. The quantum photodetector's photoresponse is based on the Cooper pairs' kinetic inductance and hence the label: Quantum Superconducting Kinetic Inductance Photodetector¹² (QSKIP). *This photodetector's photoresponse is sensitive to photoinduced changes in the total Cooper pair population and is unlike Josephson junction based photodetectors that are only sensitive to changes in the condensate population within a coherence distance ξ from the Josephson junction.*

The QSKIP is intended to operate at: (1) low temperatures, (2) low background radiation, (3) below H_{C1} , (4) below $0.5 J_C$, (5) under static nonequilibrium conditions, and (6) not under pulsed laser radiation, as reported in many experiments,^{5,6,7} but modulated at low frequencies ($<100\text{KHz}$). The reasons for choosing such operating conditions are several. In quantum photodetectors, the photoresponse increases with the effective quasiparticle lifetime. The effective quasiparticle lifetime is maximized by operating at low temperature and near thermal equilibrium. The lowest photodetector noise is achieved by operating below H_{C1} and at low temperatures ($T/T_C < 0.1$) because noise from the formation and movement of fluxoids is severely inhibited. Finally, we predict excellent performance for the QSKIP when operating in a low background environment, i.e. detection of cold objects ($< 200\text{K}$) against a cold background ($< 200\text{K}$)

The QSKIP is made from a simple superconducting film patterned into a closed loop with input and output current leads. To facilitate the photoresponse and sensitivity calculation, the QSKIP is represented by a circular loop^{13,14} illustrated in Fig. 2.1. For maximum coupling efficiency and sensitivity, the readout SQUID is directly coupled¹³ with the QSKIP, see Figure 2.2. In operation, the QSKIP is biased by a constant dc current I_0 , $I_0 < 0.5 I_C$. Current I_0 is divided by the QSKIP circuit into currents I_1 and I_2 . With photoabsorption, the division of I_0 into I_1 and I_2 changes and this change represents the QSKIP photoresponse.

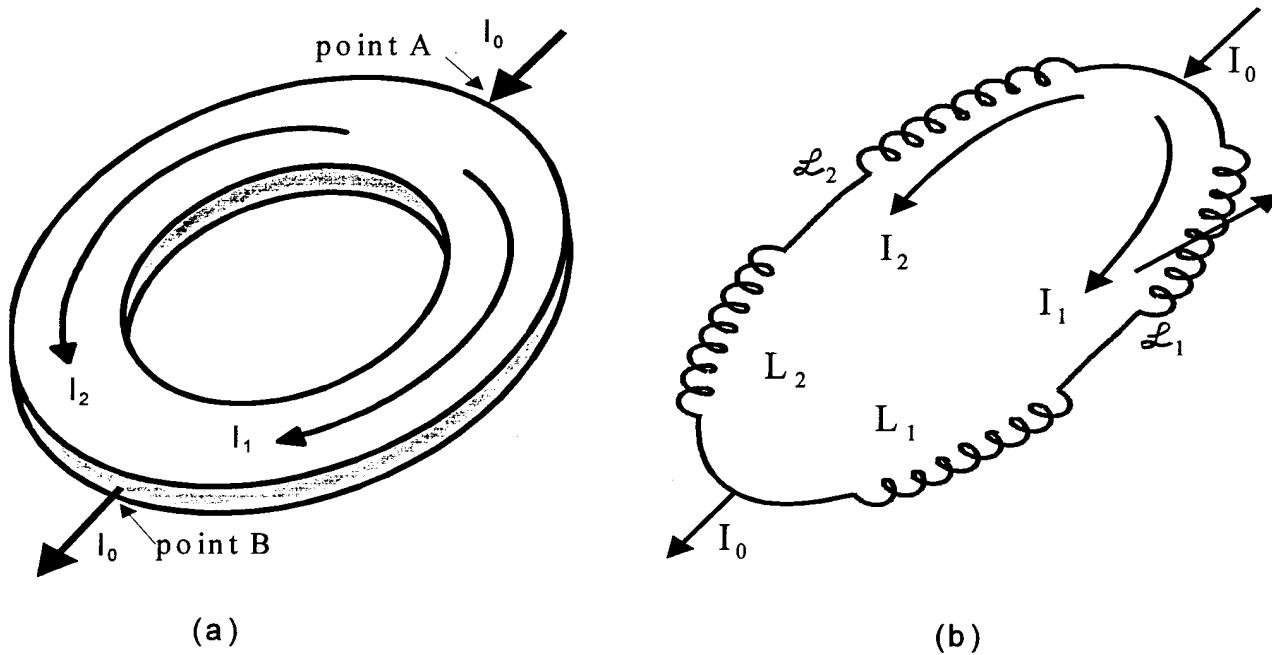


Figure 2.1. A superconducting loop (a), thinner than the London penetration depth, is subjected to a bias current I_0 injected at point "A" and removed at point "B". The bias current I_0 is divided into currents I_1 and I_2 flowing in branches 1 and 2, respectively. The QSKIP's equivalent circuit (b) contains the magnetic ($L_1 = L_{11} - L_{12}$, $L_2 = L_{22} - L_{12}$) and kinetic ($\mathcal{L}_1, \mathcal{L}_2$) inductance terms for branches 1 and 2, respectively. The self and mutual magnetic inductances are, respectively, represented by (L_{11} , L_{22}) and ($L_{12} = L_{21}$). \mathcal{L}_1 is represented as a variable inductor to indicate changes caused by photoabsorption in branch 1.

The current division in the QSKIP is calculated from the minimum of the superconductor's energy functional, the Hamiltonian. The condensate's Hamiltonian is expressed in terms of the

QSKIP operating currents, I_1 and I_2 , and the Cooper pair density $\rho_{CP}(X)$ is estimated to be constants ρ_{CP1} and ρ_{CP2} in branches 1 and 2, respectively. After incorporating the vector potential $A(X)$ into the Hamiltonian, we calculate from the energy extrema the QSKIP's equilibrium (or static nonequilibrium) operating conditions that are characterized by currents I_1 and I_2 . Photoabsorption of a constant photon flux in only one branch reduces the number of Cooper pairs in that branch resulting in a new static nonequilibrium state. With each new level of photoillumination, the QSKIP's current division changes in response to the new static nonequilibrium conditions. The QSKIP's performance, expressed in terms of the Noise Equivalent Power¹⁵ (NEP), is calculated by combining expressions for the QSKIP's photoresponse and noise.

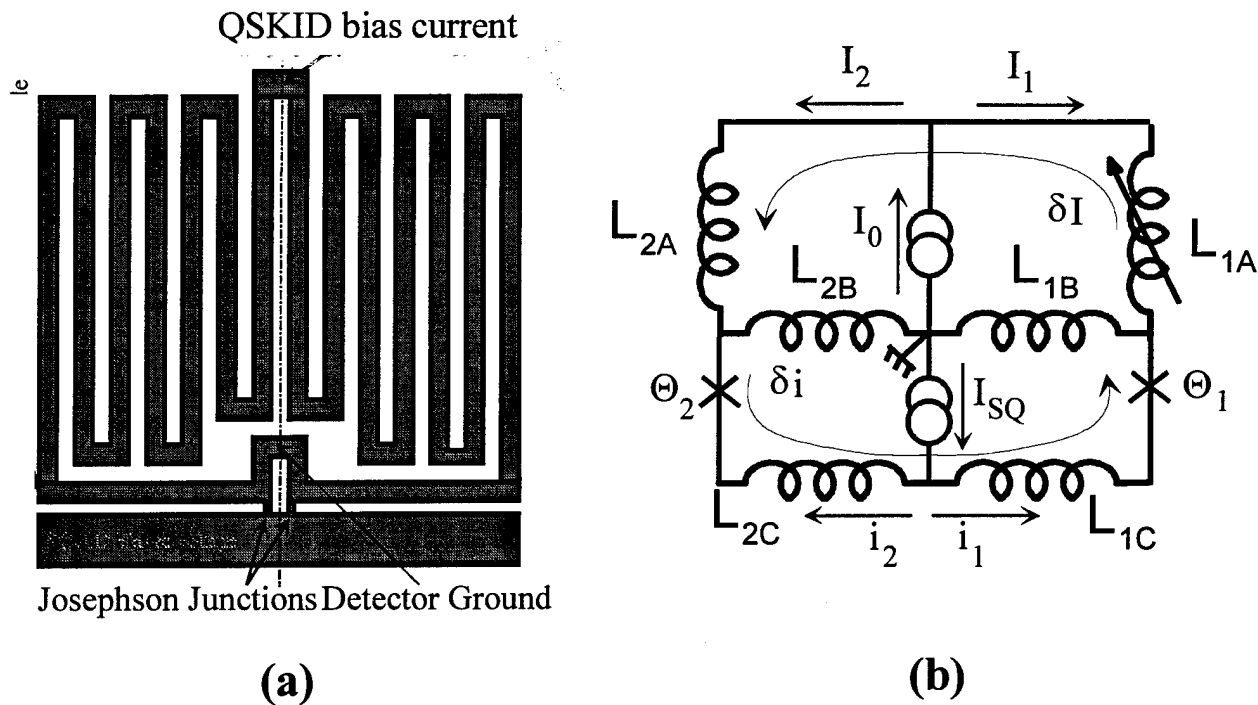


Figure 2.2. The YBCO QSKIP¹³ (a) is shaped into a serpentine pattern to increase its kinetic inductance and improve isolation against quasiparticle diffusion between the two branches. The readout SQUID is directly coupled to the QSKIP at the bottom. The photon flux only illuminates the right half of the QSKIP. The equivalent circuit (b) for the symmetrical QSKIP and readout SQUID represents the kinetic and magnetic inductances for branches 1 and 2. The QSKIP is biased with a dc current I_0 and the SQUID is biased with a dc current i_{SQ} .

2.2.1 THE QSKIP ENERGY MINIMUM

The QSKIP ring, illustrated in Fig. 2.1, receives a dc bias current I_0 , at point A, and divides it into currents I_1 and I_2 , in branches one and two, respectively, and I_0 exits at point B. The total energy of the condensate E_{QSKIP} is computed by integrating the energy of each pair over the pair density $\rho_{\text{CP}}(X)$ and the QSKIP volume $2V$. The value of currents I_1 and I_2 satisfy the energy extrema of the superconductor's Hamiltonian \mathcal{H} operating on the condensate, represented by a wave function Ψ . The Hamiltonian written in terms of canonical momentum¹⁶ (the squared term in Eq. 1) and the Cooper pairs interacting potential (last term) is:

$$\mathcal{H} = \frac{1}{2m_{\text{CP}}} [\mathbf{p}(X) + q_{\text{CP}} \mathbf{A}(X)]^2 + q_{\text{CP}} \Phi(X) + q_{\text{CP}} V_{\text{CP}}(X) \quad (1)$$

Where $\mathbf{p}(X) = m_{\text{CP}} \mathbf{v}$ is the kinetic momentum, $\mathbf{A}(X)$ is the vector potential, $V_{\text{CP}}(X)$ is the attractive potential for a Cooper pair at X , $\Phi(X)$ is the electrostatic potential energy, q_{CP} is the electric charge for a pair and m_{CP} is the mass of a pair. We simplify equation 1 by making use of the Coulomb¹⁷ gauge $\nabla \cdot \mathbf{A}(X) = 0$, and the so called London gauge¹⁸ $\Lambda \mathbf{J}(X) = -\mathbf{A}(X)$, where $\Lambda = m_{\text{CP}} / [\rho_{\text{CP}}(X) q_{\text{CP}}^2]$ and $\mathbf{J}(X)$ is the current in the superconductor.

The Hamiltonian in Eq. 1 is simplified to a form similar to the BCS Hamiltonian¹⁹ i.e.,

$$\mathcal{H} = \frac{1}{2m_{\text{CP}}} [\mathbf{p}(X)]^2 + \frac{1}{2\rho_{\text{CP}}(X)} \mathbf{A}(X) \cdot \mathbf{J}(X) + q_{\text{CP}} \Phi(X) + q_{\text{CP}} V_{\text{CP}}(X) \quad (2)$$

We have used the expression $\mathbf{J}(X) = q_{\text{CP}} \rho_{\text{CP}}(X) \mathbf{p}(X) / m_{\text{CP}}$ to simplify equation 1 and obtain an expression for the Hamiltonian with two terms in addition to the BCS terms: the second term accounts for the energy present in a flowing superconducting current, while the last term with $\Phi(X)$

was eliminated by BCS¹⁹ by solving the problem relative to the Fermi Energy, E_F . Unlike the first two terms, the last two terms in Eq. 2 are not a function of currents I_1 or I_2 and they will drop out when the energy minimum of the QSKIP is calculated relative to I_1 and I_2 . We include them for generality.

The QSKIP energy E_{QSKIP} is obtained by integrating \mathcal{H} over the Cooper pair density $\rho_{\text{CP}}(X)=\Psi^*\Psi$ where this density spans the domain of the Hermitian operator \mathcal{H} . Incorporating $\rho_{\text{CP}}(X)=\Psi^*\Psi$ and substituting $\mathbf{J}(X)=q_{\text{CP}}\rho_{\text{CP}}(X)\mathbf{p}(X)/m_{\text{CP}}$, into the Hamiltonian given by Eq. 2, the expression for the QSKIP energy E_{QSKIP} becomes:

$$E_{\text{QSKIP}} = \int_{2V} \Psi^* \mathcal{H} \Psi d^3x = \frac{1}{2} \int_{2V} \Lambda \mathbf{J}(X) \cdot \mathbf{J}(X) d^3x + \frac{1}{2} \int_{2V} \mathbf{A}(X) \cdot \mathbf{J}(X) d^3x + \int_{2V} \rho_{\text{CP}}(X) [\Phi(X) + V_{\text{CP}}(X)] d^3x \quad (3)$$

The QSKIP energy E_{QSKIP} in Equation 3 has three terms: (1) the first term represents the condensate's kinetic energy, (2) the second term represents the energy stored in the field²⁰ produced by a flowing supercurrent, and (3) the third term represents the potential energy terms.

Since the E_{QSKIP} energy minimum is calculated in terms of currents I_1 and I_2 [or the corresponding current densities $\mathbf{J}_1(X)$ and $\mathbf{J}_2(X)$] we need to express Equation 3 in terms of these. This is facilitated by doing the volume integration over branches 1 and 2. The first and last terms in Equation 3 will each yield an additional term while the middle term will yield three additional terms. The vector potential term expressed in terms of volume integral over branches 1 and 2 is:

$$\mathbf{A}(X) = \left(\frac{\mu_0}{4\pi} \right) \int_{V_1} \frac{\mathbf{J}_1(Y)}{|\mathbf{X} - \mathbf{Y}|} d^3y + \left(\frac{\mu_0}{4\pi} \right) \int_{V_2} \frac{\mathbf{J}_2(Y)}{|\mathbf{X} - \mathbf{Y}|} d^3y \quad (4)$$

Incorporating these substitutions into Eq. 3, we obtain an equation for the QSKIP energy in terms of I_1 and I_2 and the kinetic \mathcal{L}_i and magnetic L_{ij} inductance, where the subscripts “i” and “j” refer to branches one or two, i.e.,

$$E_{\text{QSKIP}} = \frac{1}{2} \mathcal{L}_1 I_1^2 + \frac{1}{2} \mathcal{L}_2 I_2^2 + \frac{1}{2} L_{11} I_1^2 + \frac{1}{2} L_{22} I_2^2 + L_{12} I_1 I_2 + \int_{2V} \rho_{\text{CP}}(X) [\Phi(X) + V_{\text{CP}}(X)] d^3x \quad (5)$$

Where $\mathcal{L}_1 = (m_{\text{CP}}/q_{\text{CP}}^2)(l_1/(S_1\rho_{\text{CP1}}))$ [$\mathcal{L}_2 = (m_{\text{CP}}/q_{\text{CP}}^2)(l_2/(S_2\rho_{\text{CP2}}))$] is the kinetic inductance of branch number one (two) with a Cooper pair density ρ_{CP1} [ρ_{CP2}], a cross sectional area S_1 (S_2) and a length l_1 (l_2). The inductance of branch one (two) is labeled by L_{11} (L_{22}) and the mutual inductance between the branches is labeled as $L_{12} = L_{21}$, by symmetry.

The minimum of E_{QSKIP} is calculated by taking the differential of equation 5 with respect to I_1 and I_2 to yield,

$$\frac{\partial E_{\text{QSKIP}}}{\partial I_i} = [\mathcal{L}_1 + L_1] I_1 - [\mathcal{L}_2 + L_2] I_2 = 0 \quad (6)$$

We make use of the fact that the currents flowing in the QSKIP branches divide $I_0 = I_1 + I_2$ hence $\partial/\partial I_1 = (\partial I_2/\partial I_1)(1/\partial I_2) = -\partial/\partial I_2$ and the magnetic inductance terms are combined into effective inductance terms: $L_1 = L_{11} - L_{12}$ and $L_2 = L_{22} - L_{12}$. It should be noted that for a symmetrical QSKIP $L_{11} = L_{22}$ and $L_{21} = L_{12}$. Equation 6 holds for any arbitrary value of Cooper pair density occurring for each level of constant photodepairing.

2.2.2 QSKIP PHOTORESPONSE

In this section we calculate the QSKIP photocurrent from the constraints governing the photodetectors operation (given by Equation 6). The photocurrent I_S is calculated first in terms of the change in kinetic inductance $\Delta\mathcal{L}_1$ (section 2.2.2.1). Next, using the modified Rothwarf-Taylor Equations, we calculate the change of $\Delta\mathcal{L}_1$ in terms of changes in the quasiparticle density ΔN_Q produced by photoabsorption (section 2.2.2.2). Finally, we relate the change in $\Delta\mathcal{L}_1$ to the quasiparticle effective lifetime described in section 2.2.2.3.

2.2.2.1 Photocurrent Calculations

The photoresponse signal, $I_S = I_1 - I_2$, is produced as the division of I_0 changes from $I_1 = I_2$ to $I_1 \neq I_2$ as one of the QSKIP branches is exposed to a constant level of illumination, and the currents change to satisfy the required *minimum energy* conditions. Without loss of generality, and for the sake of simplicity, we assume a totally symmetric QSKIP geometry, where, under no illumination and under thermal equilibrium, the Cooper pair density $\rho_{CP}(X)$ is the same in branches 1 and 2 producing a symmetric current division i.e. $I_1 = I_2 = I_0/2$. Hence, the thermal equilibrium signal current I_S^0 , and the associated magnetic flux Φ_B^0 inside the ring are zero. Photoabsorption in branch number 1 only breaks the QSKIP's symmetry in $\rho_{CP}(X)$ and produces a photosignal $I_S = I_1 - I_2$ and a corresponding net magnetic flux Φ_B inside the QSKIP's ring, where $\Phi_B = I_S(L_1 + L_2)$. Read-out of the photoinduced signal current I_S (for directly coupled) or Φ_B (for magnetically coupled) is by a SQUID.

The signal current I_S is produced by kinetic inductance changes $\Delta\mathcal{L}_1$ caused by photoabsorption, in branch 1 only, of N_Φ photons with an average value of N_Φ^0 . The signal current consists of a circulating current I_S , causing a corresponding magnetic flux Φ_B . The signal

photocurrent I_s directly depends on $\Delta \mathcal{L}_1$ and is computed by taking the differential of Eq. 6 to obtain:

$$I_s = \frac{\partial I_1}{\partial \mathcal{L}_1} \Delta \mathcal{L}_1 = \frac{-I_1}{[\mathcal{L}_1 + L_1 + \mathcal{L}_2 + L_2]} \Delta \mathcal{L}_1 \quad (7)$$

Equation 7 is valid under static nonequilibrium conditions and when the quasiparticle density N_Q is much less than $\rho_{CP}(X)$. Using partial derivatives, the change in the kinetic inductance $\Delta \mathcal{L}_1$ is expressed as:

$$\Delta \mathcal{L}_1 = \frac{\partial \mathcal{L}_1}{\partial \rho_{CP}(X)} \frac{\partial \rho_{CP}(X)}{\partial N_Q} \Delta N_Q \quad (8)$$

Explicit expressions for the partial derivative factors in Eq. 8 are obtained using Eq. 6, the definition of \mathcal{L}_1 (given below Eq. 5), and the fact that each Cooper pair forms two quasiparticles ($\partial \rho_{CP}(X)/\partial N_Q = -1/2$). To complete the calculation for I_s , an explicit expression for ΔN_Q is needed that represents the photoinduced increase in the quasiparticle population in branch 1.

The total static nonequilibrium quasiparticle density N_Q is expressed as a sum of the thermal equilibrium quasiparticle density N_Q^{EQ} and the photoinduced increase in the quasiparticle density, $N_Q = \Delta N_Q + N_Q^{EQ}$. The thermal equilibrium quasiparticle density in each branch, based on a BCS superconductor at $T < 0.5 T_C$, is given by:²¹

$$N_Q^{EQ} = 2N(0) \sqrt{\frac{\pi}{2} \Delta(T) k_B T} \exp\left(-\frac{\Delta(T)}{k_B T}\right) \quad (9)$$

where $N(0)$ is the density of states in volume and energy at the Fermi surface, k_B is Boltzmann's constant, T is the operating temperature in degrees Kelvin, and $\Delta(T)$ is the temperature dependent

superconducting energy gap. An expression for the change in the quasiparticle density ΔN_Q from the thermal equilibrium value N_Q^{EQ} is obtained with a *modified* form of the Rothwarf-Taylor²² equations.

2.2.2.2 Photoinduced Quasiparticle Population

The Rothwarf-Taylor equations, 10 and 11, describe a superconductor in nonequilibrium in terms of: the quasiparticle density, N_Q , the pair breaking (PB) phonon density, N_Ω , and the absorbed photon flux density,²³ N_Φ , as:

$$\frac{dN_Q}{dt} = 2m_1\eta N_\Phi + \frac{2N_\Omega}{\tau_B} - RN_Q^2 \quad (10)$$

$$\frac{dN_\Omega}{dt} = \frac{RN_Q^2}{2} - \frac{N_\Omega}{\tau_B} - \left[\frac{1}{\tau_{ES}} + \frac{1}{\tau_{AH}} \right] [N_\Omega - N_\Omega^{EQ}] + 2m_2\eta N_\Phi, \quad (11)$$

where $R=1/[\tau_R^{EQ} N_Q^{EQ}]$, $1/\tau_R^{EQ}$ is the thermal equilibrium quasiparticle recombination rate, $1/\tau_B$ is the quasiparticle generation rate by PB phonons (since only PB phonons have sufficient energy $2\Delta(T)$ to break Cooper pairs). The phonon depletion occurs by: (1) PB phonon escape into the substrate with rate $1/\tau_{ES}$, or (2) anharmonic rate decay of PB phonons into multiple phonons (each with energy less than $2\Delta(T)$) with rate $1/\tau_{AH}$.

We have incorporated into the Rothwarf-Taylor equation the effects of photoabsorption of a photon density N_Φ , acting with an internal quantum efficiency η . Specifically, each photoabsorbed photon, with energy $h\nu$, is thermalized by electron-electron and electron-phonon interactions. Quasiparticles directly photogenerated by electron-electron interactions^{24,25} are represented by the term $2m_1\eta N_\Phi$, in Eq. 10. Quasiparticles generated by electron-phonon interactions²⁶ are represented

by $m_2\eta N_\Phi$, in Eq. 11. The constants m_1 and m_2 represent, respectively, the number of quasiparticles and PB phonons produced by photoabsorbed photon^{27,28}. In these calculations we assume photons with energy ($h\nu$) much larger than 2Δ and the PB phonons with energies ($h\Omega \geq 2\Delta$) which are related by an approximation $h\nu \approx m_1(2\Delta) + m_2(h\Omega)$. Here the Fano²⁹ factor has been neglected. Also for YBCO $\tau_{ES} \gg \tau_{AH}$. These equations are simplified into *linear* equations by invoking static nonequilibrium operating condition detailed below.

First, since the QSKIP is operating in static nonequilibrium conditions on average $dN_Q/dt = dN_\Omega/dt = dN_\Phi/dt = 0$. There are time fluctuations in the densities of N_Φ , N_Q , and N_Ω and they manifest themselves as noise in the QSKIP, and these are considered in Section 2.2.3. Here, we are only interested in the *average* values of N_Φ , N_Q , and N_Ω , and this simplifies Equations 10 and 11 into two nonlinear equations.

Second, the nonlinearity in the Rothwarf-Taylor equations is also removed by incorporating the static nonequilibrium conditions into the term R in equations 10 and 11. The nonlinear term represents the quasiparticle recombination rate and is expressed as a product of N_Q^2 and R . The N_Q^2 term represents the number of ways a pair can be formed from N_Q quasiparticles. Specifically, for N_Q quasiparticles there are $N_Q(N_Q-1)/2$ ways of pairing and since each pairing removes two quasiparticles we obtain the N_Q^2 factor, for $N_Q \gg 1$. The term R represents the recombination rate for two particular quasiparticles. The term R is not equal to the reciprocal of the quasiparticle lifetime $1/\tau_R^{EQ}$, calculated by Kaplan et al.³⁰ Kaplan calculated the recombination rate, at thermal equilibrium, of a particular quasiparticle with any one of the N_Q^{EQ} available quasiparticles. Thus at thermal equilibrium, the factor $R = 1/[\tau_R^{EQ} N_Q^{EQ}]$ and N_Q^{EQ} is included in the denominator to preclude double counting. Rothwarf and Taylor²² expressed R in terms of the thermal equilibrium values

τ_R^{EQ} and N_Q^{EQ} , where τ_R^{EQ} can be taken from Kaplan.³⁰ Since the QSKIP operates under static nonequilibrium conditions, it is appropriate to express R in terms of the corresponding static nonequilibrium values, specifically $R=1/[\tau_R N_Q]$. This representation for R has the benefit of *linearizing* the Rothwarf-Taylor equations.

The solution for ΔN_Q is obtained by incorporating the above conditions into equations 10 and 11 and solving for N_Q to obtain:

$$N_Q = N_Q^{EQ} + \left(m_1 + m_2 \right) \frac{\tau_{AH} \tau_{ES}}{\tau_{AH} + \tau_{ES}} \eta N_\phi \quad (12)$$

This indicates that photoabsorption increases the PB phonon population beyond the thermal equilibrium number N_Q^{EQ} and the increase is directly proportional to: the effective internal quantum efficiency $(m_1+m_2)\eta$, the PB removal lifetime $(\tau_{ES} \tau_{AH})/(\tau_{ES}+\tau_{AH})$, and the photon density N_ϕ . Substituting Eq. 12 into Eq. 10 and simplifying by recognizing that $\tau_B \ll (\tau_{ES} \tau_{AH})/(\tau_{ES}+\tau_{AH})$, we obtain

$$N_Q^{EQ} + \Delta N_Q = 2 \eta \left(m_1 + m_2 \right) \left(\frac{\tau_{AH} \tau_{ES}}{\tau_{AH} + \tau_{ES}} \right) \frac{\tau_R}{\tau_B} N_\phi + 2 \frac{\tau_R}{\tau_B} N_Q^{EQ} \quad (13)$$

In Eq. 13, N_Q is replaced by $N_Q^{EQ} + \Delta N_Q$ to provide an expression for the change in quasiparticles' density in terms of N_ϕ and N_Q^{EQ} . Equation 13 is valid only for nonequilibrium conditions where $N_Q > N_Q^{EQ}$ or $\Delta N_Q > 0$. This requirement is satisfied by replacing (in Eq. 13) $2(\tau_R/\tau_B)N_Q^{EQ}$ by N_Q^{EQ} , since under thermal equilibrium conditions, when $N_\phi=0$, the nonequilibrium excess quasiparticle density $\Delta N_Q=0$. Solving Eq. 13 for ΔN_Q and substituting this into Eq. 8 and combining with Eq. 7, the explicit expression for I_s becomes

$$I_s = \frac{I_0}{4\rho_{CP}(X)} \frac{\mathcal{L}_1}{(L_1 + \mathcal{L}_1)} \left[\eta (m_1 + m_2) \left(\frac{\tau_{AH} \tau_{ES}}{\tau_{AH} + \tau_{ES}} \right) \frac{\tau_R}{\tau_B} N_\phi \right] \quad (14)$$

The expression in the square brackets in Eq. 14 is for ΔN_Q . The photocurrent I_s depends on the effective quantum efficiency $[(m_1 + m_2)\eta]$, the effective quasiparticle lifetime $\tau_R \tau_{AH} \tau_{ES} / [(\tau_{AH} + \tau_{ES})\tau_B]$, and N_ϕ . The effective internal quantum efficiency term is made up of: (1) the internal photon absorption efficiency η within the superconductor, (2) the number of quasiparticles generated by electron-electron interaction (m_1), and (3) the number of quasiparticles generated by electron-phonon interactions (m_2). Thus each absorbed photon, with energy several times larger than 2Δ generates up to $h\nu/\Delta$ quasiparticles. As expected, the effective quasiparticle lifetime has a direct influence on determining the signal I_s and it is considered next.

2.2.2.3 Effective Quasiparticle Lifetime

We estimate the quasiparticle lifetime assuming a BCS type superconductor, based on “s” wave pairing. This is appropriate for low temperature materials but is presently unresolved for high temperature materials, where the nature of the superconducting gap is still in question. It should be noted that calculations taking account of “d” and “s” wave pairing have been made by Sergeev and Reizer³¹ with results similar to our calculations. With this caveat, we proceed to estimate the quasiparticle lifetime using a BCS model.

The intrinsic quasiparticle lifetime at or near thermal equilibrium is very sensitive to temperature and for a BCS superconductor at $T < 0.5T_C$ the quasiparticle lifetime is given by Kaplan as³⁰:

$$\tau_R(T) = \frac{\tau_0}{\sqrt{\pi}} \left[\frac{k_B T_C}{2\Delta_0} \right]^{5/2} \left[\frac{T_C}{T} \right]^{1/2} \exp \left[\frac{\Delta_0}{k_B T} \right] \quad (15)$$

$$\approx 0.1 \tau_0 \exp \left[\frac{\Delta_0}{k_B T} \right] ,$$

where, for low temperature superconductors, a representative values for τ_0 calculated by Kaplan³⁰ et. al is approximately 10^{-11} seconds. At small reduced temperatures ($T \leq 0.1 T_C$) and for a BCS superconductor ($\Delta_0 \approx 1.72 k_B T_C$), the intrinsic recombination lifetime (computed with Eq. 15) becomes very large ($\tau_R \approx 30 \mu\text{sec}$) and is much larger than τ_0 . Since high temperature superconductors are projected to have an even larger energy gap, even longer quasiparticle lifetimes are expected. For example, in YBCO the energy gap, obtained from specific heat measurements³² ($\Delta_0 \approx 2.5 k_B T_C$), is larger than the BCS gap leading to a very long projected intrinsic quasiparticle lifetime, $\tau_R \approx 70 \text{msec}$.

The effective quasiparticle lifetime depends on several components: the intrinsic quasiparticle lifetime, τ_R ; the phonon escape lifetime into the substrate, τ_{ES} ; the anharmonic phonon decay lifetime, τ_{AH} ; and the pair breaking lifetime, τ_B . The increase in the effective quasiparticle lifetime is evident from the solution to the Rothwarf-Taylor equations 12 and 13 where the combination of lifetimes τ_R , τ_B , τ_{ES} , and τ_{AH} results in an effective quasiparticle lifetime τ_{EFF} given by:

$$\frac{1}{\tau_{EFF}} = \frac{1}{\frac{\tau_R}{\tau_B} \tau_{ES}} + \frac{1}{\frac{\tau_R}{\tau_B} \tau_{AH}} \quad (16)$$

The effective quasiparticle lifetime is limited by the depletion rate of nonequilibrium PB phonons through: (1) escape into the substrate with effective rate $[(\tau_R/\tau_B)\tau_{ES}]^{-1}$ and (2) anharmonic phonon decay with effective rate $[(\tau_R/\tau_B)\tau_{AH}]^{-1}$. At lower temperatures and near thermal equilibrium, these rates are much slower because $(\tau_R/\tau_B) \gg 1$.

The ratio of τ_R/τ_B is estimated in terms of the quasiparticle density N_Q and the total Cooper pair density. Using the golden rule for time dependent perturbation theory,³³ the quasiparticle recombination rate is given as $1/\tau_R = 2\pi/\hbar |\langle f | \mathcal{H}_{IN} | i \rangle|^2 \Gamma N_Q$, where \mathcal{H}_{IN} is the interaction Hamiltonian, Γ contains coherence and occupation factors,¹⁹ N_Q is the density of available recombination sites for going from the initial state $|i\rangle$ to the final state $|f\rangle$. For recombination conditions where $\rho_{CP}(X) \gg N_Q$. Similarly, using the golden rule, the pair breaking rate $1/\tau_B = 2\pi/\hbar |\langle f | \mathcal{H}_{IN} | i \rangle|^2 \Gamma \rho_{CP}(E_f)$ where the value of $|\langle f | \mathcal{H}_{IN} | i \rangle|^2$ is the same squared matrix element used for calculating $1/\tau_R$. Quasiparticle generation rate, under conditions where $\rho_{CP}(X) \gg N_Q$, is proportional to $\rho_{CP}(X)$, since this is approximately equal to the number of unoccupied quasiparticle states. From these expressions, we estimate for the ratio of the quasiparticle generation to the quasiparticle recombination lifetime as $\tau_R/\tau_B \approx \rho_{CP}(X)/N_Q$.

The effective anharmonic decay and phonon escape lifetimes are greater than the intrinsic lifetime values, τ_{AH} and τ_{ES} ,^{34,35,36} because, at low temperatures, the nonequilibrium photodeposited energy resides most of the time in the form of excited quasiparticles (since $\tau_R/\tau_B \approx \rho_{CP}(X)/N_Q \gg 1$), and the photodeposited energy can only escape when it exists in the form of nonequilibrium phonons and not quasiparticles. Since the photodeposited energy exists for the largest fraction of time, $\tau_R/(\tau_R + \tau_B)$, in the form of excited quasiparticles, there is proportionally very little time during which the nonequilibrium PB phonons can escape into the substrate or undergo anharmonic decay.

Therefore at low temperatures, the effective lifetimes τ_{AH} and τ_{ES} become very large. With a longer τ_{EFF} , the QSKIP expected performance is significantly improved and this is evident from the Noise Equivalent Power (NEP) calculations in section 2.2.5. The noise current δI is calculated next.

2.2.3 NOISE LEVEL IN QSKIP

The QSKIP's noise current δI is calculated from the Root Mean Square (RMS) fluctuations in the signal current I_S , specifically, $(\delta I)^2 = \langle I_S^2 \rangle - \langle I_S \rangle^2$ where the brackets $\langle \rangle$ represent the expected value. A superconductor operating in the current state, in principle, has two major noise sources possible : (1) fluctuations in the Cooper pair density and (2) fluxoid noise. The QSKIP is intended to operate at low temperatures and at $I_0 < 0.5 I_C$. Under these conditions, the operation of the QSKIP can be readily limited below H_{C1} thereby minimizing the effects of fluxoid noise. Accordingly we calculate the noise in the QSKIP as primarily due to fluctuations in the Cooper pair density. Expressions for the noise current δI are derived in terms of the statistical fluctuations in the density of Cooper pairs $\rho_{CP}(X)$ (or quasiparticle density N_Q) in branches 1 and 2 (see Fig. 2.1). The QSKIP noise current, δI , is expressed in terms of the quasiparticle density variances, σ_{Q1}^2 , and, σ_{Q2}^2 , in branches 1 and 2, respectively. The expression for the total noise current δI , is calculated as is the signal current I_S by using Eq. 14 and adding, in quadrature, contributions from branches 1 and 2. Making use of Eq. 7 and 8, the equation for the QSKIP's RMS noise current is:

$$\sqrt{\delta I^2} = \frac{I_0}{4\rho_{CP}(X)} \frac{\ell_1}{(\ell_1 + L_1)} \sqrt{\frac{\sigma_{Q1}^2 + \sigma_{Q2}^2}{V}} \quad (17)$$

The quasiparticle density variance, σ_{Q2}^2 , for the thermal equilibrium branch is calculated from the quasiparticle statistics. At low temperature, the quasiparticle density is much less than the

Cooper pair density ($\rho_{CP}(X) \gg N_Q$) hence the probability, P , for breaking a Cooper pair is very small and we estimate the average quasiparticle density by $P\rho_{CP}(X) \approx N_Q^{EQ}$. Under these conditions, it can be shown that the quasiparticle statistics³⁷ can be represented by a Poisson Probability Density Function (PDF). For a Poisson PDF, the variance σ_{Q2}^2 is equal to the mean quasiparticle density in branch 2, $\sigma_{Q2}^2 = (1/V)N_Q^{EQ}$. The mean quasiparticle density is given by Equation 8.

Because of photoabsorption $\sigma_{Q1}^2 > \sigma_{Q2}^2$. The quasiparticle density in branch 1, N_Q , is expressed in terms of the thermal equilibrium quasiparticle density N_Q^{EQ} and the additional density of static nonequilibrium quasiparticles, ΔN_Q , generated by the absorption of N_Φ . This corresponds to a nonequilibrium state that is *different from thermal models where the increases in the quasiparticle population are due to heating of the superconductor*. Here, the quasiparticles' nonequilibrium state is maintained by an excess static nonequilibrium of PB phonons. The total PB phonon density is made up of contributions due to thermal equilibrium PB phonons N_Ω^{EQ} , represented by Bose-Einstein statistics, and contributions due to photogenerated nonequilibrium PB phonons. The photogenerated nonequilibrium phonons span a narrow energy range because photoexcited hot quasiparticles thermalize most efficiently by the emission of energetic phonons, to which they are most strongly coupled. These energetic phonons are primarily the PB phonons that maintain the nonequilibrium quasiparticle population by virtue of the fact that they participate in the quasiparticle generation and recombination process, since they have a minimum energy of $\approx 2\Delta$. This nonequilibrium phonon representation is similar to (but not the same as) the T^* approach used by Parker.³⁸ Parker represented the phonon densities in a superconductor under static thermal nonequilibrium as a sum of: (1) thermal equilibrium phonon density represented by a thermal equilibrium temperature T_0 and (2) an excited phonon density represented by a higher thermal

equilibrium temperature $T^* > T_0$. Here, we are representing the static nonequilibrium phonon distribution as a sum of two phonon densities: (1) the N_{Ω}^{EQ} thermal equilibrium PB phonon density, and (2) a nonequilibrium phonon population $\Delta N_{\Omega} = N_{\Omega} - N_{\Omega}^{\text{EQ}}$ (see Eq. 12), which span a narrow energy range with an energy greater than 2Δ . It should be clear that this static nonequilibrium distribution of quasiparticles and PB phonons cannot be described by two thermal equilibrium distributions at different temperatures, the T^* model.

The quasiparticle variance is determined by the processes ongoing in branch 1. In static nonequilibrium, the effective quasiparticle lifetime is much larger than the intrinsic quasiparticle lifetime because of the many quasiparticle generation and recombination events occurring before the photoabsorbed energy is removed with the anharmonic decay or escape of the PB phonons. These numerous generation and recombination events (experienced by each quasiparticle, and governed by the Rothwarf-Taylor Eqs. 10 and 11) effectively decouple the quasiparticle statistics from the photogenerating photon statistics. Again given our QSKIP operating constraints, as in the case of the unilluminated branch 2, the quasiparticle density is much smaller than the Cooper pair density ($\rho_{\text{CP}}(X) \gg N_Q$). This corresponds to conditions where the probability for breaking a Cooper pair, P , is very small, thus making the average quasiparticle densities $N_Q^{\text{EQ}} + \Delta N_Q \approx P N_{\text{CP}}$. Under these conditions, the quasiparticles obey Poisson statistics and the variance σ_{Q1}^2 is equal to the mean quasiparticle density in branch 1, given by $\sigma_{Q1}^2 = (1/V)[N_Q^{\text{EQ}} + \Delta N_Q]$ (see Eq. 13). Using the explicit expression for the quasiparticle density variances, the expression for the QSKIP noise in Eq. 17 becomes:

$$\sqrt{\delta I^2} = \frac{I_0}{4\rho_{\text{CP}}(X)} \frac{\mathcal{L}_1}{(\mathcal{L}_1 + L_1)} \sqrt{\frac{2\eta(m_1 + m_2)\tau_{\text{EFF}} N_{\phi} + 2 N_Q^{\text{EQ}}}{V}} \quad (18)$$

The square root term includes the noise from the ΔN_Q additional quasiparticles photogenerated in the illuminated branch and beyond the $2N_Q^{\text{EQ}}$ thermal equilibrium density in both branches .

2.2.4 RESPONSIVITY AND NEP OF QSKIP

The QSKIP operates in the zero resistance current state and accordingly the responsivity (\mathcal{R}_I) and NEP (calculated at the end of this section) are calculated in terms of current and not voltage. The calculated responsivity is readily expressed in terms of the photoinduced magnetic flux Φ_B simply by multiplication of \mathcal{R}_I by the QSKIP total magnetic inductance L_1+L_2 . The expressions for the current responsivity \mathcal{R}_I is:

$$\mathcal{R}_I \left(\frac{\text{Amps}}{\text{Watt}} \right) = \frac{1}{h\nu} \frac{I_s}{VN_\phi^0} \quad (19)$$

The explicit expression for $\mathcal{R}_I(\text{A/Watt})$ is obtained by substituting I_s (Eq. 14) into Eq. 19 and dividing by the incident photon power, $Vh\nu N_\phi^0$, to yield:

$$\mathcal{R}_I = \frac{1}{Vh\nu} \frac{I_0}{4\rho_{\text{CP}}(X)} \frac{\ell_1}{(\ell_1 + L_1)} 2\eta(m_1 + m_2) \tau_{\text{EFF}} \quad (20)$$

The responsivity is directly proportional to the effective quasiparticle lifetime τ_{EFF} , as is expected for a photoconductive nonequilibrium quantum photodetector.³⁹ At low temperatures, the responsivity is greatly increased because the ratio $\tau_R/\tau_B \approx \rho_{\text{CP}}(X)/N_Q \gg 1$ (see section 2.2.2.3 and calculations by S. B. Kaplan³⁰ et. al) resulting in an effective quasiparticle lifetime significantly larger than the phonon trapping lifetime τ_{ES} (produced by acoustical mismatch at the film substrate interface) or the anharmonic phonon decay lifetime τ_{AH} . Thus, the maximum responsivity occurs at low temperatures.

BLIP is achieved when τ_{EFF} is sufficiently large so that the photon radiation shot noise is equal to the photodetector noise and the readout circuit noise, added in quadrature. From Equation 18, it is evident that one requirement for BLIP is that $\eta(m_1+m_2)\tau_{\text{EFF}}N_{\Phi}^0 > N_Q^{\text{EQ}}$. The NEP is generically represented by:

$$\text{NEP(Watts)} = \frac{[\delta I^2 + \delta I_{\text{SQUID}}^2]^{1/2}}{\mathfrak{R}_I} \quad (21)$$

Under BLIP conditions, the photon radiation shot noise is equal to the photodetector's internal noise. In section 2.2.4 it was shown that the photodetector's noise can be represented in terms of the quasiparticle variances σ_{Q1}^2 and σ_{Q2}^2 , that obey Poisson statistics. Hence, noise from the photogenerated quasiparticles is equal to the noise from thermal equilibrium quasiparticles when $\eta(m_1+m_2)\tau_{\text{EFF}}N_{\Phi}^0 \approx N_Q^{\text{EQ}}$, see Eq. 18. The expression for the QSKIP's BLIP NEP, obtained with Eq. 20, (and assuming negligible electronic readout noise) is

$$\text{NEP}_{\text{BLIP}} = h\nu \sqrt{\frac{VN_Q^{\text{EQ}} \Delta F}{\eta(m_1 + m_2)\tau_{\text{EFF}}}} \quad (22)$$

The QSKIP NEP varies with: VN_Q^{EQ} , the effective internal quantum efficiency $[\eta(m_1+m_2)]$, the electrical operating bandwidth of the readout circuit ΔF , and the effective quasiparticle lifetime, τ_{EFF} . The VN_Q^{EQ} term corresponds to variance of the thermal equilibrium quasiparticle population (Poisson statistics).

2.2.5 The NEP of a YBCO QSKIP

The NEP is computed for a 100 μm square by 100nm thick YBCO QSKIP. In computing the NEP, we determine the operating conditions necessary for achieving BLIP performance.

Specifically, three conditions are required and are satisfied: (1) the QSKIP is assumed to operate at sufficiently low temperatures such that the photoinduced quasiparticle density is equal to or larger than the thermal equilibrium quasiparticle density N_Q^{EQ} ; (2) the QSKIP bias current is limited to less than $0.5I_C$ to insure operation below H_{C1} , thereby circumventing noise problems associated with fluxoid generation and transport, and (3) the photon density levels N_Φ^0 are selected so that the noise associated with the QSKIP dominates over the readout noise, i.e. $\delta I > \delta I_{SQUID}$. The last condition is the most stringent and we consider it first.

To satisfy the requirement that $\delta I > \delta I_{SQUID}$ several operating conditions need to be met: (1) large τ_{EFF} , (2) I_0 sufficiently small to inhibit fluxoid noise, and (3) $\rho_{CP}(X) \gg N_Q$. Presently for YBCO, there are no universally accepted theoretical or experimental values available for τ_{EFF} and $\rho_{CP}(X)$ and we proceed to estimate these.

(1) Estimating τ_{EFF} in a YBCO QSKIP requires knowledge of τ_R/τ_B , τ_{ES} , τ_{AH} , and $2\Delta(0)$. The value of $2\Delta(0)$ is needed to determine the PB phonon's frequency for estimating τ_{ES} , and τ_{AH} , since an estimate already exists for $\tau_R/\tau_B \approx \rho_{CP}(X)/N_Q$ (see section 2.2.2.3). From specific heat measurements³² in YBCO, the measured pair binding energy $2\Delta(0)$ is about $32\text{meV} \approx 5k_B T_C$. This energy gap value is consistent with the Raman measurements which from line broadening identified the B_{1g} (out-of-phase oxygen plane vibration) at 340cm^{-1} as being particularly strongly coupled with the electrons^{40,41} and this is inferred as being related to superconductivity. This strongly suggests that the PB phonons are energetic B_{1g} optical phonons whose energies are approximately equal to the YBCO Debye energy⁴² phonons, which corresponds to the value of the energy gap, $2\Delta(0) \approx 32\text{meV}$.

The estimate for the phonon escape lifetime τ_{ES} is based on several experimental results. Experimental measurements with acoustic phonons indicate a temperature independent 99% scattering probability at the YBCO/substrate boundary ($\tau_{ES} \approx 10^{-8}$ sec for 100nm YBCO film)⁴³. For PB phonons there are no similar measurements, however, the YBCO phonon dispersion curves in the "c" direction⁴⁴ indicate that *there are no phonon propagating modes with sufficient energy to break Cooper pairs*. Thus from a c-axis oriented HTS film, PB phonons will not be depleted by escaping into the substrate because of the relatively poor coupling between the supercurrent carrying CuO planes. Thus, we expect that the depletion of PB phonons is primarily by anharmonic phonon decay, i.e. $\tau_{AH} \ll \tau_{ES}$.

Experimental values for τ_{AH} are not available for PB phonons. The value of τ_{AH} is estimated from measurements on YBCO subjected to large deviations from thermal equilibrium, and induced by excitations with energetic laser pulses²⁷. At large deviations from thermal equilibrium, $\rho_{CP}(X) \approx N_Q$ resulting in $\tau_R/\tau_B \approx 1$ (see section 2.2.2.3), and the measured effective relaxation lifetimes should correspond to $\tau_{AH} \approx 10$ -100psec. At low temperatures and near thermal equilibrium thermal $\tau_R/\tau_B \approx \rho_{CP}(X)/N_Q \gg 10^6$, leading to an estimate for $\tau_{EFF} \approx 1$ msec.

(2) The value of $I_0 < 0.5I_C$ is chosen to facilitate operation of the QSKIP below H_{C1} and outside the fluxoid formation regime and associated noise effects. A reasonable value for the critical current density in YBCO at low temperatures is $\approx 2 \times 10^7$ A/cm². For a 100nm thick YBCO film, 7 μ m wide, $I_C \approx 0.14$ A and an operating current $I_0 \leq 0.1$ Amp is less than I_C . The self induced magnetic field produced by I_0 is less than 90 Gauss, which is below the value of H_{C1} in YBCO,^{45,46,47} thereby facilitating the maintenance of the QSKIP in the Meissner state, and eliminating flux flow noise.

(3) The Cooper pair density for YBCO, $\rho_{CP}(X)$, is estimated from specific heat measurement that identify the contribution of the electronic component, γ_p . The density of states at the Fermi surface⁴⁸ $N(0) \approx 3\gamma_p/(\pi^2 k_B^2)$ is estimated from measured values⁴⁹ of γ_p [between 1.4-2.9 mJ/(g-atom-K²)] to be about $2.8-5.8 \times 10^{27}$ states/(eV-m³). Furthermore, the specific heat jump⁴⁹ at T_C [$\Delta C/\gamma_p T_C$] varies between 0.4-1.11 instead of the BCS value of 1.43. Loram et. al³² measured γ_p at 10K in YBCO and showed it vanishes, hence the reduced jump in the specific heat at T_C is not attributed to multiphase YBCO sample, with normal regions, but it is simply an indication of a smaller fraction (10%-30%) of k-space pairing than in a BCS superconductor. Accordingly, our estimate of $\rho_{CP}(X)$ is 10%-30% of $\Delta(0)N(0)/2 \approx 0.2-1.4 \times 10^{25}$ pairs/m³. For a serpentine QSKIP structure with 7 μ m wide lines formed in a 0.1 μ m thick YBCO film and within a 50x100 μ m area, the calculated value for $V \approx 5 \times 10^{-16}$ m³, which corresponds to a kinetic inductance of about $L_1 \approx 1.4-8$ nH.

We can now proceed to calculate the value of N_Φ^0 needed to ensure that the SQUID read out noise is less than the QSKIP noise, $\delta I_{SQUID} < \delta I$. Good modulation of the readout SQUID output voltage with magnetic flux requires $L_{SQ} I_{SQ} < \Phi_0$, where I_{SQ} and L_{SQ} are the SQUID critical current and loop inductance, respectively. Designing a SQUID with $I_{SQ} \approx 100 \mu$ A, is reasonable given a loop inductance $L_{SQ} \approx 20$ pH. These SQUID operating conditions yield a $\gamma = \hbar I_{SQ} / e k_B T \approx 600$ and this is consistent with operation that prevents significant noise rounding in the I-V curves⁵⁰. For a directly coupled SQUID readout circuit,¹³ and under BLIP conditions, we require that $\delta I_{SQUID} < \delta I$. An achievable SQUID flux noise level^{51,52} is $\approx 3 \times 10^{-7} \Phi_0 / \text{Hz}^{1/2} \approx 6 \times 10^{-22}$ Webers/ $\sqrt{\text{Hz}}$, and for $L_{SQ} \approx 20$ pH, we compute $\delta I_{SQUID} \approx 3 \times 10^{-11}$ Amps/ $\sqrt{\text{Hz}}$. To satisfy the condition $\delta I_{SQUID} < \delta I$, we need to select a sufficiently large N_Φ^0 (see Eq. 18) to satisfy the following expression:

$$\frac{I_0}{4\rho_{CP}(X)} \frac{\ell_1}{(L_1 + \ell_1)} \sqrt{\frac{2\eta(m_1 + m_2)\tau_{EFF} N_\phi^0}{V}} > 3 \times 10^{-11} \sqrt{\Delta F} \quad (23)$$

Evaluating Eq. 23 by substituting average values for: $\ell_1 \approx 4.7\text{nH}$, $\ell_1/(L_1 + \ell_1) \approx 1$, $I_0 \approx 0.1$ Amps, $\rho_{CP}(X) \approx 0.8 \times 10^{25}$ pairs/m³, $\eta(m_1 + m_2) \approx 1$, and 30Hz for ΔF , we obtain $\tau_{EFF} N_\phi^0 > 1.4 \times 10^{18}$ photons/m³. For a projected $\tau_{EFF} \approx 1\text{msec}$, we determine that $N_\phi^0 > 1.4 \times 10^{21}$ photons/m³-sec (corresponding to more than 1.4×10^{10} photons/sec-cm²) is required for photon noise to dominate over the readout noise, i.e., $\delta I > \delta I_{SQUID}$.

For BLIP performance, in addition to the requirement that $\delta I > \delta I_{SQUID}$, N_ϕ^0 needs to be sufficiently large so that the photodetector is dominated by the photoinduced quasiparticle noise, that is, $\eta(m_1 + m_2)\tau_{EFF} N_\phi^0 > N_Q^{EQ}$ (see Eq. 18). Below 9K, the value of N_Q^{EQ} is readily calculated with Eq. 9, where the product of all the preexponential factors is approximately equal to about 3.8×10^{25} quasiparticles/m³. Evaluating Eq. 9 at 9K, with $\Delta(0) \approx 16\text{meV}$, we obtain $N_Q^{EQ} \approx 1.6 \times 10^{16}$ quasiparticles/m³ and this leads to the requirement that $\tau_{EFF} N_\phi^0 > 4 \times 10^{16}$ quasiparticles/m³ [assuming as before that $\eta(m_1 + m_2) \approx 1$]. This is a less strict requirement than $\delta I > \delta I_{SQUID}$ which requires that $\tau_{EFF} N_\phi^0 > 1.4 \times 10^{18}$ photons/m³ (see bottom of previous paragraph).

For $\delta I > \delta I_{SQUID}$, we calculate the NEP at BLIP. At 9K, for $\tau_{EFF} \approx 1\text{msec}$, $N_\phi^0 > 1.4 \times 10^{21}$ photons/m³-sec (corresponding to 1.4×10^{10} photons/sec-cm²). For 0.1eV photons, the equivalent NEP in a 30 Hz bandwidth is about 7×10^{-17} Watts. The NEP is limited by the readout circuit noise. Better NEP might be possible with smaller operating bandwidth, or larger values of τ_{EFF} or $\Delta(T)$, which are potentially possible with HTS material with a higher T_C . The QSKIP performance is currently being experimentally investigated.

2.2.6 CONCLUSIONS ON QSKID OPERATION

We have described a Quantum Superconducting Kinetic Inductance Detector suitable for operation in a low background environment and compatible with LTS and HTS material technologies. The QSKIP responsivity and NEP are analyzed using the Hamiltonian energy functional and *linearized* Rothwarf-Taylor equations. The QSKIP is intended to operate at low temperatures, in the current state, and below H_{C1} to maximize photoresponsivity and to suppress flux flow and Johnson noise, present in resistive current operation. The noise remaining is due to phonon induced fluctuations in the Cooper pair population, and this noise is significantly reduced because at $T \ll T_C$ the population of PB phonons ($\hbar\Omega > 2\Delta(T)$) is very small. As in semiconductor based photoconductive quantum photodetectors, the QSKIP responsivity increases with the effective quasiparticle photoexcitation lifetime. Because the energy gap in superconductors (unlike the bandgap in conventional semiconductor photodetectors) is comparable to the energy of PB phonons, trapping of these phonons increases the effective quasiparticle lifetime and thereby maximizes the QSKIP photoresponsivity. The trapping of PB phonons in YBCO is very effective because, according to experiment, the PB phonons cannot travel in the "c" direction (toward the substrate) since such large energy phonon modes do not exist for the "c" direction. Thus, the PB phonons will be effectively prevented from escaping into the substrate and can only escape by lateral motion or anharmonic decay. The QSKIP is projected to have a spectral photoresponse up to $2\Delta(T)$, the superconductor's energy gap $\approx 32\mu\text{m}$ for YBCO at $T \ll T_C$. Such a wide spectral response is currently achieved only with thermal photodetectors. Operating the QSKIP at about 9K should provide very good performance to about $32\mu\text{m}$ with a calculated NEP of about 7×10^{-17} Watts.

2.3 DETECTOR FABRICATION

Fabrication of the hybrid LTS/HTS photodetector with readout involved finding a compromise between the disparate materials involved in LTS vs. HTS processing. Possible undesirable interactions between HTS and LTS-related areas include:

- Loss of oxygen from YBCO to other materials, such as Nb and SiO_x
- Diffusion of materials such as Si or Nb into the YBCO
- Degradation of the Nb junction properties due to the roughness of YBCO

In practice the most significant problem was deterioration of the YBCO T_c due to overlayers of SiO_x, which robbed oxygen from the YBCO. Removal of the SiO_x from the YBCO followed by an anneal resulted in recovery of the T_c to within a couple of degrees of the original value. This residual depression of T_c was presumably due to some diffusion of Si into the YBCO.

The initial process for a magnetically coupled photodetector and readout involved three such SiO_x depositions, which resulted in the T_c being suppressed to zero. Subsequent designs for a *direct-coupled* photodetector and readout involved only one such deposition. Depending on the particular YBCO film this typically lead to suppression of T_c by anywhere from zero to five degrees by this single step. In practice the sum total of all process steps resulted in suppression of T_c by as much as twenty degrees, a serious degree of degradation.

It should be noted that, in retrospect, an all-epitaxial approach, using only epitaxial insulators compatible with YBCO, would lead to less process-related damage to the YBCO than the hybrid LTS/HTS approach pursued on this program. Needless to say, this was not obvious at the outset of the program.

The remainder of this section discusses the processes developed for both magnetically coupled and direct coupled HTS/LTS photodetector/readout structures.

2.3.1 Magnetically Coupled Detector

The initial approach to the hybrid HTS/LTS photodetector was to have a YBCO photodetector on the bottom, then a layer of SiO_x to isolate the photodetector from an overlaid Nb SQUID readout circuit, which was in turn overlaid with another SiO_x layer to provide isolation from the top Au layer, which served as a light shield and contact layer. This approach is outlined in Figure 2.3, which also details the individual process steps involved.

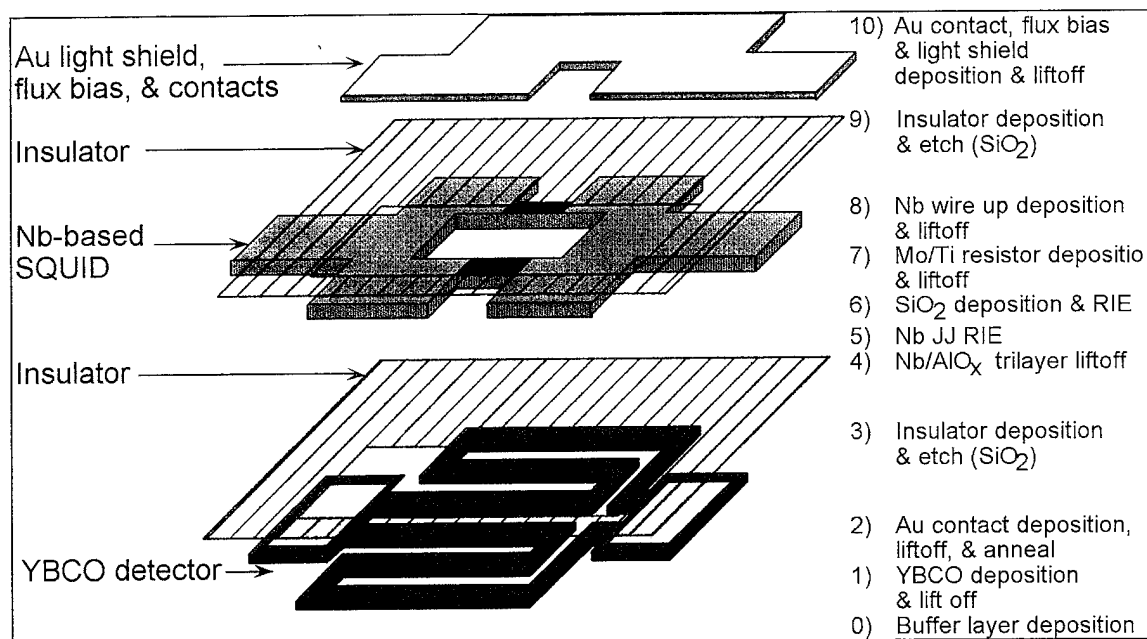


Figure 2.3 Schematic process sequence for HTS meander photodetector with magnetically coupled LTS SQUID readout. In practice the SQUID readout is accomplished with a series array of SQUIDs.

Two versions of this photodetector were fabricated on the wafer: one so-called “single-slit”, which had a simple loop of YBCO with a series array of Nb SQUIDs overlayed on the slit, and a “meander” version in which the SQUIDs were layed over the central slit of the meander. Mask drawings for the meander version are shown Figure 2.4, while Figure 2.5 shows a detail of the SQUID array on the single-slit version.

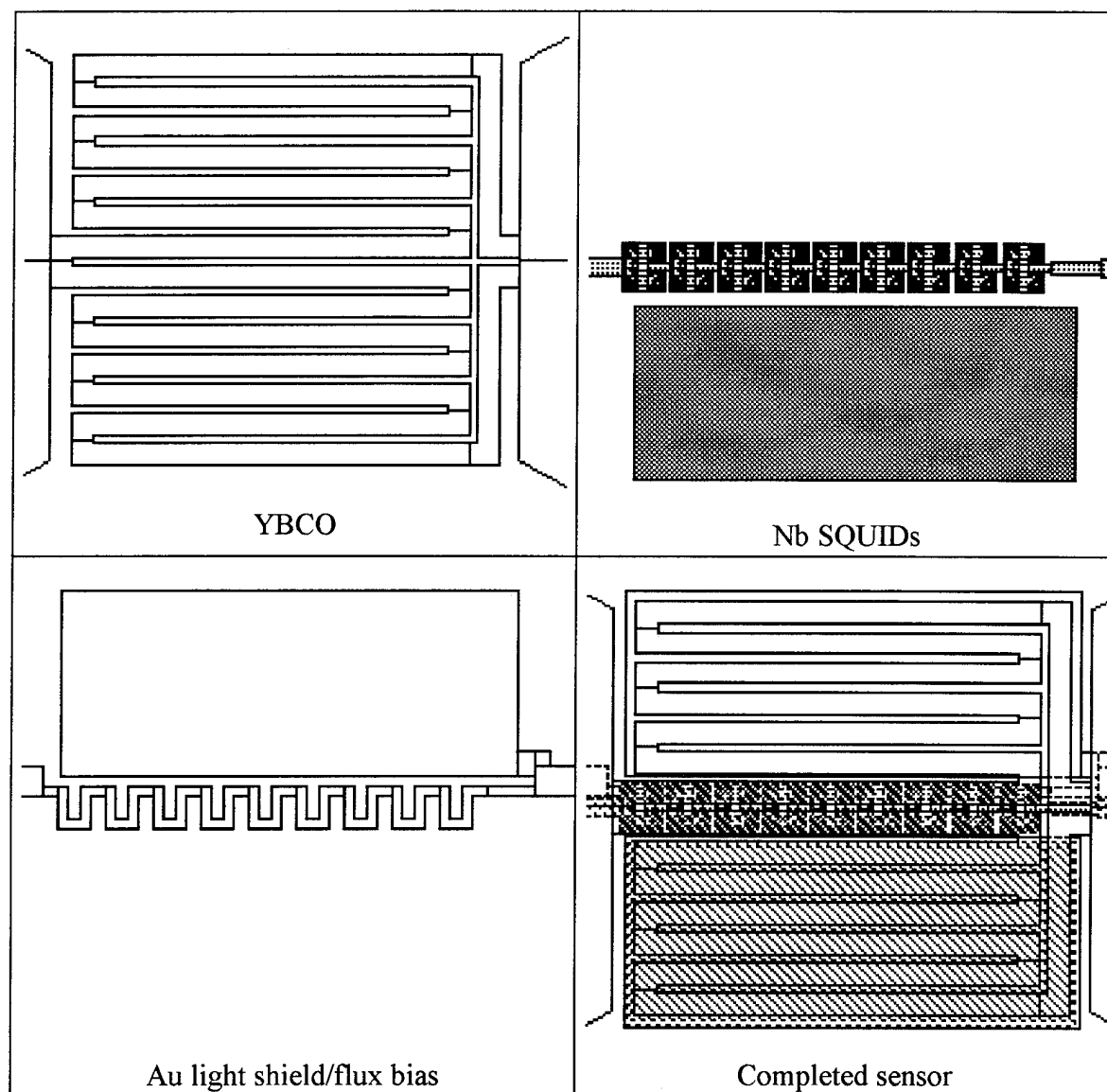


Figure 2.4 Excerpts from mask drawings for a YBCO meander photodetector with series array of Nb SQUIDs for readout.

One of the concerns at the start of the program was whether the quality of the Nb junctions would be compromised by the relatively rough surface of the YBCO below. This was not however a major problem.

From Figure 2.3 one can see that a total of three layers of SiO_x were required in this process, including one required for defining contact windows to the Nb junctions. Each deposition of SiO_x degraded the YBCO, resulting in it being non-superconducting by the time the process was completed.

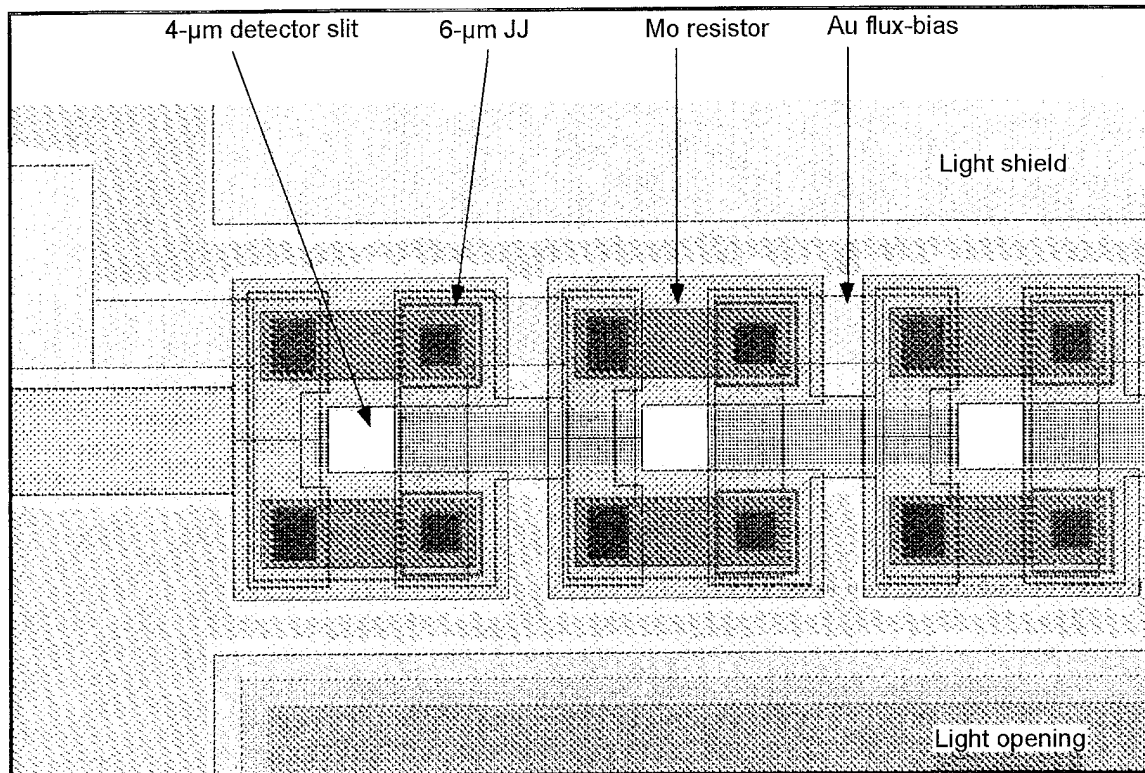


Figure 2.5 Detail of the mask layout for a magnetically coupled “single slit” photodetector and readout, showing three of nine SQUIDs in series. The Au flux-bias line meanders back and forth over the SQUIDs, and is used to set the desired operating point of the SQUIDs.

2.3.2 Direct Coupled Detector

Partly because of the problems with SiO_x , and because of a general desire to simplify the process, a new photodetector concept was invented — the direct-coupled photodetector, where the Nb SQUID makes direct electrical contact to the YBCO through a layer of in-situ Au. The layer of Au was necessary in order to ensure that the Nb would not steal oxygen from the YBCO. Such direct Nb-YBCO contacts, without Au, have extremely high contact resistance, of order $10^{-4} \Omega\text{-cm}$ or higher.

The fabrication sequence for the direct-coupled photodetector is illustrated Figure 2.6. The contact area between the Nb SQUID and YBCO photodetector was deliberately made large (more than $2000 \mu\text{m}^2$) in order to obtain a high enough critical current for the contact.

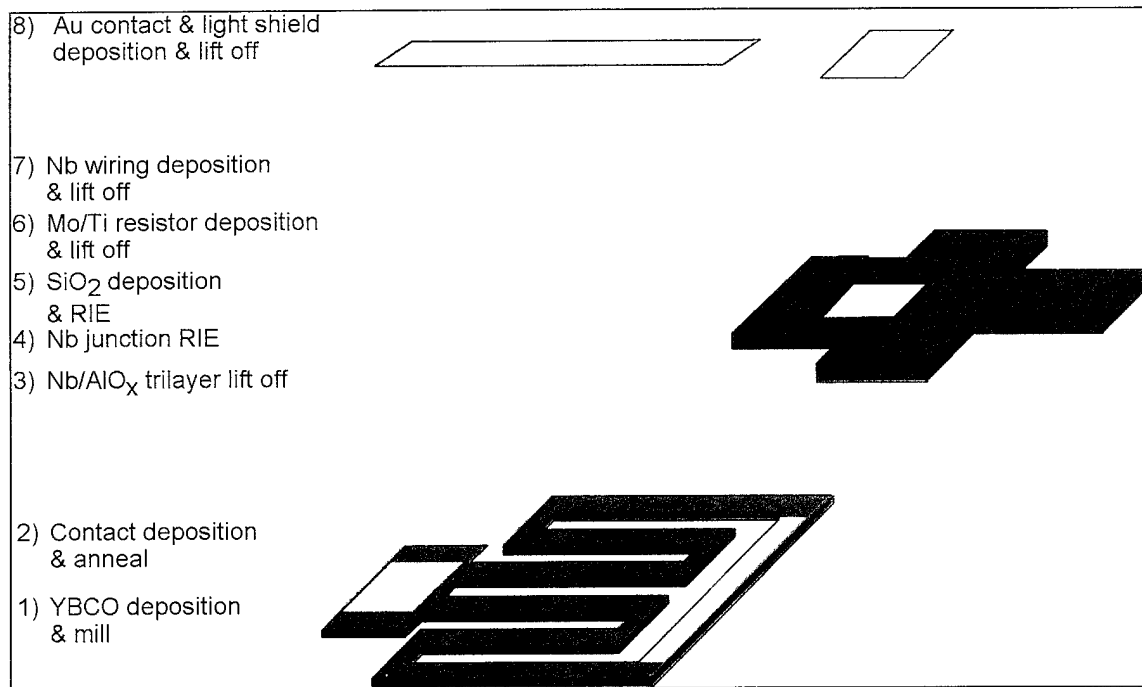


Figure 2.6 Schematic process sequence for HTS meander photodetector with direct-coupled LTS SQUID readout. Only one SiO_x layer is required in this process, in order to make contact windows to the Nb junctions.

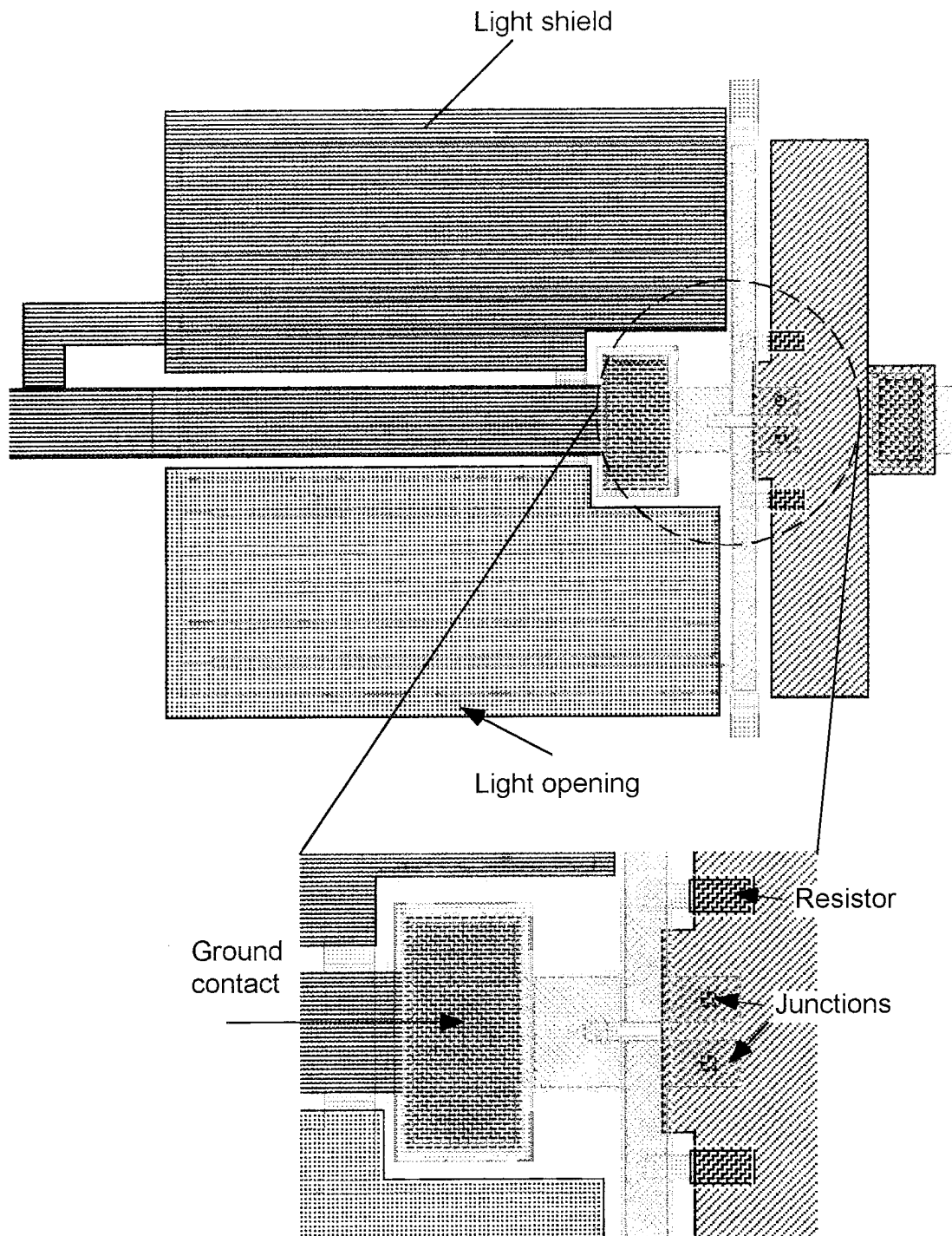


Figure 2.7 Section of the mask drawing for the direct-coupled photodetector, showing the meander path with light shield on one branch, and light opening (through the SiO_x) on the other branch, and a detail of the Nb SQUID and ground contact area.

2.4 REFERENCES

- ¹ R.A. Smith, F.E. Jones and R.P. Chasmar, **THE DETECTION AND MEASUREMENTS OF INFRA-RED RADIATION** (Oxford at Clarendon Press, NY, 1958), p 206.
- ² P.W. Kruse, L.D. McGlauchlin and R.B. McQuistan, **ELEMENTS OF INFRARED TECHNOLOGY: GENERATION, TRANSMISSION, AND DETECTION** (John Wiley and Sons, NY, 1962), p 354.
- ³ Y. Enomoto and T. Murakami, J. Appl. Phys., **59**(11), 3807 (1986).
- ⁴ J.G. Bednorz and K.A. Muller, Z. Phys. B **64**, 189 (1986); Rev. Mod. Phys., **60**, 585 (1988).
- ⁵ H. S. Kwok, J.P. Zheng, and Q.Y. Ying, Appl. Phys. Lett., **54**, 2473 (1989).
- ⁶ M. Leung, P.R. Broussard, J.H. Claassen, M. Osofsky, S.A. Wolf and U. Strom, J. Appl. Phys. Lett., **51**, 2046, (1987).
- ⁷ W.S. Brockelesby, D. Monroe, A.F.J. Levi, M. Hong, S.H. Liou, J. Kwo, C.E. Rice, P.M. Mankiewich and R.E. Howard, Appl. Phys. Lett., **54**, 1175 (1989).
- ⁸ M.G. Forrester, M. Gottlieb, J.R. Gavaler, and A.I. Braginski, IEEE Trans. on Magn., **MAG-25**, 1327, (1989).
- ⁹ A.M. Kadin, M. Leung, A.D. Smith, and J.M. Murduck, IEEE Trans. on Magn., **MAG-27**, 1540 (1991).
- ¹⁰ R. Kaplan, W.E. Carlos and E.J. Cukaukas, J. Appl. Phys., **67**, 4212 (1990).
- ¹¹ E.K. Track, M. Radpavar, S.M. Faris, IEEE Trans. Magn. **MAG-25**, 1096 (1988).
- ¹² N. Bluzer, United States Patents 5,179,072 and 5,185,527.
- ¹³ N. Bluzer and M.G. Forrester, presented at the 1994 Applied Superconductivity Conference, October 16-21, 1994, Boston, Mass., and published in: IEEE Transactions on Applied Superconductivity **5**(2), 2583 (1995).
- ¹⁴ N. Bluzer and M.G. Forrester, Optical Engineering, **33** No. 3, 697 (1994); N. Bluzer and M.G. Forrester, Journal of Superconductivity, **7**, No. 2, 395 (1994).
- ¹⁵ William L. Wolfe and George J. Zissis, Editors, **THE INFRARED HANDBOOK** (The Infrared Information and Analysis Center, Environmental Research Institute of Michigan, Revised Edition 1985) p19-45.
- ¹⁶ H. Goldstein, **CLASSICAL MECHANICS** (Addison-Wesley Publishing Co., Inc., Reading, Massachusetts 1950) Chapter 2
- ¹⁷ J.D. Jackson, **CLASSICAL ELECTRODYNAMICS** (John Wiley and Sons, Inc., New York, 1962) Chapter 6, p 181.
- ¹⁸ With the so called London gauge we set $A_{\perp}(X) = -\Lambda_{\perp}(X)$, where \perp denotes the normal component of the vector potential $A(X)$ and the current density $J(X)$ at all boundaries. Thus the canonical momentum $p = q_{CP}[\Lambda J_s(X) + A(X)]$ is equal to zero over the entire boundary and is given in terms of the condensate's phase angle θ as $p = i\hbar \nabla \theta = 0$. Hence θ is equal to a constant over the entire superconductor. Under these conditions $\Lambda J_s(X) = -A(X)$, where $\Lambda = m_{CP} / [\rho_{CP}(X) q_{CP}^2]$.
- ¹⁹ J. Bardeen, L. N. Cooper, and J. R. Schrieffer, Phys. Rev. **108**, 1175 (1957); M. Tinkham, **INTRODUCTION TO SUPERCONDUCTIVITY** (Robert E. Krieger Publishing Co., Malabar, FL 1985), Chapter 2.
- ²⁰ Dale Corson and Paul Lorrain, **INTRODUCTION TO ELECTROMAGNETIC FIELDS AND WAVES** (W.H. Freeman and Co. San Francisco, 1962) Chapter 6, p254.
- ²¹ W.H. Parker and W.D. Williams, Phys Rev. Lett. **29**, 924(1972).
- ²² A. Rothwarf and B.N. Taylor, Phys. Rev. Lett. **19**, 27 (1967).
- ²³ Since all the terms in the Rathwarf-Taylor equations use volume density, we choose to use volume density instead of area density for the photon flux. The photon volume density is obtained by dividing the nonreflected fraction of the incident photon flux by the QSKIP's thickness $d \approx 100\text{nm}$.
- ²⁴ A. A. Abrikosov, L.P. Gorkov, and I.E. Dzyaloshinski, **METHODS OF QUANTUM FIELD THEORY IN STATISTICAL PHYSICS**, (Prentice-Hall, Engelwood Clifs, NJ, 1993).
- ²⁵ M.Yu. Reizer, Phys. Rev. B **39**, 1602 (1989).
- ²⁶ M.Yu. Reizer, Phys. Rev. B **40**, 5411 (1989).
- ²⁷ N. Bluzer, Phys. Rev. B **46**, 1033 (1992); Phys. Rev. B **44**, 10222 (1991).
- ²⁸ N. Bluzer, IEEE Trans. Appl. Supercond. **3**, 2869 (1993).

- ²⁹ U. Fano, Phys. Rev. **70**, 44(1946)
- ³⁰ S.B. Kaplan, C.C. Chi, D.N. Lngenberg, J.J. Chang, S. Jafarey, and D.J. Scalapino, Phys. Rev. B **14**, 4854 (1976).
- ³¹ A.V. Sergeev and M.Yu.Reizer, "Nonequilibrium Superconducting Detectors of Electromagnetic Radiation," submitted to Phys. Rev. B.
- ³² J.W. Loram, K.A. Mirza, J.R. Cooper and W.Y. Liang, MOS Satellite Conference to LT-20 July 27-31, 1993. Journal of Superconductivity, Plenum NY.
- ³³ Eugene Mertzbacher, **QUANTUM MECHANICS**, (John Wiley, New York, 1960),p370
- ³⁴ W.A. Little, Can. J. Phys. **37**,334(1959).
- ³⁵ A. C. Anderson, in **NON-EQUILIBRIUM SUPERCONDUCTIVITY, PHONONS, AND KAPITZA BOUNDARIES**, edited by Kenneth E. Gray (Plenum, New York, 1980)p. 263.
- ³⁶ S. B. Kaplan, J. low Temp. Phys. **37**, 343(1979).
- ³⁷ A. Papoulis, **PROBABILITY, RANDOM VARIABLES, AND STOCHASTIC PROCESSES** (McGraw Hill Systems in Science Series, NY 1965), chapter 16.
- ³⁸ W.H. Parker, Phys. Rev. B, **12**, 3667 (1975).
- ³⁹ R.K. Willardson and A.C. Beer, Editors, **SEMICONDUCTORS AND SEMIMETALS**, Infrared Detectors Vol. 5 (Academic Press, New York 1970). p219
- ⁴⁰ B. Friedl, C. Thomsen, and M. Cardona, Phys. Rev. Lett. **65**, 915(1990).
- ⁴¹ R.E. Cohen, W.E. Pickett, and H. Krakauer, Phys. Rev. Lett. **64**, 2575(1990); R.E. Cohen, W.E. Pickett, and H. Krakauer, Phys. Rev. Lett. **62**, 831(1989).
- ⁴² H.E. Fisher, S.K. Watson, and D.G. Cahill, Comments Mod. Phys. B **14**(2), 65(1988).
- ⁴³ M. Nahum, S. Verghese, P.L. Richards, and K. Char, J. Appl. Phys. Lett. **59**, 2034(1991).
- ⁴⁴ See in particular Figure 5 in: W. Reichard, D. Ewert, E. Gering, F. Gompf, L. Pintschovius, B. Reneker, G. Collin, A.J. Dianoux, and H. Mutka, Physica B **156&157**, 897 (1989).
- ⁴⁵ Y. Iye, T. Tamegai, H. Takeya and H. Takei, Physica **148 B**, 224(1987).
- ⁴⁶ W. J. Gallagher, T. K. Worthington, T. R. Dinger, F. Holtzberg, D. L. Kaiser and R. L. Sandstorm, Physica **148 B**, 228, (1987).
- ⁴⁷ Y. Hidaka, M. Oda, M. Suzuki, A. Katsui, T. Murakami, N. Kobayashi, and Y. Muto, Physica **148 B**, 329 (1987).
- ⁴⁸ Charles Kittel, **INTRODUCTION TO SOLID STATE PHYSICS**, (John Wiley, New York, 1971), p. 255.
- ⁴⁹ A compilation of values for γ_p and $\Delta C/\gamma_p T_C$ obtained at different laboratories is given in table 1.6 of reference 42.
- ⁵⁰ C.M. Falco, W.H. Parker, S.E. Trullinger, and P.L. Hansma, Phys. Rev., **B10**, 1865 (1974).
- ⁵¹ H. Seppa, M. Kiviranta, A. Satrapinski, L. Gronberg, J. Salami, and I. Suni, IEEE Trans. on Appl. Superconductivity **3(1)**, 1816 (1992).
- ⁵² C.D. Tesche and J. Clarke, Journal of Low Temp. Phys. **29**, Nos.3/4, 301 (1977).

3.0 EXPERIMENTAL APPROACH AND MEASUREMENTS

In this section, we describe the experimental approach used and the measurements made. All the equipment and engineering effort used to design the experimental test station were done on Westinghouse funds. The experimental test station, shown in Figure 3.1, has a generic capability for making photoresponse measurements and its use is intended for use on several different programs as a spectrophotometer for measuring photoresponse of superconducting and semiconducting photophotodetectors. The operation of the test station and data recording is computer controlled using the LabView for Windows software package. The optics, designed to operate over a very wide spectral band ($3\mu\text{m}$ - $100\mu\text{m}$), are described in section 3.1. The cryogenics of the test station is designed to operate between 5-300K and is described in section 3.3. Such operating characteristics are compatible with testing superconducting quantum photodetectors under development on this program. Part of the experimental test station's electrical subsystem was specifically designed for interface with a SQUID readout from QSKIP, and this is described in section 3.2. A special packaging approach for handling the QSKIP was developed and this is described in section 3.4. Finally, in section 3.5. we describe the experimental results on the QSKIP.

3.1 OPTICAL SETUP

The optical setup, assembled on an aluminum breadboard table, includes: (1) a monochrometer, (2) reflecting optics, (3) cooled long pass filters, (4) optical windows, (5) thermopile reference sources, (6) black body source, and (7) chopper. A diagram of the optical setup, including the black body source, focusing optics, and monochrometer is

shown in Figure 3.2. Also included in this diagram are the location of the optical elements in the dewar. The optical elements in the dewar include: (1) a window, (2) cooled (77K) filters (and attenuators), (3) gold coated mirrors for sampling the incident and reflected optical beam onto thermopiles (not shown) at 77K, and (5) the sample location. The sample is located on a cold finger whose temperature can be varied from 5-300K. A description of the components used and their operation follows.

The **black body source** is made up of a tungsten filament operated at 2400K. The filament selected is from an OSRAM Halogen projector lamp part number HLX 64655 EHI. This lamp is rated to operate at 3400K and puts out 10^4 lumens for an average life of 50 Hours. The filament is enclosed in a quartz envelope and operates from a 24 DC power supply. To use this lamp as a black body source, we first removed the quartz envelope because it does not transmit much beyond $4\mu\text{m}$. The tungsten filament was enclosed in a specially made vacuum box that had provisions for replaceable optical windows and powering of the filament. The replaceable optical windows included KRS-5 ($0.6\mu\text{m}$ - $40\mu\text{m}$), clear ZnSe ($0.3\mu\text{m}$ - $18\mu\text{m}$), and single crystal silicon ($1.1\mu\text{m}$ - $300\mu\text{m}$, with a blocking band between $12\mu\text{m}$ - $40\mu\text{m}$). With these windows a very broad spectral band could be covered and in particular the $3\mu\text{m}$ - $100\mu\text{m}$ spectral band we are interested in.

To maintain a longer life, the tungsten filament was operated at a lower voltage than the rated 24 volts. The tungsten filament was enclosed in the vacuum box and evacuated. Next, the vacuum box was backed filled with an inert gas to a pressure of about 30 psi. This provided two advantages: (1) the window coating rate from the

tungsten filament was reduced, and (2) the filament could be run hotter. Out of Argon, Krypton and Xenon we selected Krypton because Xenon was too expensive. With this design the filament and the optical windows could be readily replaced.

Only **Reflective optics** are used to focus the black body radiation onto the monochrometer entrance slit. Two gold coated 90° off-axis paraboloidal mirrors (part # 02 POA 013), from Melles Griot, collimate and refocus the black body radiation onto the monochrometer's entrance slit. A metal blade chopper, located less than 3mm in front of the monochrometer entrance slit, when rotated modulates the black body radiation. The radiation entering the monochrometer is filtered by a grating before it emerges at the monochrometer's exit slit.

Six gold coated gratings spectrally filter and provide radiation within the $3\mu\text{m}$ - $100\mu\text{m}$ spectral band of interest. The six gratings are assembled on two turrets with each turret holding three gratings. The monochrometer, model SpectraPro-275 from Acton Research Corporation, holds one three grating turret at a time. Each turret is easily installed in the monochrometer and no realignments are required. This six grating set covers the $3\mu\text{m}$ - $100\mu\text{m}$ spectral band as listed in Table 3.1. Turret number 1 contains gratings (1) through (3) spanning $3\text{-}30\mu\text{m}$. Turret number 2 contains gratings (4) through (6) spanning $30\text{-}100\mu\text{m}$. The monochrometer is used to select a narrow wavelength band (with higher order harmonics) from the spectrally broad band black body radiation, and this optical signal is collimated at the monochrometer exit slit with a gold coated 90° off-axis paraboloidal mirrors (part # 02 POA 013), from Melles Griot. The collimated optical

signal is directed at the photodetector through an optical window in the dewar, see Figure

3.3.

#	Grooves /mm	Blaze wavelength	Acton part #	Operating Band	$\Delta\lambda$ (for 3mm slit)
1	150 g/mm	4 μ m	1-015-4	3-6 μ m	72nm
2	75 g/mm	10 μ m	1-075-10	6-16 μ m	144nm
3	20 g/mm	22.5 μ m	1-02-22.5	16-30 μ m	540nm
4	20 g/mm	45 μ m	1-02-45	30-55 μ m	540nm
5	13.3 g/mm	67 μ m	1-013.3-67	55-85 μ m	810nm
6	7.9 g/mm	112 μ m	1-07.9-112	85-168 μ m	1365nm

Table 3.1. The list of gratings and their operating characteristics used in this program. The first three gratings were mounted on turret number 1 and the next three grating were mounted on turret number 2.

Filter #	Part Number	Cut-on λ	Transmission @ λ Cut-on
1	PN LP-3000-F	3 μ m	5%
2	PN LP-6000-F	6 μ m	5%
3	4-8 μ m P-12	12 μ m	20%
4	5-10 μ m P-16	16 μ m	35%
5	8-16 μ m P-22	25 μ m	20%
6	15-25 μ m P-40	40 μ m	20%
7	30-40 μ m P-62	62 μ m	20%

Table 3.2. List of long pass filters use in the optical set-up. Filters number 1 and 2 were purchased from the Infrared Optical Products, Inc. Filters number 3,4,5,and 6 were purchased from Infrared Laboratories, Inc.

Inside the dewar, see Figure 3.3, the collimated optical is filtered to remove the higher order harmonics. Seven long pass filters are needed to operate over the 3 μ m-100 μ m spectral band, and these are listed in Table 3.2.

The filters, 1" in diameter, are mounted in an eight-position wheel and cooled to 77K. With a knob, mounted outside the dewar, we place one of the seven filters (or no filter) in the optical beam path. Cooling these filters to 77K greatly reduces their black body radiation. A second wheel, (cooled to 77K and located in front of the filter wheel

and inside the dewar) contains neutral density attenuators that pass 10% and 1% of the incident optical radiation. The second wheel is independently controlled with a second knob mounted outside the dewar. This two wheel arrangement allows us to filter out the higher order harmonics and attenuate the narrow-band optical signal. The combination of filters and gratings used for spanning the 3 μ m- 100 μ m spectral band is given in Table 3.3. The last column indicates the location of the filters in the wheel so the knob mounted outside the dewar can be used to set the dial at the appropriate number (or filter). Similarly, the description of the wheel with the attenuators is given in Table 3.4 and the knob's dial settings are listed in the last column.

Operating Band	# Grating & Part	Filter	Knob Setting
Open	n/a	None	240
3-6 μ m	(1) 1-015-4	PN LP-3000-F	340
6-12 μ m	(2) 1-075-10	PN LP-6000-F	440
12-16 μ m	(2) 1-075-10	4-8 μ m P-12	540
16-26 μ m	(3) 1-02-22.5	5-10 μ m P-16	640
26-30 μ m	(3) 1-02-22.5	8-16 μ m P-22	740
30-45 μ m	(4) 1-02-45	8-16 μ m P-22	740
45-55 μ m	(4) 1-02-45	15-25 μ m P-40	840
55-70 μ m	(5) 1-013.3-67	15-25 μ m P-40	840
70-85 μ m	(5) 1-013.3-67	30-40 μ m P-62	940
85-100 μ m	(6) 1-07.9-112	30-40 μ m P-62	940

Table 3.3. Arrangement of Filters and Gratings for operating in 3-100 μ m spectral band. Once the operating band is selected, the corresponding grating is rotated into place in the monochrometer and the appropriate filter in the dewar is rotated into the beam path with the knob on the dewar.

After being spectrally filtered inside the dewar, the filtered optical signal is divided into three parts. One part is reflected by a gold mirror and is used as a reference. A second part is reflected from a thin film held at the same temperature as the

photodetector. The thin film is the same material that the photodetector is made from. The third part of the filtered optical signal reaches the photodetector located on the cold finger.

Two thermopiles (operated at 77K and mounted on a cross member located inside the dewar's radiation shield, shown in Figure 3.3), are used to measure the intensity of the incident and reflected beams. With the measured intensities of the reflected and incident, the detector's normalized photoresponse is computed. Both thermopiles are model 2M, manufactured by Dexter Research Center. Improved thermopile responsivity is realized because they are operated in a vacuum and at 77K. The responsivity of both thermopiles have been calibrated with a HeNe laser. The responsivity of the thermopile used to measure the incident filtered optical signal is 1425.5 Volts/Watt. The responsivity of the thermopile used to measure the reflected optical signal from the photodetector is 1104.19 Volts/Watt. The thermopile output signals are amplified and recorded on a PC. The electrical setup is described in the next section.

Operating Band	Function	Characteristics	Knob Setting
3-100μm	Open	Open	910
3-100μm	Attenuator	1% Pass	810
3-100μm	Attenuator	10% Pass	710
3-100μm	Open	Open	610
3-100μm	Open	Open	510
3-100μm	Open	Open	410
3-100μm	Open	Open	310
3-100μm	Open	Open	210

Table 3.4. Arrangement of attenuators in the second wheel. Out of the eight positions in this wheel only two are used, for the 1% and 10% neutral density attenuators. With the two wheel arrangement, these attenuators can be placed in series with the filters to vary the intensity of the filtered optical beam.



Figure 3.1. Shown is the experimental test station for measuring photodetector photoresponse. The dewars shown in the background are used to cool the radiation shield to 77K and the cold finger as low as 5K. Also visible are the electronics, dewar, optics and computer control.

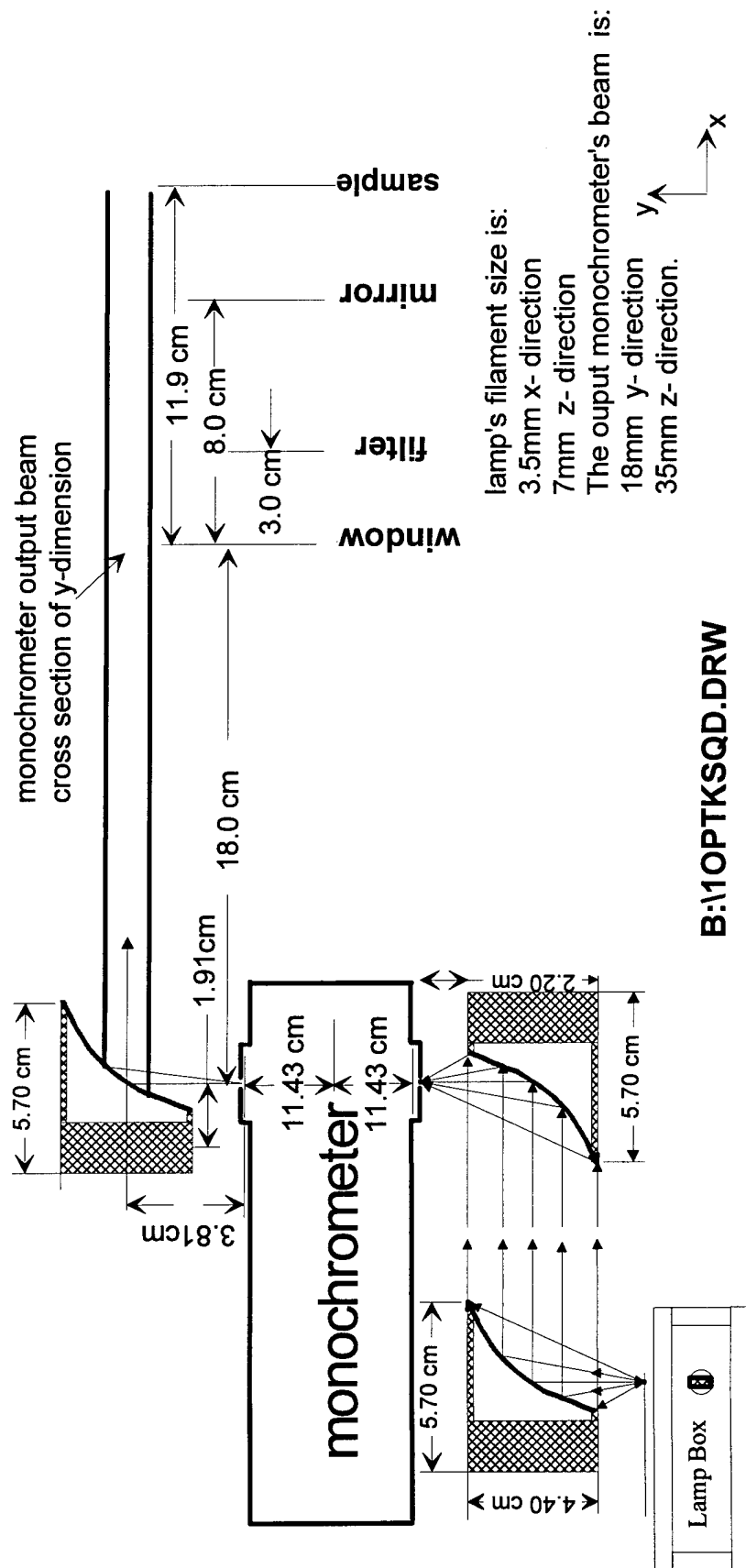


Figure 3.2. The layout of the optical system is shown, including: the monochrometer, the paraboloidal mirrors, and the location of the dewar components.

Technical drawing of the radiation shield components for the Superconducting Proton Accelerator. The drawing shows a cross-section of the shield assembly, including the radiation shield, LN (liquid nitrogen) cooling system, sample clamp, cross member, window, and vacuum jacket. Dimensions are provided in inches. Labels include: First Stage at 77K, LN, Radiation Shield, Sample Clamp, cross member, Window, Vacuum Jacket, Dual Filter Wheel Assembly, and Radiation Shield's Top.

Table Top

3.2 ELECTRICAL SETUP

The electrical setup included provisions for: (1) PC computer data acquisition, (2) signal processing electronics, (3) photodetector bias circuits, (4) electrical interface to optical elements, and (5) temperature control and monitoring. A significant effort was required for the electrical subsystem and this is described next.

PC computer data acquisition is used to control the entire experimental setup. A PC with a 486 microprocessor is used to operate the equipment through the GPIB. Incorporated into the PC are two cards made by National Instruments: (1) an AT-GPIB interface for IBM PC/AT EISA Bus PC including NI-488.2, and (2) a multifunction Analog and Digital I/O Bus for IBM PC, model AT-MIO-16L-25. The computerized data acquisition software is based on National Instruments LabView for Windows. All the electronics are initialized through the PC computer interface, with provisions for a manual override. The initial settings have been programmed into the Virtual Instruments (VI) formed with the LabView software. The VI incorporates all the electronic instruments on the PC CRT screen and provides control knobs for operating these through an GPIB. Once the photodetector sample has been cooled and properly biased, the data recording is made with the PC computer. The PC computer reads many different parameters from the instruments and these are listed in Table 3.5. The reason for all these reading follow.

The first three rows are used to establish the AC incident photon flux. The incident flux is measured with a thermopile when the chopper blade is open and closed.

The difference between these reading gives us the change in photon flux and this is used to compute the AC photocurrent response. The AC measurement is used to remove the photon background which is very significant in the 3-100 μ m spectral band.

#	Label	Purpose
1	High Incident Photon Reading	Incident flux recording with chopper blade open
2	Low Incident Photon Reading	Incident flux recording with chopper blade closed
3	Delta 1-2 COMPUTATION	Incident flux AC amplitude computation
4	High Reflected Photon Reading	Reflected flux recording with chopper blade open
5	Low Reflected Photon Reading	Reflected flux recording with chopper blade closed
6	Delta 4-5 COMPUTATION	Reflected flux AC amplitude computation
7	Detector High Voltage Reading	Voltage across detector with chopper blade open
8	Detector Low Voltage Reading	Voltage across detector with chopper blade closed
9	Delta 7-8 COMPUTATION	Voltage change across SC should remain ZERO
10	Detector High Bias Current	Measures bias current with chopper blade open
11	Detector Low Bias Current	Measures bias current with chopper blade closed
12	Delta 10-11 COMPUTATION	Insures bias current remains the same
13	Detector Temperature	Reads the detector's temperature
14	SQUID Temperature	Reads the cold finger's temperature
15	Cold Shield Temperature	Reads the radiation shield's temperature
16	Thermopile Temperature	Reads the thermopile's temperature
17	SQUID Bias Current	Ic SQUID bias current
18	SQUID High Current Reading	Current used to balanced SQUID with blade open
19	SQUID LOW Current Reading	Current used to balanced SQUID with blade closed
20	Delta 18-19 COMPUTATION	AC photocurrent amplitude
21	Photon Wavelength	Provides spectral band of incident photon flux
22	DC Lock-in Null Signal	Error signal, zero if 18 & 19 are adjusted OK
23	SQUID Flux Bias	Net SQUID bias including Lock-in error signal
24	Lamp Voltage	DC Bias voltage on Black Body lamp source

Table 3.5. List of readings and computations produced with the computerized data acquisition system used to measure the photodetector's photoresponse and tabulated in 24 rows.

Rows 4 through 6 are used to establish the AC reflected photon flux. The reflected photon flux is measured with a thermopile with the chopper blade open and closed. The reflected photon flux is normalized by the corresponding incident photon flux. The

difference between these readings should yield the percentage of photon signal which is reflected. With the AC reflected photon signal calculations are made to compute how much photon flux is absorbed by the photodetector to produce the observed photocurrent signal.

Rows 7 through 9 are used to monitor the voltage across the superconducting photodetector. Two readings are made, one with the chopper blade open and a second one with the chopper blade closed. If the superconducting photodetector remains in the zero resistance state (or current state) the difference between these two readings should be zero. Taking a difference between two reading circumvents the issue of removing DC offsets present in the voltage reading. If the difference between the two readings is not zero it signifies that the photodetector is not operating in the zero resistance state.

Rows 10 through 12 are used to monitor the current bias of the superconducting photodetector. Two readings are made, one with the chopper blade open and a second one with the chopper blade closed. If the superconducting photodetector remains in the zero resistance state (or current state) the photodetector difference between these two readings should be zero. Taking a difference between two readings circumvents the issue of removing DC offsets present in the reading. The combination of the voltage and current readings is our check to ensure that the photodetector remains in the zero resistance superconducting state with different levels of photoillumination.

Rows 13 through 16 provide temperature information on the photodetector and dewar. Row 13 represents the temperature from a diode thermometer mounted inside a leadless chip carrier package containing the photodetector. Row 14 is the temperature of

silicon diode sensor thermally attached to the cold finger. The temperature of the radiation shield is recorded on line 15 and we assume that it corresponds to the temperature of the thermopiles which are attached to the radiation shield. Row 16 has provisions for adding a second temperature sensor for specifically measuring of the thermopiles temperature, which are bolted to the cross member in the radiation shield.

The SQUID bias current is recorded in row 17. The bias current is manually adjusted for placing the SQUID in the voltage state and at maximum sensitivity.

Rows 18 through 20 monitor the needed offset current for balancing the photodetector signal and placing the SQUID in the symmetrical operating mode. The offset current is adjusted with the chopper blade open (Row 18) and the chopper blade closed (Row 19). The difference between these readings (Row 20) represents the photodetector's AC photoresponse current. This photoresponse is normalized with the incident flux level obtained from Rows 1-6. The number of photons incident are calculated from the wavelength (Row 21) and the spectrophotometer spectral bandwidth $\Delta\lambda$ given in Table 3.1.

The total offset current flowing in the SQUID is automatically trimmed with a Lock-in feedback circuit and the trim offset current level is given in Row 22. The total offset current is a sum of the manually adjusted offset current level and the Lock-in contribution, and this is given in Row 23. The voltage used to power the black body tungsten lamp is listed in Row 24.

It should be evident that each data point recorded with the computer data acquisition system is extensive. Such a practice permits better data analysis and proper operation of the superconducting photodetectors.

The **Signal Processing Electronics** consist of custom made preamplifiers and off-the-shelf electronics. The custom made preamplifiers, housed inside a breakout box attached to the dewar, provide gain to improve noise immunity to outside interference. The output from the preamplifiers is channeled to the computer data acquisition system through off-the-shelf electronics.

The off-the shelf signal processing electronics include: (1) a Keithley 182 nanovolt meter with an IEEE 488 interface, (2) a Keithley 705 scanner with a 7160 nanovolt scanner card and IEEE 488 interface, and (3) an Ithaco 3970 electro optical Lock-in measuring system. These instruments receive the outputs from the preamplifiers connected to the superconducting photodetector as shown in Figure 3.4. The photodetector is located inside the dashed lines labeled inside vacuum jacket in Figure 3.4.

The **photodetector bias circuits** are illustrated in Figure 3.4 and the details are shown in Figure 3.5. A DC current $I(\text{QSKIP})$ biases the photodetector. The signal developed is sensed with a SQUID located at the photodetector base. The SQUID is biased with a DC current I_C (SQUID). The construction of the photodetector and the readout SQUID are symmetrical to provide a differential output between the illuminated and covered portions of the photodetector. With such a differential operation, the SQUID bias circuits provide bi-directional flux bias (see Figure 3.5) that apply positive and

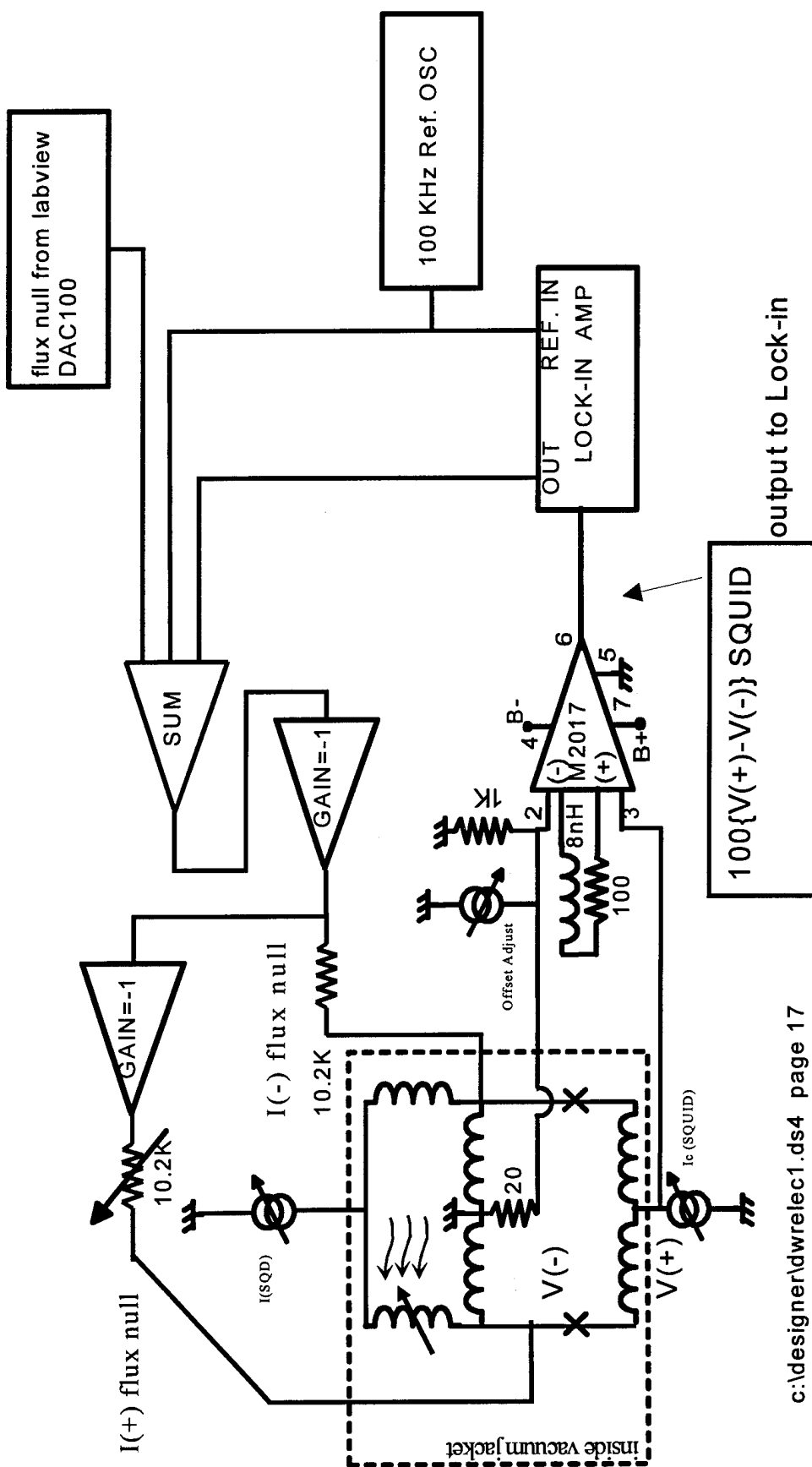


Figure 3.4. Diagram of preamplifier, Lock-in and photodetector bias circuits used for making photoreponse measurements.

negative currents to different ends of the SQUID. The combination of offsetting positive and negative SQUID bias currents minimizes ground currents. The bi-directional DC and AC flux modulating currents are produced through two $10.2\text{K}\Omega$ resistors. The amplitude and phase of the SQUID flux nulling currents are adjusted to be equal in amplitude and 180° out of phase with a variable resistor and capacitor (see Figure 3.5). The flux nulling circuits sum three inputs. These inputs are the AC flux modulation signal, the V(+) null signal from the Lock-in and the manually controlled DC SQUID flux bias adjust from the Lab-view DAC. Since the photodetector is DC coupled to a high gain preamplifier circuit, provisions have been included for manually removing any DC offsets that may saturate the preamplifier. An "offset adjust" current through a 20Ω resistor provides a small voltage at the preamplifier inputs to null out any DC offset. The preamplifiers are directly coupled to the SQUID to facilitate characterization of the SQUID's I-V curves. The SQUID preamplifier is an audio amplifier with a spectral voltage noise density of less than $1\text{nV}/\sqrt{\text{Hz}}$.

The **electrical interface to optical elements** includes: the monochrometer, the chopper, the black body tungsten filament, and the thermopiles. The Acton Research monochrometer has an electronic control module that interfaces through an IEEE 488 bus with the PC computer to record the operating wavelength. The HMS light beam chopper 220 interfaces to the computer through the National Instruments AT-GPIB interface for IBM PC/AT EISA Bus PC including NI-488.2. The Black body tungsten filament is powered by a remote controlled Sorensen SRL 20-12 power supply (0-25VDC, 0-15 Amp). The Sorensen power supply is controlled manually or with an automatic option.

The output of the supply is adjusted to maintain a fixed photon flux level as determined by the thermopiles inside the dewar. The thermopiles are connected to special preamplifier circuits with a gain of 11 (see Figure 3.6) and are calibrated to read the incident photon flux power. To extend the thermopiles' frequency response, the coaxial shield's effective shunting capacitance is reduced by the preamplifier circuits.

The **temperature control and monitoring** is centered around two Lake Shore 93CA temperature controllers connected via an IEEE 488 bus to a PC. Each controller accepts inputs from two temperature sensors and can power one heater. The heater output in combination with either temperature sensors provides for temperature control. The heater output is a proportional analog signal (not digital) to minimize heater induced electrical interference. The temperature sensors are calibrated silicon diodes with a temperature range between 2K and 300K. The sensor's calibration curves are entered inside the 93CA to provide, at low temperatures, a resolution better than 0.1K.

3.3 CRYOGENIC SETUP

The dewar used in this setup was a model MTD 150 made by Lake Shore Cryotronics (see Figure 3.3). The dewar includes 100 coaxial electrical inputs for electrical access to the packaged sample. The dewar includes a socket designed to accept packaged devices in a leadless chip carrier (LCC) 84 pin package. A square hole is machined inside the socket to accommodate an aluminum pedestal which is attached to the cold finger. Several modifications were made to this dewar and they are described.

The original dewar arrangement made use of a single clamp to make electrical and thermal contact between the LCC package and the dewar's socket and aluminum

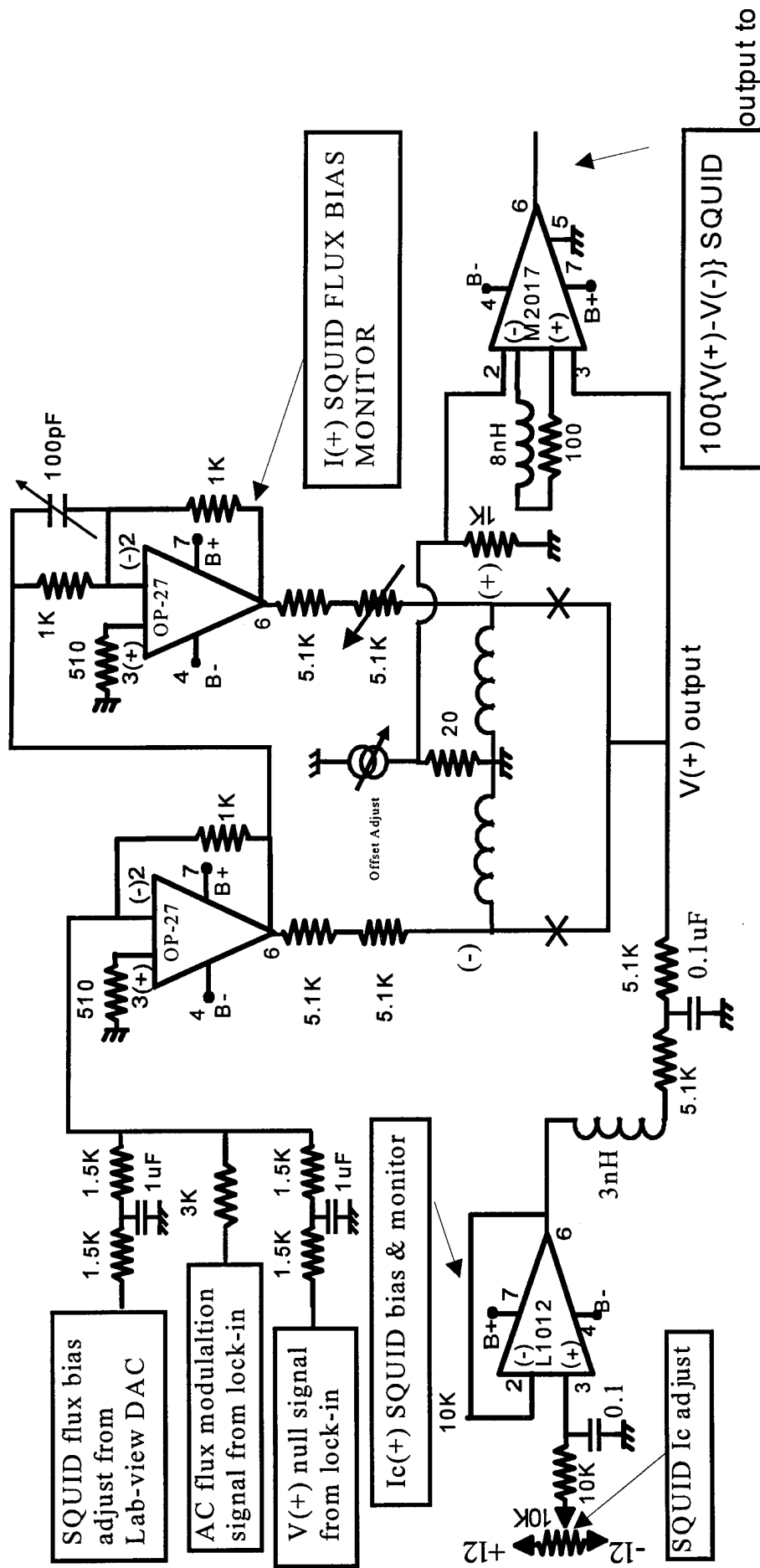


Figure 3.5. Details of: (1) bias circuits used for biasing the photodetector and the SQUID, (2) the SQUID preamplifier readout circuits, and (3) circuits for monitoring the SQUID critical current I_C and the flux bias.

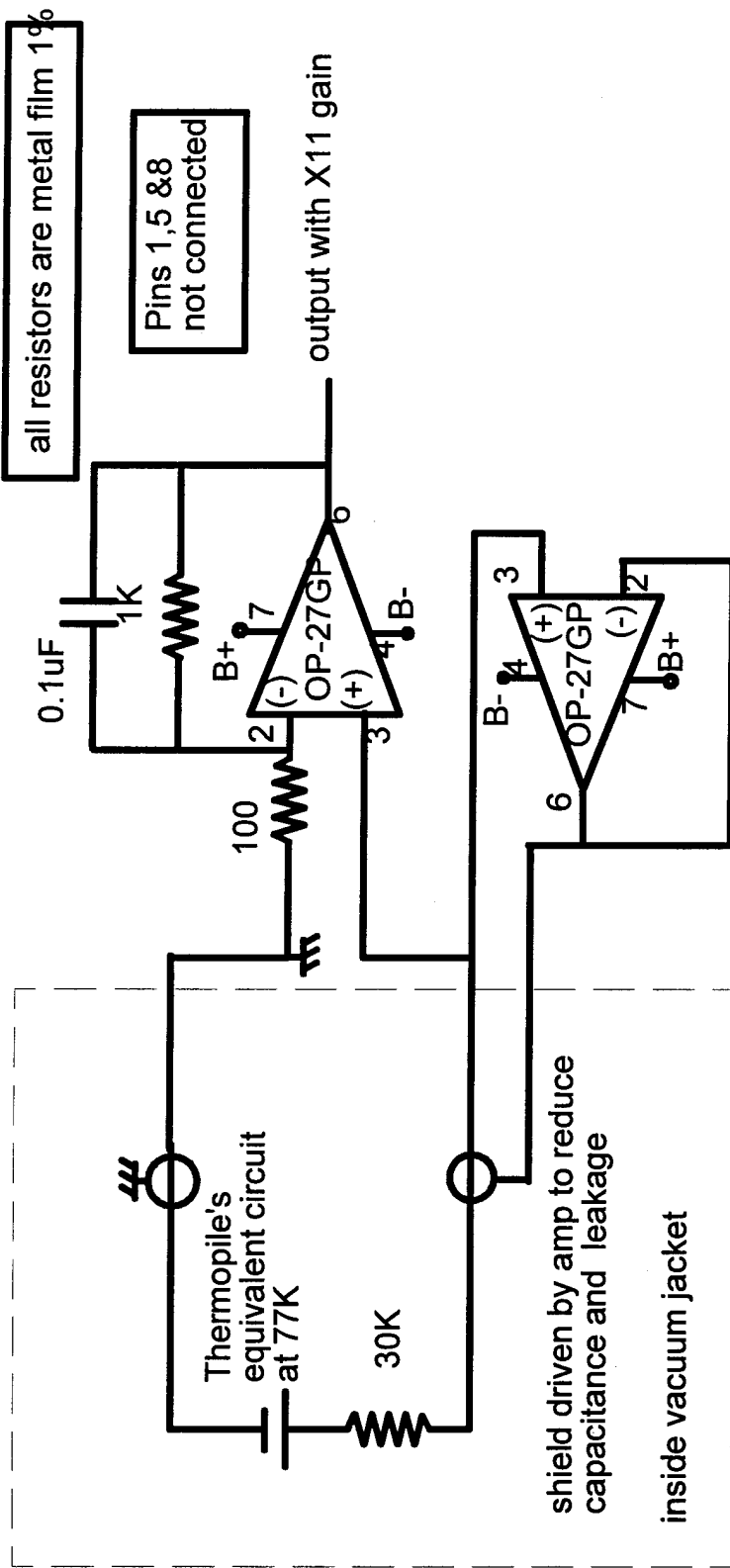


Figure 3.6. Circuit diagram of preamplifiers used to readout the thermopiles. One amplifier provides a voltage gain of 11 to the thermopile output signal. A second amplifier drives the coax shield to reduce the effective shunting capacitance across the thermopile and thus extend the frequency response.

pedestal. We have incorporated two independent pressure clamps to electrically and thermally contact, respectively, the LCC package to the socket and the aluminum pedestal. The LCC socket is soldered to a small printed circuit board which is attached to a second fan-out board with flexible thin wires. The small printed circuit board has provisions for attaching a clamp that clamps down the LCC package inside the socket. This clamp is independent of a second clamp which is used to press the package/socket assembly onto the aluminum pedestal and make good thermal contact. With two spring loaded clamps good electrical and thermal contact are independently established. This is important given the fact that the packaged devices are loaded into the dewar at room temperature and cycled between 5-300K. Cycling devices over such a wide temperature range requires provisions for accommodating mechanical mismatches in the thermal expansion coefficients. The two clamps provide the additional degree of freedom to accomplish this feature.

The modified dewar included two separate cryogenic inputs. The radiation shield, the two filter wheels, and the thermopiles were cooled by liquid nitrogen through separate cryogenic lines. This permitted us to cool most of the dewar mass with liquid nitrogen and saved both cool down time and liquid helium consumption. The second cryogenic input was from liquid helium that allowed us to cool the sample to about 5K. In operation, liquid nitrogen and liquid helium were transferred at the same time to speed up cool down. After cool down, the liquid nitrogen valve was turned off and the radiation shield remained close to 77K. The cold finger temperature was varied between 5-77K.

To reduce electrical interference, a Mu-metal magnetic shield was incorporated in the dewar. The shield, purchased from Advance Magnetics, was custom designed and made from RMA 1084 material. The shield was assembled from several pieces so it could be incorporated into the dewar. As designed the shield was easily added to the dewar after all the electrical, cryogenic, vacuum, and optical elements were incorporated.

As configured, the dewar was routinely used to cool down and measure photodetectors down to 5K. However, operation at 5K required reducing the thermal load from the 100 coaxial lines. For testing single photodetectors, 25 coaxial lines were sufficient and 75 coaxial lines were disconnected from the cold finger stage to significantly reduce the thermal load. The 75 lines can be readily reattached by removing three plastic inserts.

3.4. DETECTOR PACKAGING

Testing of LWIR QSKIP IC requires provisions for dealing with large thermal expansion mismatch between the photodetector and package material. Additionally, operation at liquid helium temperatures requires excellent thermal contact between the package and the cold finger. We developed a method, on Westinghouse funds, for packaging superconducting IC's in modified ceramic packages which resolve the thermal expansion mismatch and thermal drops across the package.

The solution we have developed solves: (1) the thermal expansion mismatch, and (2) thermal drops across the package. The packaging approach is compatible with conventional bonding of integrated circuits into packages that fit in conventional sockets.

The socket used is for an 84 pin LCC package, Kyocera part number PB-0289, and is integrated into the Lake Shore Cryotronics MTD-150 open cycle dewar.

The thermal mismatch is resolved by using a metallic base material (for good thermal conductivity) that has an thermal expansion coefficient close to the substrate the superconductor material is grown on. YBCO is typically grown on LaAlO_3 and NdGaO_3 substrates. Table 3.6 lists thermal expansion coefficient for several materials. For a LaAlO_3 substrate, beryllium, niobium and tantalum offer very good thermal matches (1300 vs 1300, 1290, and 1279). Niobium and tantalum are potentially a good choices. However, as niobium becomes superconducting at 9.2K (vs 4.43K for tantalum) its thermal conductivity also begins to decrease drastically at 9.2K. For operating down to about 4.5K it is better to use tantalum and this is out choice material.

MATERIAL	$\Delta L/L \times 10^6$	MATERIAL	$\Delta L/L \times 10^6$
LaAlO_3	1300	SS Monel	2450
Niobium	1290	SS 301	2300
Tantalum	1270	SS 321	2600
Molybdenum	894	SS 316	2770
Iron Fe	1890	SS 304	2790
Beryllium	1300	Titanium	1700
Aluminum	3910	Poly-Alumina	791

Table 3.6. Total thermal contraction difference $\Delta L/L$ between 300K to 77K for different candidate substrate.

Incorporating a tantalum base into the 84 pin LCC alumina package requires package modification. A 1 cm diameter hole was drilled in the 84 pin LCC package to remove the alumina that the IC is normally mounted on (see 3.7). The hole was

sufficiently small to be confined within the package well and thus not damage the electrical lines inside the package. The hole removes the bottom of the IC well which is replaced by the tantalum base(see Figure 3.7).

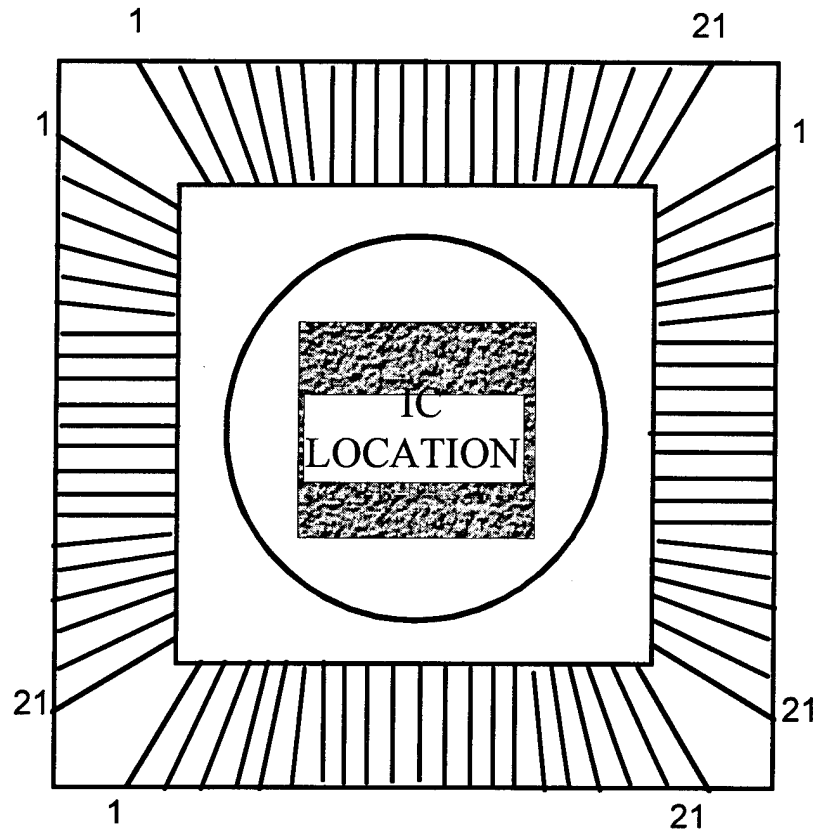


Figure 3.7. Schematic of 84 pin leadless chip carrier package with hole drilled in IC cavity. The hole, indicated by the circle, is 1 cm in diameter, which is sufficiently large for the IC to fit inside.

The base is made from a thin (about 0.05cm thick) tantalum sheet cut into a 2.4 cm square. The 2.4 cm square size is sufficiently small to fit within the electrical contact frame located on the back of the ceramic package, about 2.86 cm square. The processing and assembly needed to incorporate this tantalum base are described next.

A tantalum sheet is first plated with about 10 μ m of copper on both sides and then cut into 2.4 cm small squares. The plated tantalum squares receive about 120 μ m of

Indium on the front side, for a total base thickness of about 620 μ m. The LWIR QSKIP devices are soldering to the indium-coated tantalum base. The soldering is performed by placing the LWIR QSKIP device (with a gold coated back) on a SnInCd solder preform in the center of the indium-coated tantalum base. This assembly is placed into an oven and heated to 130°C and cooled to room temperature. This thermal cycle solders the LWIR QSKIP device to the indium-coated tantalum base with the SnInCd solder whose melting temperature is 95°C. The tantalum base with the LWIR QSKIP device is glued to the back of the ceramic package as shown in Figure 3.8.

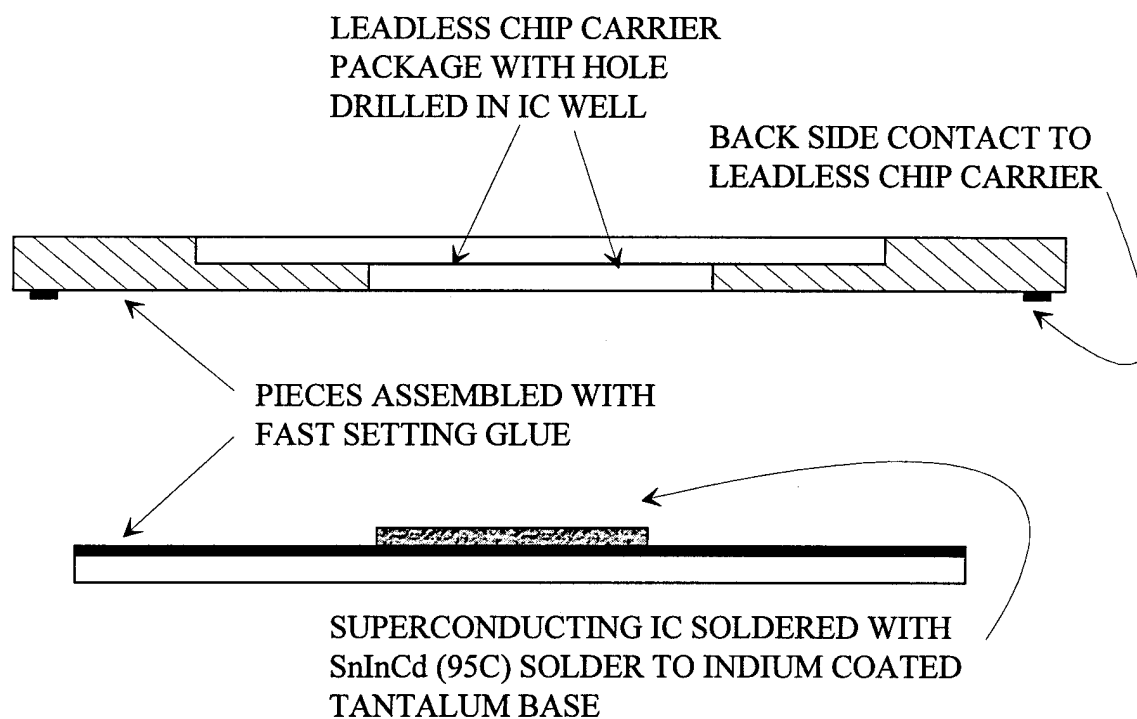


Figure 3.8. Illustration of assembly of indium-coated tantalum base, with IC attached, before being glued to back of ceramic package.

With this assembly, the soft indium, located between the tantalum base and the alumina LCC package, provides mechanical compliance to accommodate thermal

expansion mismatch. The fast setting glue, (Super Bonder 495 made by Loctite) is used for ease of assembly. When the LWIR QSKIP device, the tantalum base, and package are assembled, ultrasonic bonding is used to bond the LWIR QSKIP to the LCC package frame. The completed assembly is shown in Figure 3.9, with the electrical contact pads exposed on the back. With this arrangement, the electrical contact between the socket and LCC package is through the original contact pads, located on the package's back side.

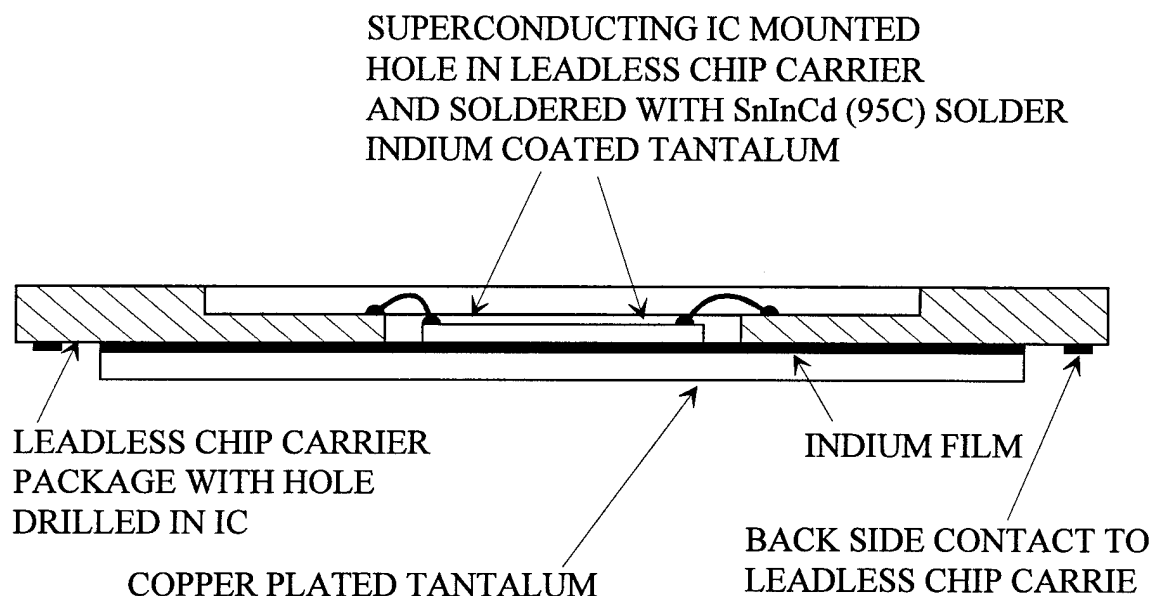


Figure 3.9. Assembly of Tantalum base, with IC soldered to it, glued to the back of a ceramic package pre-drilled with a hole in the IC well.

The packaging scheme has been implemented and LWIR QSKIP devices have been placed in a dewar and cooled down to about 5K. Unlike previous approaches, the LWIR QSKIP device did not sheer off the tantalum base after several cycles between 300K and 5K. This is a significant improvement over previous attempts where the QSKIP was

placed directly inside a 84 pin ceramic package. This technique is appropriate for packaging different IC made with high and/or low temperature superconductors.

3.5 DETECTOR TESTING AND RESULTS

The LWIR QSKIP fabricated and tested in this program is represented by the diagram shown in Figure 2.2 and the photograph shown Figure 3.10. In this section we start with an analysis specific to this photodetector structure and follow with experimental measurements taken on photodetectors pictured in Figure 3.10. The LWIR QSKIP did not exhibit photoresponse to light and we examine potential reasons for this.

The device pictured in Figure 3.10 includes a YBCO photodetector with a niobium readout SQUID located at the bottom. The photodetector is symmetric with each side configured into a serpentine pattern to increase the kinetic inductance. One side of the photodetector is shielded with a gold light shield and the other side exposed to light. The SQUID readout consists of two resistively (by 1Ω) shunted Nb/ Al_2O_3 /Nb Josephson tunnel junctions.

In operation, the serpentine photodetector is biased by a DC current. The $0.1\mu\text{m}$ thick YBCO photodetector occupies a $100\mu\text{m} \times 100\mu\text{m}$ square. Each serpentine branch is about $700\mu\text{m}$ long and $11\mu\text{m}$ wide. For this geometry, the resistivity of undegraded YBCO lines should be about $300\mu\Omega\text{-cm}$ at 300K. However, we have measured more than six devices and each one exhibits a resistivity of $1800\mu\Omega\text{-cm}$ at 300K. This resistivity is six times higher than the expected nominal value of $300\mu\Omega\text{-cm}$. Also, with

processing the YBCO films' transition temperature degrades from 90K to about 60K (see Figure 3.11). These changes in resistivity and transition temperature are evidence that the YBCO LWIR QSKIP processing causes damage to the YBCO superconductor.

We attribute the processing damage to the YBCO films primarily to the silicon dioxide layer covering the YBCO. The sputtered silicon dioxide provides for electrical isolation between the gold interconnect lines and the YBCO film. The first LWIR QSKIP devices fabricated had YBCO that was not superconducting down to 5K. It was determined that the sputtered silicon dioxide films were silicon rich. The excess silicon in silicon rich silicon dioxide is expected to leach oxygen from the YBCO films. Experiment were run to add oxygen to the Argon sputtering gas with the expectation of realizing stoichiometric silicon dioxide. With this approach, the processed YBCO remained superconducting after processing albeit they exhibited a reduced transition temperature. We stripped the oxide from these YBCO films and attempted to reoxygenate these film. Thermal cycles in oxygen ambient at 400C did not increase the YBCO films transition temperature to 90K. The reduced transition temperature remained leading us to conclude that some silicon has diffused into the YBCO sample and was irreversible. Careful tuning of the silicon dioxide deposition improved the YBCO films. The latest YBCO films remained superconducting after all the processing, which incorporate the niobium SQUID. However with the reduced transition temperature and increased resistivity we believe that the degraded superconducting characteristics have also produced a significant degradation in the quasiparticle lifetime and hence no photoresponse was observed. A solution to the YBCO degradation is to use epitaxial

SrTiO₃ as the insulator and passivation layer over the YBCO films. Such a process is being developed in the laboratory.

The SQUID built into the LWIR QSKIP was from niobium. This was selected to reduce the risk of using a YBCO SQUID. With the niobium SQUID noise and performance issues are well understood, thus leaving only the YBCO photodetector as an unknown. The niobium SQUID incorporated with the YBCO photodetector operated. At 5K, the critical SQUID junction current was about 0.2mA. The SQUID I-V curves are shown in an oscillograph in Figure 3.12. The SQUID was modulated by a magnetic flux and the modulation is shown in Figure 3.13. The inductance of the SQUID loop was about 10pH, consistent with our design goals.

In conclusion, the calculation reveal that the LWIR QSKIP device should provide excellent performance with an NEP of about 10^{-17} Watts and operate over a very wide spectral bandwidth. For YBCO, the expected photoresponse cutoff wavelength is expected to extend to about 30-40 μ m. On this program, we have developed performance models and photodetector structures which should provide the base for future demonstration of superconducting quantum photodetectors. With the development of improved fabrication, and QSKIP designs this photodetector will be demonstrated. The main improvement for QSKIP design is a reduction of the magnetic field inductance relative to the kinetic inductance. Both process and design improvements are being pursued and we expect positive results in the near future.

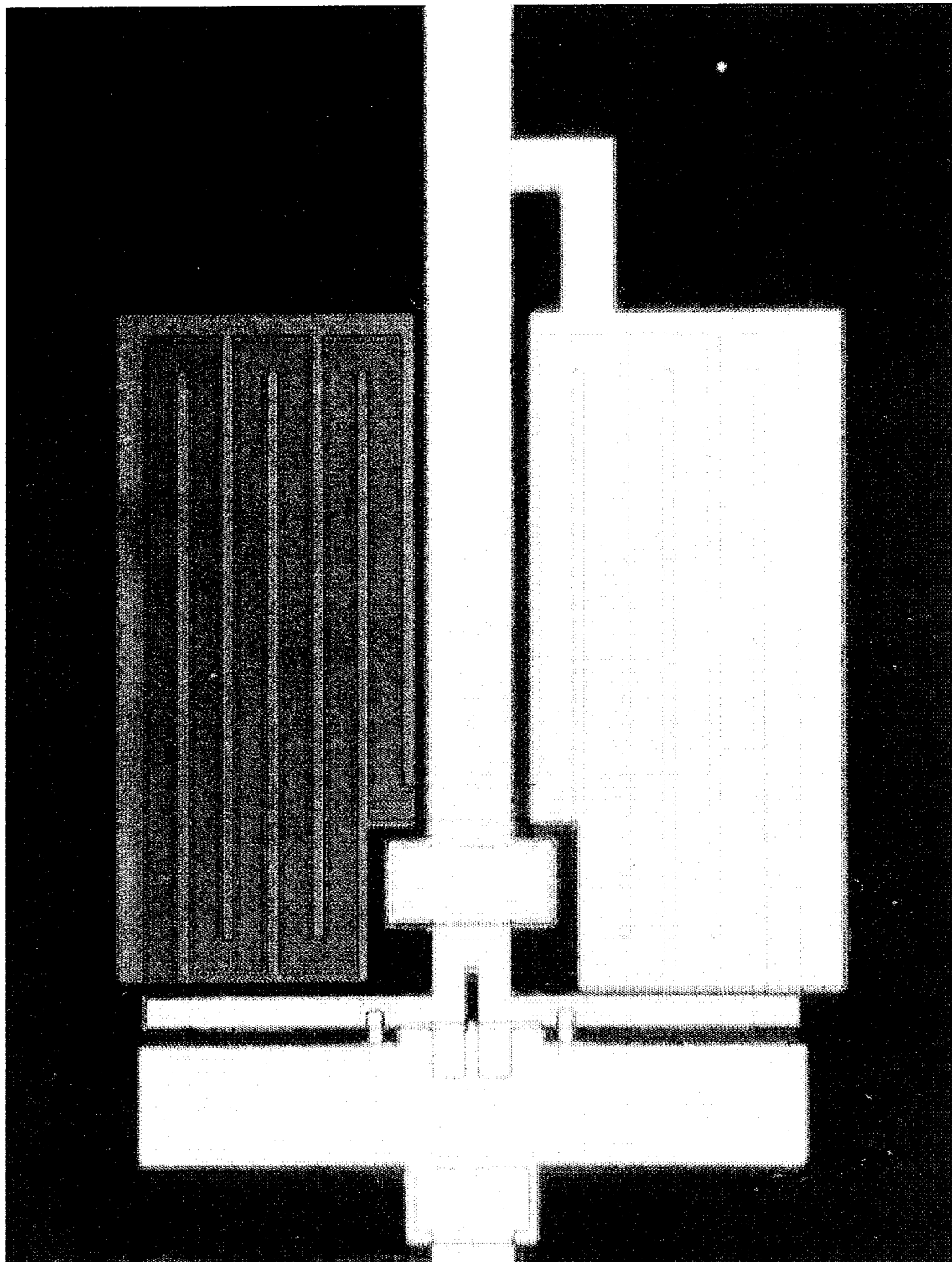


Figure 3.10. A photograph of the LWIR QSKIP designed and fabricated in this program. The photodetector is made of symmetric YBCO serpentine left and right portions with a niobium SQUID readout located at the bottom.

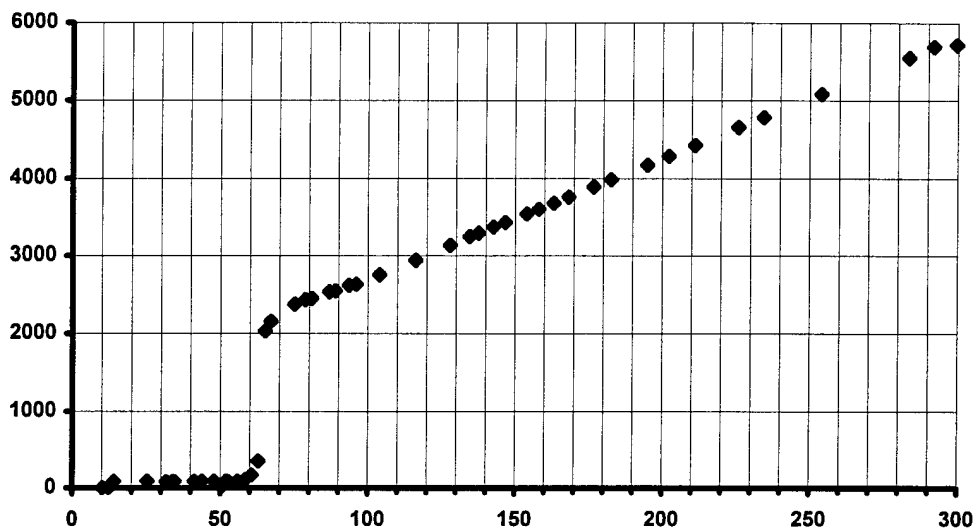


Figure 3.11. Resistance of YBCO photodetector versus temperature after all processing was completed. There is a small resistance offset which has shifted the R vs. T curve upward. Processing of the YBCO films caused the superconducting transition temperature to decrease from about 90K to about 60K.

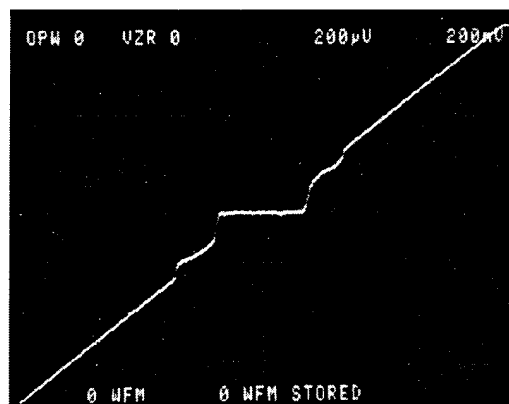


Figure 3.12. The I-V curve of a niobium SQUID built into the LWIR-QSKIP device, measured at 4.2K. The Y-axis is 200 μ V/div and the X-axis is 200 μ A/div.

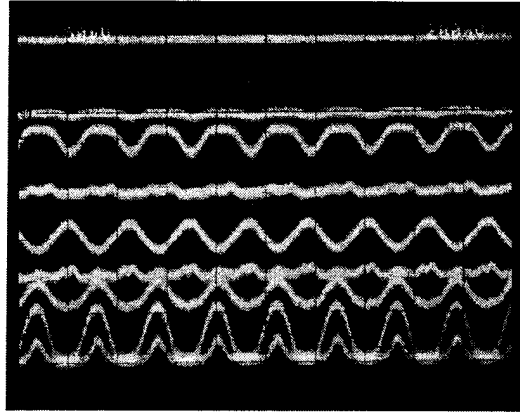


Figure 3.13. The SQUID $V-\Phi$ modulation curves, with magnetic flux provided by an injected control current. The Y scale is $50\mu\text{V}/\text{div}$ and the X-scale is $200\mu\text{A}/\text{div}$. The measured period corresponds to a loop inductance of 10pH , which was the design value.

Superconducting quantum detectors

Nathan Bluzer

Westinghouse Advanced Technology
Laboratories
Winterson and Nursery Roads, MS 3D12
Linthicum, Maryland 21090

Martin G. Forrester

Westinghouse Science and Technology
Center
1310 Beulah Road, Code S52
Pittsburgh, Pennsylvania 15235-5098

Abstract. The discovery of high-temperature superconductors (HTS) spawned many potential applications, including optical detectors. Realizing viable superconducting detectors requires achieving performance superior to competing and more mature semiconductor detector technologies, and quantum detector technologies in particular. We review why quantum detectors are inherently more sensitive than thermal or bolometric detectors. This sensitivity advantage suggests that for operation at cryogenic temperatures, we should be developing only quantum superconducting detectors. Accordingly, we introduce and describe the structure and the operation of a superconducting quantum detector with a superconducting quantum interference device (SQUID) readout circuit. The superconducting quantum detector, consisting of a superconducting loop, produces a photosignal in response to photoinduced changes in the superconducting condensate's kinetic inductance. The superconducting quantum detector is designed to operate only in the superconducting state and not in the resistive or transition states.

Subject terms: infrared technology; superconducting sensors; bolometric detectors; quantum detectors.

Optical Engineering 33(3), 697-703 (March 1994).

1 Introduction

The discovery of high-temperature superconductivity (HTS) by Bednorz and Muller¹ in 1986 evoked much excitement and a rush to find applications for the new discovery. One of the first proposed applications was for making optical detectors, and infrared detectors in particular. This proposed application was natural because infrared detectors operate at liquid nitrogen temperatures, just like high-temperature superconductors. Enomoto and Murakami² made the earliest photoresponse measurements using granular $\text{BaPb}_{0.7}\text{Bi}_{0.3}\text{O}_3$ and reported encouraging results. Soon, many more papers³⁻⁵ were published reporting on the photoresponse of different detector structures made in HTS materials. However, the photoresponse mechanism was not clearly identified nor was the ultimate expected detector performance. After much examination, it was shown⁶ that the reported photoresponse signals were consistent with a bolometric response. This was a very discouraging turn of events because the sensitivity of bolometric detectors is far less than the sensitivity of quantum detectors.

However, because of inherent limitations in semiconductor-based quantum detectors, the search for a superior superconductor-based quantum detector persists. Specifically, the main improvements over semiconductor-based detectors sought are a broadband photoresponse and operation at very

high speeds. Typically, semiconductors consume more power at higher operating speed, thus the desire to include high-speed signal processors with the detectors is incompatible with cooling constraints. Furthermore, broadband sensing, at very long infrared wavelengths, with semiconducting quantum detectors demands much lower operating temperatures than 77 K. HTS offers two attractive potentials: first, superconducting electronics is the only technology offering high-speed performance at low power, and second, the small energy gap in HTS materials offers the possibility of broadband photodetection. For these reasons the development of HTS broadband superconducting detectors is being actively pursued.

In this paper, we report on the progress attained toward realizing HTS superconducting quantum detectors. We begin by reviewing the inherent sensitivity advantage of quantum detectors over bolometric detectors in Sec. 1.1. This is followed by a description of the limitations of the conventional superconducting detectors, given in Sec. 1.2. Finally, Sec. 2 describes our novel approach to realizing a superconducting quantum detector.

1.1 Sensitivity of Bolometers and Quantum Detectors

Bolometers operate as thermal equilibrium devices, whereas quantum detectors operate as nonequilibrium devices. The performance of each detector category is ultimately limited by the detector's noise level. Photon shot noise is the ultimate sensitivity limit of an ideal detector. For very low photon flux levels, the detector's noise level sets the sensitivity limit. Here we review the operation of each detector category and provide expressions for the sensitivity limit of each. It be-

Paper IRT-37 received July 24, 1993; revised manuscript received Sep. 2, 1993; accepted for publication Sep. 12, 1993. This paper is a revision of a paper presented at the SPIE conference on Infrared Technology XIX, July 1993, San Diego, Calif. The paper presented there appears (unrefereed) in SPIE Proceedings Vol. 2020.
© 1994 Society of Photo-Optical Instrumentation Engineers. 0091-3286/94/\$6.00.

comes evident that quantum detectors are more sensitive than bolometric detectors.

In bolometers, photosignals are produced when the photoabsorbed photons' energy is quickly transferred into thermalized phonons, thereby changing the lattice's temperature. The transfer process of the photons' energy into the lattice is very fast relative to the bolometric detector's response time. Although photoabsorption in a bolometer occurs via intermediate quantum excitations of electrons or phonons, the lifetime of these intermediate excitations is very short and the excitation energy is quickly thermalized to produce a change in the lattice's temperature. Thus, the signal levels in a bolometric detector correspond to the change in the value of the lattice's temperature T . Similarly, the sensitivity^{7,8} of a bolometer is limited by the thermal fluctuations in the lattice's temperature ΔT^2 . For an object with heat capacity C connected to its surroundings by a thermal conductance G , the object's temperature change ΔT is related to its power exchange $W(t)$ with the surroundings by

$$C \frac{d\Delta T}{dt} + G\Delta T = W(t) \quad (1)$$

Using this expression and integrating over all frequencies,⁷ the mean-square value of the power flow from the body ΔW_T^2 can be expressed as

$$\Delta W_T^2 = 4k_B T^2 G \Delta f, \quad (2)$$

where Δf is the frequency band of interest. The smallest value for the object's power fluctuations with its surroundings occurs for the smallest value of conductance G , or the conductance of free space $4T^3\sigma A_D$, where σ is the Stefan-Boltzmann constant and A_D is the surface area of the object. Incorporating both equations, the mean-square value^{6,7} of the power flow from the body into free space is

$$\Delta W_T^2 = 16A_D k_B \sigma T^5 \Delta f. \quad (3)$$

The resolution or sensitivity of a bolometric detector is limited to the value of the power fluctuations with the surroundings, and this limit cannot be reduced by readout circuits.

In quantum detectors, photoabsorption efficiently channels the photons' energy directly into the production of quantum excitations, which may have relatively long lifetimes, creating a nonequilibrium. The nonequilibrium consists of an excess population of excited states over the thermal equilibrium population. The signal and the noise in quantum detectors correspond to the excess nonequilibrium population and the fluctuations therein, respectively. Thus for a given lattice temperature, different nonequilibrium levels exist, unlike in bolometric detectors. The sensitivity of a quantum detector is limited by the larger of (1) the minimum electronic noise in the detector ΔW_{QE} or (2) the photon radiation shot noise ΔW_{QP} . These noise quantities (ΔW_{QE} , ΔW_{QP}) are expressed as an average power fluctuation in the quantum detector^{6,7} as

$$\Delta W_{QE} = 4k_B T \Delta f, \quad (4a)$$

$$\Delta W_{QP} = \left[\Delta f A_D \left(\frac{hc}{\lambda_c} \right)^2 \int_0^{\lambda_c} \frac{2\pi c \lambda^{-4} d\lambda}{\exp(hc/\lambda k_B T) - 1} \right]^{1/2}, \quad (4b)$$

where c is the speed of light, λ is the wavelength, λ_c is the cutoff response of the detector, and h is Planck's constant. It should be evident from the integral in Eq. (4b) that the photon radiation shot noise in the quantum detector is band limited by the cutoff wavelength λ_c . In bolometric detectors, there is no spectral band limiting and hence the photon noise is significantly higher. Evaluating at 77 K, the noise power expressions for bolometric and quantum detectors (operating at a 30-Hz frame rate), we find that the noise power $(\Delta W_T^2)^{1/2}$ in a bolometric detector is significantly higher than the noise power in a quantum detector, each detector being 10^{-4} cm^2 in area. The bolometer's noise power $(\Delta W_T^2)^{1/2}$ is calculated to be 10^{-13} W , for a scene and a detector operating temperature of 77 K. The Johnson noise power (ΔW_{QE}) for a quantum 10^{-4} cm^2 detector operating at 77 K is $1.4 \times 10^{-19} \text{ W}$. Additionally, the radiation shot noise for 3 to 5 μm (8 to 12 μm) operation is 10^{-19} W (10^{-15} W). Combining the radiation shot noise with the detector's Johnson noise in quadrature, it becomes evident that the noise in quantum detectors is much less than the noise in bolometric detectors. These calculations clearly illustrate that at liquid nitrogen temperatures, quantum detectors are inherently more sensitive than thermal detectors. This preference for bolometric versus quantum detectors is independent of the specific detector signal generation mechanism, e.g., polarizability, resistivity, reflectivity, etc. Note that in addition to minimizing the noise levels in a detector, the signal levels need to be maximized to facilitate the performance of the readout circuits. The photosignal levels in bolometric detectors are maximized with minimum values for C and G , which ultimately puts severe restrictions of the operating frame rate of bolometric detectors. In quantum detectors, the photosignal levels are maximized with maximum values for the excitation lifetimes and much higher operating frame rates are possible.

1.2 Conventional Superconducting Detectors

Like semiconductors, superconducting detectors can be grouped into two main categories: quantum and bolometric (or thermal) detectors. Several different detectors have been realized in low- and high-temperature superconductors and they can be classified into the categories mentioned. Other exotic mechanisms of detection, such as photon-induced vortex-antivortex nucleation and photon-enhanced flux-flow, have been proposed⁹ but are not well understood vis-à-vis the four detector categories enumerated below.

1. Thermal detectors, where the energy from incident photons changes some temperature-dependent property of the material, such as resistance. Transition edge bolometers have been realized in low-temperature superconductor (LTS) and HTS materials, and their sensitivity is limited by the thermal energy fluctuations of the lattice and the photon flux. These detectors provide attractive performance especially for long-wave ($>20 \mu\text{m}$) detection where semiconductors require liquid helium operating temperatures.
2. Josephson-effect-based detectors, which make use of the nonlinear interaction between the incident photon's electromagnetic field and the high-frequency oscillating currents and voltages in a biased Josephson junction to perform millimeter-wave mixing and direct detec-

tion. These devices are particularly useful for millimeter- and submillimeter-wave detection.

3. Quasiparticle tunneling devices, such as superconductor-insulator-superconductor (S-I-S) mixers and direct detectors, where the incident photons are absorbed by quasiparticles, allowing tunneling events that would otherwise be energy forbidden to affect the junctions current-voltage (I-V) characteristics.
4. Pair-breaking detectors, where incident photons with energy larger than the energy gap break Cooper pairs, leading to changes in such macroscopic parameters as the superconducting gap and the kinetic inductance. Because of the difficulty of making S-I-S structures in HTS, this fourth detector category has received the most attention and is described in the following.

The fourth category is the least developed from a historical and practical standpoint. It can provide thermal as well as quantum detectors critically depending on the material parameters such as quasiparticle recombination time, which is not relevant to the other categories described. In HTS materials, the quasiparticle lifetime and the theory for predicting it are unknown. What is accepted is the existence of Cooper pairs in HTS with a minimum energy 2Δ required to break them. Thus, a basic mechanism of a superconducting quantum detector is to have photons with energy greater than 2Δ to break Cooper pairs and create excess quasiparticles.

To efficiently detect the excess quasiparticle population produced by photon depairing one must measure a property that is sensitive to all such quasiparticles. These include the voltage across a series of superconductive weak links, the microwave surface resistance of the superconductor, and the kinetic inductance of the superconductor.

Approaches pursued previously included the measurement, in granular HTS films, of the voltage signal induced by laser radiation, caused by local suppression of the gap, and thus the intergranular critical current in the film. However, in such a situation, only those quasiparticles created within a distance of order of the coherence length from a grain boundary are effective in reducing the intergranular critical current, and thus producing a voltage signal. The area efficiency of such a detector goes (in two dimensions) as the ratio of the coherence length to the grain size squared $(\xi/L_g)^2$, which for a typical granular YBCO film might be of order 10^{-7} . This is an unacceptably poor area efficiency (equivalent to a very poor effective quantum efficiency) and it is incompatible with a high-performance detector.

Using microwave circuits we can measure changes in the microwave reflectivity¹⁰ and resonator Q produced with photoabsorption. These detector approaches are sensitive to the entire quasiparticle or superconducting condensate population. Such techniques are not practical for detector array development because the size of the microwave readout circuits is incompatible with the small size of detectors, about $50 \times 50 \mu\text{m}^2$.

Another method sensitive to the entire quasiparticle or condensate population monitors the kinetic inductance of a superconducting film incorporated into a superconducting quantum interference device (SQUID) loop. The period of the threshold characteristic of gate current I_g versus control current I_c is given by Φ_0/L , where Φ_0 is the flux quantum

and L is the sum of the geometrical and kinetic inductances of the SQUID loop.¹¹ Thus, biasing at fixed values of I_c and I_g in the voltage state, the voltage will be a sensitive function of the kinetic inductance, and thus of the excess quasiparticle population. The disadvantage of such a scheme is that the SQUID must operate in the voltage state, and a calculation of the sensitivity of such a detector based on the measured noise characteristics of even the best dc SQUIDs yields extremely poor detectivity.

A more practical technique, and one that is also sensitive to all the quasiparticle's produced, is to measure the kinetic inductance \mathcal{L} of the condensate in the superconductor under irradiation. The kinetic inductance is a measure of the inertia of the Cooper pairs in a superconductor and is proportional to the reciprocal of the Cooper pair density n (see Sec. 2). With this approach, the detector is maintained in the superconducting current state (low noise) and changes in its kinetic inductance are monitored as a change in the magnetic field, as detailed in Sec. 2.

2 Quantum Superconducting Kinetic Inductance Detectors

The description of the quantum superconducting kinetic inductance detector (QSKID) illustrated in Fig. 1 is given in this section. We include the basis for the approach selected, the QSKID structure, the operating principle, and projected performance. Finally, we present an integrated QSKID with a SQUID readout circuit.

2.1 Detector Approach

Realizing a viable QSKID requires meeting several important technical objectives. First and foremost, the detector operation and structure needs to demonstrate a quantum response. The quantum response needs to occur with low electrical noise realizable in a zero-resistance superconducting state. Maximum photoresponse is desirable and is obtainable with a maximum quasiparticle lifetime. The readout circuit of the QSKID is to be simple, specifically a SQUID circuit. The

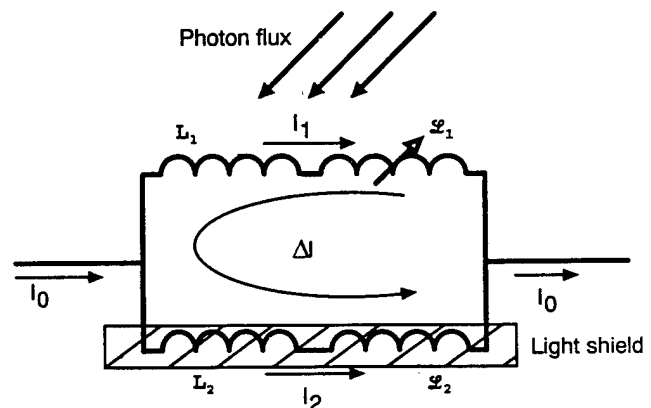


Fig. 1 QSKID structure, represented here by its equivalent circuit with magnetic L and kinetic \mathcal{L} inductances, consists of a superconducting loop biased with a dc current I_0 . The bias current splits between branch 1 and 2 of the superconducting loop producing branch currents I_1 and I_2 , respectively. For identical branches, i.e., with the same kinetic and magnetic inductance, current I_1 is equal to current I_2 . Changing the kinetic inductance by photodepairing in only one branch gives rise to a circulating photocurrent ΔI , producing a detectable magnetic field.

QSKID structure compatible with the aforementioned objectives includes

1. no Josephson junctions or weak links in the detector structure, thus facilitating manufacturability
2. maximum photoresponse amplitude
3. noise-equivalent power (NEP) superior to thermal detectors facilitated by operation in the zero-resistance superconducting state
4. broadband response, UV to far infrared ($\lambda_C > 20 \mu\text{m}$)
5. detector structure compatible with a 100% fill factor.

From a manufacturability point of view it is undesirable to use Josephson junctions or weak-link-based detectors. First, the coherence length in high T_C materials is too short for making Josephson junctions, and making reliable weak links in high T_C materials is very difficult. Second, the required weak-link area for each detector makes a large focal plane impractical. In high T_C , the coherence length ξ is very small ($< 2 \text{ nm}$) and for a photon to be detected it needs to be absorbed within a coherence length of the junction. Because a typical detector is about $50 \times 50 \mu\text{m}$ in area, many weak links would be needed to provide a 100% fill factor. The weak links would have to be separated by about 2 nm and span the detector width. An alternative is a vertical geometry where a single weak link per detector is used and it is oriented perpendicular to the incident photons. Neither geometries are technologically practical if we recognize that a typical focal plane is expected to have thousands of detectors. The total cross-sectional area of the weak links would grow to greater than $1 \times 1 \text{ cm}^2$. Such a detector array would need to satisfy demanding critical current uniformity requirements. Junctions with a nonuniform critical current density distribution would have significant fractions of areas with zero current flow, because of the small Josephson penetration depth, resulting in insensitive regions.

The second issue deals with maximizing the photoresponse amplitude. It has been mentioned earlier that the QSKID's responsivity is directly proportional to the lifetime of the quasiparticle excitations. The quasiparticle lifetime is minimized as the temperature increases toward T_C , thereby reducing the photoresponsivity. Quasiparticle lifetime reduction occurs because as the temperature increases, so does the number of quasiparticles and therefore the likelihood of finding two with opposite momentum to recombine into a Cooper pair. Making use of phonon-trapping phenomena and operating well below T_C , the quasiparticle lifetime and thus the photoresponse amplitude are maximized.

The third objective is the use of a detector structure not operating in the voltage state. Satisfying this criterion is important to achieve low operating power and minimum noise operation. If we operate high T_C detectors in a voltage state (with a gap voltage of about 20 mV) and at a bias current of 10 mA, the power consumed by each detector is about 0.2 mW. With thousands of detectors, this becomes a significant and an intolerable load on the refrigerator. Furthermore, given the low resistance of superconductors operating in a voltage state, the current shot noise would be too large, leading to poor sensitivity. Using voltage readout circuits, to take advantage of the small voltage noise, is unacceptable because of refrigeration requirements. Very low noise voltage sem-

iconducting readout circuits consume too much power to be compatible with large, low-power focal plane arrays. Thus if low power and low noise operation are sought the detector needs to remain in the zero-resistance superconducting state.

The fourth and fifth objectives are important from an operational point of view. HTS materials have a small energy gap and therefore are expected to respond from x rays to far infrared ($\lambda_C > 20 \mu\text{m}$). The need for a high fill factor detector structure is to simply maximize the detector quantum efficiency and performance.

A QSKID structure has been formulated¹² to satisfy the objectives raised in this section. The detector structure is illustrated in Fig. 1, where a single square superconducting loop forms the detector. No weak links are used, and the detector is made simply of a thin film patterned into a square loop. The output signal is a magnetic flux produced by the circulating current in the square loop. Details on the operation of this QSKID are given next.

2.2 QSKID Structure and Operation

In this section, the operation of the QSKID is described and the responsivity is computed. First, the operating constraints are computed. Next, a photon flux is used to cause a perturbation to the quiescent operating condition from which the responsivity is computed.

The current division between the QSKID's two branches is adjusted to minimize the total energy of the detector. The total energy (E) of the QSKID is made up of the magnetic field contribution (E_M) and the kinetic energy (E_K) of the supercurrent. For the QSKID structure in Fig. 1, the input current I_0 (less than the critical current) is divided between the two branches yielding currents I_1 and I_2 . The total magnetic field energy E_M stored in the magnetic inductances L_1 and L_2 , of branches 1 and 2, respectively, is

$$E_M = \frac{1}{2} L_1 I_1^2 + \frac{1}{2} L_2 I_2^2. \quad (5)$$

The kinetic energy E_K of the supercurrent I_0 flowing in branches 1 and 2, expressed in terms of the Cooper pair volume density n , the Cooper pair velocity v , the Cooper pair mass $2m$, the pair's electronic charge $2e$, the length of each branch ℓ , and the cross section of each branch A is

$$E_K = (n_1 A_1 \ell_1) m v_1^2 + (n_2 A_2 \ell_2) m v_2^2. \quad (6)$$

Recognizing that $I_1 = 2n_1 A_1 e v_1$ and $I_2 = 2n_2 A_2 e v_2$, we can recast Eq. (6) to obtain an expression for E_K in terms of I_1 and I_2 as

$$E_K = \frac{1}{2} \mathcal{L}_1 I_1^2 + \frac{1}{2} \mathcal{L}_2 I_2^2. \quad (7)$$

The recasting of Eq. (6) in terms of supercurrents I_1 and I_2 instead of v_1 and v_2 results in a form similar to Eq. (5) for the magnetic energy E_M . The two coefficients \mathcal{L}_1 and \mathcal{L}_2 provide a convenient form for expressing the kinetic energy of the supercurrent in terms of currents I_1 and I_2 . Because the forms of Eqs. (5) and (7) are similar, the coefficients \mathcal{L}_1 and \mathcal{L}_2 are labeled as kinetic inductances in correspondence to the magnetic inductance label given to L_1 and L_2 in Eq. (5). Equations for the kinetic inductances, associated with

the kinetic energy of the supercurrent flow in a rectilinear geometry QSKID, are defined as

$$\mathcal{L} = \left(\frac{\ell}{A} \right) \frac{m}{2e^2 n} . \quad (8)$$

The kinetic inductance is a function of the detector's geometry and is inversely proportional to the Cooper pair density n . Combining Eqs. (5) and (7), the QSKID's total energy E becomes

$$E = \frac{1}{2}(L_1 + \mathcal{L}_1)I_1^2 + \frac{1}{2}(L_2 + \mathcal{L}_2)I_2^2 . \quad (9)$$

Division of current $I_0 = I_1 + I_2$ between branches 1 and 2 (in Fig. 1) into I_1 and I_2 is according to the minimum energy constraint, or

$$\frac{\partial E}{\partial I_1} = \frac{\partial E}{\partial I_2} = (L_1 + \mathcal{L}_1)I_1 - (L_2 + \mathcal{L}_2)I_2 = 0 . \quad (10)$$

The QSKID's minimum energy criterion and its quiescent operating condition require the current division between the two branches to satisfy

$$(L_1 + \mathcal{L}_1)I_1 = (L_2 + \mathcal{L}_2)I_2 . \quad (11)$$

A photoresponse occurs in the QSKID when one branch, branch 1, for example, is exposed to a photon irradiance E_P sufficiently energetic to break Cooper pairs. As Cooper pairs are broken, the kinetic inductance \mathcal{L}_1 will increase [see Eq. (8)]. A change in the kinetic inductance of $\delta\mathcal{L}_1$ in branch 1 changes by ΔI_1 the current flowing in branch 1, or equivalently, produces a circulating current ΔI_1 in the QSKID loop. Taking the differential of Eq. (11), an expression for the photoresponse current is obtained. The induced current ΔI_1 is expressed in terms of the changes in the kinetic inductance $\delta\mathcal{L}_1$ of branch 1 as

$$\Delta I_1 = -I_1 \frac{\delta\mathcal{L}_1}{(L_1 + \mathcal{L}_1 + L_2 + \mathcal{L}_2)} . \quad (12)$$

Note that the photoresponse current ΔI_1 can also be computed from fluxoid conservation requirements, and the results are the same as given by Eq. (12), derived from minimum energy requirements. Specifically, in a superconductor the condensate described by a wave function that in general can be expressed by a complex quantity $\psi(x) = \sqrt{n(x)} e^{j\phi}$. At any given point x inside the superconductor the density of Cooper pairs is given by $n(x)$, where $n(x) = \psi^*(x)\psi(x)$. Writing out explicitly the current density in a superconductor using the canonical momentum, we obtain

$$\nabla\phi = \frac{2\pi}{\Phi_0} \left(\mathbf{A} + \frac{m}{2e^2 n} \mathbf{J}_s \right) , \quad (13)$$

where $\Phi_0 = h/2e$, \mathbf{A} is the vector potential, and \mathbf{J}_s is the supercurrent density. The closed loop of the detector is made from a superconducting film thinner than the magnetic penetration depth. Thus the supercurrent \mathbf{J}_s does not vanish anywhere inside the QSKID loop, Γ , and the \mathbf{J}_s term in Eq. (13)

cannot be made equal to zero. Because the superconductor's wave function $\psi(x)$ is single valued, a superconducting current flowing in a closed loop Γ (see Fig. 1) has a phase ϕ that can only change by $2\pi N$, where N is an integer. Performing the closed loop line integration on Eq. (13), we obtain

$$\oint_{\Gamma} \mathbf{B} \cdot d\mathbf{S} + \oint_{\Gamma} \frac{m}{2e^2 n} \mathbf{J}_s \cdot d\boldsymbol{\ell} = N\Phi_0 , \quad (14)$$

where \mathbf{B} is the magnetic field inside the detector's square loop and \mathbf{S} is the area enclosed by the curve Γ . Completing the integration in Eq. (14) and making use of Eq. (8), we obtain the expression

$$L_1 I_1 - L_2 I_2 + \mathcal{L}_1 I_1 - \mathcal{L}_2 I_2 = N\Phi_0 . \quad (15)$$

Taking the differential I_1 in Eq. (15) relative to the changes in the kinetic inductance $\delta\mathcal{L}_1$ produces the same result as given by Eq. (12), derived from minimum energy requirements. The magnetic field $\mathbf{B}_{\text{QSKID}}$ produced by the circulating current ΔI is a measure of the absorbed photon irradiance E_P .

2.3 QSKID Responsivity

The QSKID's responsivity \mathfrak{R} in webers per watt is expressed in terms of the incident photon irradiance E_P . The change in the kinetic inductance $\delta\mathcal{L}_1$ caused by this irradiance is

$$\delta\mathcal{L}_1 = \left(\frac{\partial\mathcal{L}_1}{\partial n_1} \right) \left(\frac{\partial n_1}{\partial E_P} \right) E_P = -\frac{\mathcal{L}_1}{n_1} \left(\frac{\eta\tau_{\text{eff}}}{d} \right) E_P , \quad (16)$$

where n_1 , η , τ_{eff} , and d are, respectively, the Cooper pair density, the number of Cooper pairs broken by each photon, the effective quasiparticle lifetime, and the detector thickness. The optical power P incident on the detector with an optical area A_D is simply the product of three terms:

$$P = A_D E_P h\nu . \quad (17)$$

The QSKID's responsivity \mathfrak{R} in webers per watt is computed by combining Eqs. (12), (16), and (17) to yield

$$\begin{aligned} \mathfrak{R}(\text{webers/watt}) &= (L_1 + L_2) \frac{\partial I_1}{\partial P} = \\ &= I_1 \left(\frac{L_1 + L_2}{L_1 + \mathcal{L}_1 + L_2 + \mathcal{L}_2} \right) \\ &\times \left(\frac{\eta}{A_D n_1 d} \right) \left(\frac{\mathcal{L}_1 \tau_{\text{eff}}}{h\nu} \right) . \end{aligned} \quad (18)$$

The responsivity is expressed as a product of four factors. The first factor is simply the bias current I_1 flowing through the branch illuminated by the photon irradiance. This is exactly given by Eq. (11), and for a balanced detector it is equal to $I_0/2$. The second factor in Eq. (18) is that the ratio of inductances is equal to about unity, because the kinetic inductances are smaller in value than the magnetic inductances. The third factor in Eq. (18) is a ratio of the number of Cooper pairs broken by a photon divided by the total number of Cooper pairs in the detector. For a 0.1-eV phonon and a YBCO QSKID $50 \times 50 \mu\text{m}$ in area 50 nm thick with a Cooper

pair density of $7 \times 10^{20} \text{ cm}^{-3}$, this term can be estimated equal to 10^{11} . Combining all these approximations, the expression for the responsivity reduces to

$$\mathfrak{R}(\text{webers/watt}) \cong 0.5 \times 10^{11} I_0 \tau_{\text{eff}} \mathcal{L}_1. \quad (19)$$

It is evident that the responsivity is directly proportional to the QSKID bias current I_0 , the effective quasiparticle lifetime τ_{eff} , and the kinetic inductance \mathcal{L}_1 . Substituting reasonable values for $I_0 \approx 1 \text{ A}$ and $\mathcal{L}_1 \approx 2 \text{ nH}$, the responsivity simplifies to $\mathfrak{R} \approx 700 \tau_{\text{eff}}$. Because I_0 is below the superconductors critical current, no power is dissipated by the QSKID. The estimated quasiparticle lifetime (see Sec. 2.4) is greater than $10 \text{ } \mu\text{s}$ at 10 K considering phonon trapping effects in the film. For these values, the responsivity conservatively computes to about 10^{-4} Wb/W at 10 K . This can readily be detected by a SQUID circuit.

2.4 Quasiparticle Lifetime

The photoresponse¹³ of YBCO and Nb were measured with the transient photoimpedance response (TPR) method¹⁴ to observe the nonequilibrium photoresponse¹⁵ of superconductors, and in particular to estimate the duration of the nonequilibrium excitation's lifetime. Laser pulses of 300 fs at 665 nm were used to study nonequilibrium excitation lifetimes from the photoinduced impedance transient that appears as a voltage signal across the films. From the amplitude and temporal dependence of the TPR signal, the thermalization process was studied in superconductors in the normal, transition, and superconducting states. The temporal dependence of the thermalization process forms the basis for our rough estimation of quasiparticle lifetime and the viability of the QSKID.

The TPR photoresponse clearly demonstrated that the duration of the photoinduced nonequilibrium was dominated by extrinsic quasiparticle lifetime effects. Specifically, phonon trapping in the thin-film samples significantly increased the quasiparticle recombination lifetime over intrinsic values. This was particularly evident from TRP measurement in the normal state where the signals were bolometric in origin and phonon trapping governed the photoresponse lifetime. Phonon trapping in thin films ($< 80 \text{ nm}$) resulted in thermalization lifetimes much greater than several nanoseconds. These lifetimes were longer than anticipated from a simple acoustic boundary mismatch model by at least an order of magnitude. A nonideal boundary between substrate and thin film and the slower velocity expected for energetic Debye phonons in YBCO help to explain the observed long thermalization lifetimes. It is important to stress that, in the superconducting state, the quasiparticle lifetime will be also governed by phonon trapping, and we infer from the data that their lifetime will be much larger than 10 ns . Clearly the net recombination of quasiparticles cannot occur faster than the escape time for phonons from the film into the substrate or the anharmonic phonon decay lifetime. The normal state measurements put a lower limit on the phonon escape time. However in the superconducting state the phonon trapping time is further lengthened by quasiparticle excitations.

In the superconducting state, the excess energy being thermalized is shuttled back and forth between creating phonons and exciting quasiparticles. This excess energy can be removed from the film only by phonon emission into the sub-

strate or anharmonic phonon decay. The energy stored in quasiparticles cannot be removed from the film via quasiparticle emission into the substrate because of their different band gap structures. Thus during the time the excess energy is stored in quasiparticle excitations no excess energy escapes into the substrate. At lower temperatures, typically the quasiparticle generation lifetime τ_B is much shorter than the quasiparticle recombination lifetime τ_R . Therefore, the excess energy is, most of the time, in the form of excited quasiparticles. Because the excess energy can escape into the substrate only through phonons, the storage of this excess energy in the form of quasiparticles effectively increases the phonon trapping time. According to Rothwarf and Taylor,¹⁶ the effective lifetime τ_{eff} for quasiparticle recombination can be related to the phonon trapping time (τ_γ) and the intrinsic quasiparticle generation and recombination lifetimes as

$$\tau_{\text{eff}} = \tau_R + \tau_\gamma \left(\frac{\tau_R}{\tau_B} \right). \quad (20)$$

Because $\tau_R > \tau_B$, the effective recombination time for quasiparticles should be longer than the thermalization time constant τ_γ for the normal state, see Eq. (20). From our measurement of the normal and superconducting state responses, it is evident that quasiparticle lifetimes much longer than 10 ns are likely. Calculations indicate that the quasiparticle lifetimes at 10 K may in fact be much greater than $10 \text{ } \mu\text{s}$.

2.5 QSKID Readout Circuit

The QSKID readout circuit senses the magnetic flux produced by the photoinduced current circulating in the square loop (see Fig. 2). For achieving the highest sensitivity, a SQUID is used to sense the photoinduced magnetic flux. In the detector currently under development, the SQUID is made up of two niobium tunnel junctions. The QSKID structure is equally compatible with a SQUID readout circuit made from YBCO weak links. For best sensitivity, the SQUID readout circuit should be well coupled to the flux produced by the QSKID, and this is achieved by integrating the QSKID and SQUID on a single substrate. The responsivity of the QSKID is about 10^{-4} Wb/W or about $0.5 \cdot 10^{11} \Phi_0/\text{W}$, a quantity readily detected by a SQUID.

3 Conclusions

For operation at cryogenic temperatures, excellent semiconductor quantum detectors are available. Intrinsically, quantum detectors are more sensitive than bolometers. Thus, if superconducting detectors are to displace existing semiconductor-based quantum detectors, they need to offer improved performance, possible only by developing QSKID and not superconducting bolometers. Such a superconducting quantum detector has been introduced and its operation described. The projected responsivity is calculated for a SQUID readout circuit. The QSKID is a broadband detector with a response extending beyond $\lambda \approx 20 \text{ } \mu\text{m}$ and consumes very little power. These performance features are not available with semiconducting detectors. Ongoing developments on the theoretical and experimental front should provide, in the near future, answers to the ultimate performance of the QSKID. The information presented represents a starting point in the development of a new superconducting detector structure.

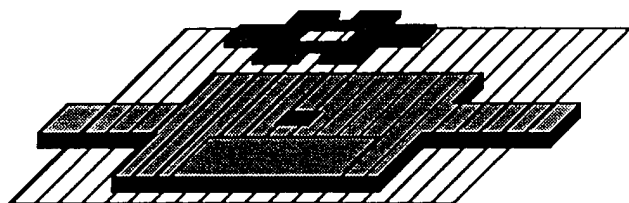


Fig. 2 QSKID with a SQUID readout circuit. The QSKID detector, represented by the bottom square loop, is overlaid by a light shield and an insulator. The topmost layer corresponds to the SQUID readout circuit, drawn enlarged. The actual size of the SQUID readout circuit is much smaller than the size of the QSKID detector.

Acknowledgments

This research and development has been supported by Westinghouse IR&D under task No. Z61601EHAA, the Naval Research Laboratory under contract No. N0014-92-C-2033, and the Ballistic Missile Defence Organization/Innovative Science & Technology Office under contract No. DASG60-92-0140.

References

1. J. G. Bednorz and K. A. Müller, "Possible high T_C superconductivity in the Ba-La-Cu-O system," *Z. Phys. B* **64**, 189-193 (1986); "Pseudogap-type oxides—The new approach to high- T_C superconductivity," *Rev. Mod. Phys.* **60**, 585-600 (1988).
2. Y. Enomoto and T. Murakami, "Optical detector using superconducting $\text{BaPb}_{0.7}\text{Bi}_{0.3}\text{O}_3$," *J. Appl. Phys.* **59**(11), 3807-3814 (1986).
3. H. S. Kwok, J. P. Zheng, and Q. Y. Ying, "Nonthermal optical response of Y-Ba-Cu-O thin films," *Appl. Phys. Lett.* **54**, 2473-2475 (1989).
4. M. Leung, P. R. Broussard, J. H. Claassen, M. Osofsky, S. A. Wolf, and U. Strum, "Optical detection in thin granular films of Y-Ba-Cu-O at temperatures between 4.2 and 100 K," *Appl. Phys. Lett.* **51**, 2046-2049 (1987).
5. W. S. Brocklesby, D. Monroe, A. F. J. Levi, M. Hong, S. H. Liou, J. Kwo, C. E. Rice, P. M. Mankiewicz, and R. E. Howard, "Electrical response of superconducting $\text{YBa}_2\text{Cu}_3\text{O}_{7-x}$ to light," *Appl. Phys. Lett.* **54**, 1175-1177 (1989).
6. M. G. Forrester, M. Gottlieb, J. R. Gavaler, and A. I. Braginski, "Optical response of epitaxial and granular films of $\text{YBa}_2\text{Cu}_3\text{O}_{7-x}$ at temperatures from 25 K to 100 K," *IEEE Trans. Magnet.* **25**, 1327-1330 (1989).
7. R. A. Smith, F. E. Jones, and R. P. Chasmar, *The Detection and Measurement of Infra-red Radiation*, p. 206, Clarendon Press, Oxford (1958).
8. P. W. Kruse, L. D. McGlauchlin, and R. B. McQuistan, *Elements of Infrared Technology: Generation, Transmission, and Detection*, p. 354 John Wiley & Sons, New York (1962).
9. A. M. Kadin, M. Leung, A. D. Smith, and J. M. Murduck, "Nonbolometric infrared detection in thin superconducting films via photo-production of fluxon pairs," *IEEE Trans. Magnet.* **27**, 1540-1543 (1991).
10. R. Kaplan, W. E. Carlos, and E. J. Cukauskas, "Microwave detected optical response of $\text{YBa}_2\text{Cu}_3\text{O}_{7-x}$ thin films," *J. Appl. Phys.* **67**(9), 4212-4216 (1990).

11. E. K. Track, M. Radparvar, and S. M. Faris, "Modulation of the penetration depth of Nb and NbN films by quasiparticle injection," *IEEE Trans. Magnet.* **25**, 1096-1099 (1989).
12. N. Bluzer, "Multispectral superconductive quantum detector," U.S. Patent No. 5,179,072 (Jan. 12, 1993) and "Multispectral superconductive quantum detector," U.S. Patent No. 5,185,527 (Feb. 9, 1993).
13. N. Bluzer, "Temporal relaxation of nonequilibrium in YBCO measured from transient photoimpedance response," *Phys. Rev. B* **44**, 10222-10232 (1991); "Temporal relaxation of photoinduced nonequilibrium in niobium," *Phys. Rev. B* **46**, 1033-1042 (1992).
14. N. Bluzer, "Temporal relaxation of photoinduced nonequilibrium in superconductors," *J. Appl. Phys.* **71**, 1336-1348 (1992).
15. N. Bluzer, "Biexponential decay and delay artifacts in the photoresponse of superconductors," *IEEE Trans. Appl. Supercond.* **3**(1), 2869-2872 (1993).
16. A. Rothwarf and B. N. Taylor, "Measurements of recombination lifetime in superconductors," *Phys. Rev. Lett.* **19**, 27-30 (1967); also see W. H. Parker, "Modified heating theory of nonequilibrium superconductors," *Phys. Rev. B* **12**, 3667-3672 (1975).



Nathan Bluzer is a senior advisory physicist at the Westinghouse Advanced Technology Laboratories, Linthicum, Maryland. He received his BS degree in electrical engineering with honors and a PhD degree in solid state physics from the University of Maryland, College Park. He was a visiting scholar at Stanford University studying high-temperature superconductivity. For more than 20 years Bluzer has had a key role in the research and development of high-speed CCDs, imaging CCDs, radiation hard CCDs, multiplexers, and detectors for IR sensors. The Maryland Academy of Sciences has recognized his original work and awarded him Maryland's 1990 Outstanding Young Engineer Award. Currently, he is responsible for the development of multispectral superconducting detectors. Bluzer has published more than 40 papers and has 30 U.S. patents granted and/or pending. He is a member of TB π , a fellow of the IEEE, and a life member of APS.



Martin G. Forrester received his BS in physics from the Massachusetts Institute of Technology in 1981 and his PhD in physics from Harvard University in 1987, completing his thesis on the properties of 2-D arrays of Josephson junctions. Since joining the staff of the Cryoelectronics Group at the Westinghouse Science and Technology Center in 1987, he has worked in the area of IR and digital electronic applications of superconductivity. His work has included the investigation of the response of high-temperature superconductors to visible and IR radiation, and in particular the understanding of the response in the context of thermal versus nonequilibrium models. He is currently pursuing the development of high-temperature superconducting Josephson junctions for both IR and digital circuit applications. Dr. Forrester has authored 30 papers on superconducting materials and devices. He is a member of the Materials Research Society and the American Physical Society.

Superconducting Quantum Detectors in YBCO

Nathan Bluzer¹ and Martin G. Forrester²

Received 31 July 1993

The discovery of high-temperature superconductors has led to great efforts to find potential applications, including the development of photon detectors. We review the limitations of the different approaches proposed for realizing superconducting photon detectors. The structure and operation of a new quantum superconducting kinetic inductance detector (QSKID) with a SQUID readout circuit is described. The QSKID is made from a superconducting loop where the photosignals are generated in response to photoinduced changes in the condensate's kinetic inductance. The QSKID operates in the zero-resistance superconducting state, thereby circumventing Johnson noise.

KEY WORDS: HTS; photodetector; quantum detector; kinetic inductance.

1. INTRODUCTION

The discovery of high-temperature superconductivity (HTS) by Bednorz and Muller [1] in 1986 evoked proposals for making IR photon detectors in HTS. These proposals were offered because IR detectors, like HTS, operate at liquid-nitrogen temperatures. Enomoto and Murakami [2] made photoresponse measurements on granular $\text{BaPb}_{0.7}\text{Bi}_{0.3}\text{O}_3$ and reported encouraging results. Soon, more papers [3–5] followed, reporting on the photoresponse of different HTS detector structures. After much analysis, it was recognized [6] that the reported photoresponse signals were consistent with a bolometric process. This was discouraging because the sensitivity [7,8] of bolometric detectors is less than the sensitivity of quantum detectors. However, because of technological limitations in semiconducting quantum detectors, the search for a superior superconducting quantum detector continues. In this paper, we report on the limitations of different published approaches toward realizing HTS superconducting detectors and an approach to realizing a HTS quantum detector.

2. CONVENTIONAL SUPERCONDUCTING DETECTORS

Semiconducting and superconducting detectors can be grouped into two main categories: quantum and bolometric (or thermal) detectors. The detectors realized in LTS and HTS materials can be classified into the aforementioned categories. Other exotic mechanisms of detection, such as photon-induced vortex-antivortex nucleation, and photon-enhanced flux flow, have been proposed [9] but are not well understood vis-a-vis the four conventional detector approaches enumerated below.

- I. Thermal detectors, where the photoabsorbed energy changes the lattice temperature and some electronic property of the material, such as resistance. LTS and HTS transition edge bolometers have a sensitivity limited by the energy fluctuations of the lattice temperature and the photon flux. These detectors are attractive for very long wavelength ($>20\ \mu\text{m}$) applications where semiconductor-based detectors require cooling to liquid-helium temperatures.
- II. Josephson-effect based detectors are particularly useful for millimeter and submillimeter wave detection. These devices use the nonlinear interaction between the incident

¹Westinghouse Advanced Technology Laboratories, Winterson and Nursery Roads, Linthicum, Maryland 21090.

²Westinghouse Science and Technology Center, 1310 Beulah Road, Pittsburgh, Pennsylvania 15235-5098.

photons and the high-frequency oscillating currents and voltage, in a biased Josephson junction, to perform millimeter wave mixing and direct detection.

- III. Quasiparticle tunneling devices such as S-I-S mixers and direct detectors, where the incident photons are absorbed by quasiparticles, allowing tunneling events which would otherwise be energy-forbidden to affect the junction I - V characteristics.
- IV. Pair-breaking detectors, where incident photons (with energy larger than the energy gap) break Cooper pairs, leading to changes in such macroscopic parameters as the superconducting gap and the kinetic inductance. In these detectors photoabsorption is by quantum excitations.

The basic requirement for a superconducting quantum detector are: (1) quantum excitations to create excess quasiparticles by breaking Cooper pairs with photons that have an energy greater than 2Δ , and (2) efficient detection of the excess quasiparticles by measuring a property sensitive to the condensate population. Properties sensitive to the quasiparticle (or condensate) population include the voltage across a series of weak links, the superconductor's microwave surface resistance, or the superconductor's kinetic inductance.

In granular HTS films, the voltage signals are induced by laser radiation that locally suppresses the gap and the intergranular critical current. Only those quasiparticles created within a distance of the order of the coherence length ξ from the grain boundaries produce a voltage signal. The *area efficiency* of a granular HTS detector is expressed (in 2D) as the ratio of the coherence length to the average grain size, L_g , squared. For a typical granular YBCO film, this area efficiency ratio $(\xi/L_g)^2$ is of the order 10^{-7} . This is an extremely poor area efficiency and equivalent to a very poor quantum efficiency, incompatible with high-performance detectors.

The poor area efficiency in granular HTS detectors can be overcome with microwave readout circuits which are sensitive to the entire quasiparticle or condensate population, such as changes in the microwave reflectivity [10] and resonator Q produced with photoabsorption. The microwave readout circuit's size is much larger than a typical pixel size, about $50 \times 50 \mu\text{m}^2$. Thus, such a readout approach is not practical nor compatible with the development of dense two-dimensional arrays.

Another method sensitive to photoinduced changes in the condensate population is the voltage vs. flux signal of the superconducting film incorporated into a SQUID loop. Biasing this SQUID loop in the voltage state, photodepairing changes the condensate's kinetic inductance, resulting in a voltage signal, derived from the SQUID's periodicity with flux. The period of the SQUID's threshold characteristic with applied flux is given by Φ_0/L , where Φ_0 is the flux quantum and L is the total inductance, equal to the sum of the geometrical and kinetic inductances in the SQUID loop [11]. Such a detector must operate in the voltage state, and calculations reveal a sensitivity severely limited by the SQUID's noise characteristics, resulting in poor detectivity.

To realize sensitive (low-noise) detectors, it is critical that the LTS or HTS detectors operate in the current and not voltage state. This detector needs to be sensitive to photoinduced changes in the condensate, e.g., sensitive to the condensate's kinetic inductance \mathcal{L} . With such an approach, the detector remains in the superconducting current state (low noise), and changes in its kinetic inductance are monitored as a change in the magnetic field, as detailed in the next section.

3. QUANTUM SUPERCONDUCTING KINETIC INDUCTANCE DETECTORS

A viable QSKID needs to operate in the superconducting current state to achieve low-noise performance. For maximum photoresponse, long quasiparticle photoexcitation lifetimes are necessary. The QSKID's read-out circuit must be simple, specifically a SQUID circuit. The QSKID structure compatible with the aforementioned objectives includes: (a) no weak links, facilitating low noise and manufacturability, (b) maximum photoresponse and NEP by operation in the zero-resistance superconducting state, (c) multispectral response from UV to the far infrared ($\lambda_c > 20 \mu\text{m}$), and (d) structure compatible with a 100% fill factor. Meeting these objectives is necessary to produce a viable QSKID with a performance superior to competing semiconductor quantum detectors. Such a detector structure has been formulated [12] and is schematically illustrated in Fig. 1 by a single superconducting loop. No weak links are used, and the output signal is the magnetic flux produced by the circulating current in the loop. Details on the QSKID's operation are given next.

The division of current $I_0 < I_c$ into currents I_1 and I_2 satisfies an energy minimum [12,13] and the single-valuedness for the condensate wave function,

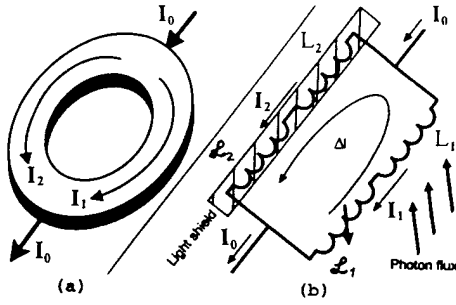


Fig. 1. The QSKID (a) and its equivalent circuit (b) consists of superconducting loop biased with a dc current I_0 , with magnetic (L) and kinetic (\mathcal{L}) inductances. Bias current I_0 splits between branches 1 (I_1) and 2 (I_2) of the superconducting loop. For identical branches $I_1 = I_2$. Photodepairing only in branch 1 changes the kinetic inductance ($\delta\mathcal{L}_1$) and gives rise to a circulating photocurrent ΔI , producing a detectable magnetic field. A small SQUID placed (not shown) over the opening in the QSKID detects the photoinduced magnetic flux.

expressed by a complex quantity $\psi(x) = \sqrt{n(x)} e^{i\varphi}$. We calculate the current division by requiring a single-valued $\psi(x)$, and the result is consistent with energy minimization requirements. At any point x inside the superconductor, the density of Cooper pairs is given by $n(x)$, where $n(x) = \psi^*(x)\psi(x)$. Writing out explicitly the condensate's phase gradient $\nabla\varphi$, we obtain

$$\nabla\varphi = \frac{2\pi}{\Phi_0} \left(\bar{A} + \frac{m}{2e^2 n} \bar{J}_s \right) \quad (1)$$

where, $\Phi_0 = h/2e$, \bar{A} is the vector potential, and \bar{J}_s is the supercurrent density. In superconducting films thinner than the London penetration depth, the supercurrent \bar{J}_s does not vanish anywhere inside the QSKID loop, and $\psi(x)$ is single-valued. The line integral in Eq. (1), after some simplifications, yields

$$\int_S \bar{B} \cdot d\bar{S} + \oint_{\Gamma} \frac{m}{2e^2 n} \bar{J}_s \cdot d\bar{l} = N\Phi_0 \quad (2)$$

where \bar{B} is the magnetic field inside the detector's loop and \bar{S} is the area enclosed by the integration curve. Completing the integration in Eq. (2), we obtain

$$L_1 I_1 - L_2 I_2 + \mathcal{L}_1 I_1 - \mathcal{L}_2 I_2 = N\Phi_0 \quad (3)$$

where the four coefficients $\mathcal{L}_1(L_1)$ and $\mathcal{L}_2(L_2)$ are the kinetic (magnetic) inductances of branch 1 and 2, respectively. The kinetic inductance of each branch expressed in terms of the Cooper pair's mass ($2m$), charge ($2e$), the branch length (l), with cross sectional

area (a) is

$$\mathcal{L} = \left(\frac{l}{a} \right) \frac{m}{2e^2 n} \quad (4)$$

In a QSKID with a symmetrical geometry shielded from external fields and not subjected to any illumination, the net enclosed flux is zero [the right side of Eq. (3) is zero] and no current circulates, $I_1 = I_2 = I_0/2$. Illuminating only branch number 1 in Fig. 1 changes $\delta\mathcal{L}_1$. The change in $\delta\mathcal{L}_1$ that will produce a circulating current ΔI , obtained by taking the differential of Eq. (3), is

$$\Delta I_1 = -I_1 \frac{\delta\mathcal{L}_1}{(L_1 + \mathcal{L}_1 + L_2 + \mathcal{L}_2)} \quad (5)$$

The circulating current ΔI produces a magnetic field \bar{B}_{QSKID} and flux $\Phi = \Delta I(L_1 + L_2)$, which is a measure of the absorbed photon flux Φ_{ph} . The QSKID's responsivity \mathfrak{R} (Webers/watt) (dependent on the flux Φ_{ph} , changes in \mathcal{L}_1 , and number of broken pairs n_1) is

$$\delta\mathcal{L}_1 = \left(\frac{\partial\mathcal{L}_1}{\partial n_1} \right) \left(\frac{\partial n_1}{\partial \phi_{\text{ph}}} \right) \Phi_{\text{ph}} = -\frac{\mathcal{L}_1}{n_1} \left(\frac{\eta \tau_{\text{eff}}}{d} \right) \Phi_{\text{ph}} \quad (6)$$

where n_1 , η , τ_{eff} , and d are, respectively, the Cooper pair density, the number of pairs broken by a photon, the effective quasiparticle lifetime, and the detector thickness. The incident power P on the detector, with an optical area A_λ , is

$$P = A_\lambda \Phi_{\text{ph}} h\nu \quad (7)$$

Combining Eqs. (5) and (6), multiplying by $(L_1 + L_2)$, and dividing by 7, the computed QSKID's responsivity \mathfrak{R} (Webers/watt) becomes

\mathfrak{R} (Webers/watt)

$$= I_1 \left(\frac{L_1 + L_2}{L_1 + \mathcal{L}_1 + L_2 + \mathcal{L}_2} \right) \left(\frac{\eta}{A_\lambda n_1 d} \right) \left(\frac{\mathcal{L}_1 \tau_{\text{eff}}}{h\nu} \right) \quad (8)$$

The first factor is the bias current I_1 flowing through the illuminated branch, and for a balanced detector it is equal to $I_0/2$. The second factor, the ratio of inductances, is equal to about unity, because $\mathcal{L}_1 \approx L_1$ and $\mathcal{L}_2 \approx L_2$. The third factor, for a 0.1-eV photon and a YBCO QSKID $50 \mu\text{m} \times 50 \mu\text{m}$ in area and 160 nm thick with a Cooper pair density of $\approx 10^{20} \text{ cm}^{-3}$, is estimated to be 2×10^{-11} . Combining all these, the expression for the responsivity reduces to

$$\mathfrak{R} \text{ (Webers/watt)} \cong 10^8 I_0 \tau_{\text{eff}} \mathcal{L}_1. \quad (9)$$

The responsivity is proportional to the QSKID bias current I_0 , the effective quasiparticle lifetime τ_{eff} , and the kinetic inductance \mathcal{L}_1 . Substituting values for $I_0 \approx 0.1$ A and $\mathcal{L}_1 \approx 2$ nH, the responsivity simplifies to $\mathfrak{R} \approx 0.02 \tau_{\text{eff}}$. Since I_0 is below the superconductor's critical current, no power is dissipated by the QSKID. The estimated quasiparticle lifetime [14,15] is about 10 msec at 10 K, considering phonon trapping effects in the film. For these values the responsivity conservatively computes to about 10^{-4} Webers/Watt at 10 K. This can readily be detected by a SQUID circuit with a sensitivity of $\approx 10^{-21}$ Webber/ $\sqrt{\text{Hz}}$.

The QSKID read-out circuit senses the magnetic flux produced by the photoinduced current circulating in the loop (see Fig. 1). A SQUID is used to sense the photoinduced magnetic flux. In the QSKID under development, the SQUID is made up of two niobium tunnel junctions or YBCO weak links. For best sensitivity, the SQUID read-out circuit should be well coupled to the flux produced by the QSKID, integrating the QSKID and SQUID on a single substrate. The responsivity of the QSKID is about 10^{-4} Webers/Watt or about $0.5 \times 10^{11} \Phi_0/\text{Watt}$, a quantity readily detected by a SQUID, yielding an $\text{NEP} \approx 10^{-17}$ Watt/ $\sqrt{\text{Hz}}$.

4. CONCLUSIONS

Excellent semiconductor quantum detectors are available for operation at cryogenic temperatures. Intrinsically, quantum detectors are more sensitive than bolometers. Thus, if superconducting detectors are to replace existing semiconducting quantum detectors, they need to offer improved performance, possible only by developing QSKID and not superconducting bolometers. A superconducting quantum detector, with a SQUID read-out circuit, is

introduced and its operation is described. The QSKID projected responsivity is calculated. The QSKID is a multispectral detector with a response extending beyond $\lambda \approx 20 \mu\text{m}$ and consumes very low power.

ACKNOWLEDGMENTS

This research was supported by Westinghouse IR&D under task Z61601EHAA, the Naval Research Laboratory under tasks No. N0014-92-C-2033, and the Ballistic Missile Defence Organization/Innovative Science & Technology Office under task No. DASG60-92-0140.

REFERENCES

1. J. G. Bednorz and K. A. Muller, *Z. Phys. B* **64**, 189 (1986); *Rev. Mod. Phys.* **60**, 585 (1988).
2. Y. Enomoto and T. Murakami, *J. Appl. Phys.* **59**, 3807 (1966).
3. H. S. Kwok, J. P. Zheng, and Q. Y. Ying, *Appl. Phys. Lett.* **54**, 2473 (1989).
4. M. Leung, P. R. Broussard, J. H. Claassen, M. Osofsky, S. A. Wolf, and U. Strum, *Appl. Phys. Lett.* **51**, 2046 (1987).
5. W. S. Brocklesby, D. Monroe, A. F. J. Levi, M. Hong, S. H. Liou, J. Kwo, C. E. Rice, P. M. Mankiewicz, and R. E. Howard, *Appl. Phys. Lett.* **54**, 1175 (1989).
6. M. G. Forrester, M. Gottlieb, J. R. Gavaler, and A. I. Braginski, *IEEE Trans. Magn.* **MAG-25**, 1327 (1989).
7. R. A. Smith, F. E. Jones, and R. P. Chasmar, *The Detection and Measurement of Infra-red Radiation* (Oxford University Press, New York, 1958), p. 206.
8. P. W. Kruse, L. D. McGlauchlin, and R. B. McQuistan, *Elements of Infrared Technology: Generation, Transmission, and Detection* (J. Wiley, New York, 1962), p. 354.
9. A. M. Kadin, M. Leung, A. D. Smith, and J. M. Murduck, *IEEE Trans. Magn.* **27**, 1540 (1991).
10. R. Kaplan, W. E. Carlos, and E. J. Cukauskas, *J. Appl. Phys.* **67**, 4212 (1990).
11. E. K. Track, M. Radparvar, and S. M. Faris, *IEEE Trans. Magn.* **MAG-25**, 1096 (1980).
12. N. Bluzer, United States Patents 5,179,072 and 5,185,527.
13. N. Bluzer and M. G. Forrester, Proceedings of the SPIE conference, San Diego, California, July 11-16, 1993.
14. N. Bluzer, *Phys. Rev. B* **44**, 10222 (1991); N. Bluzer, *Phys. Rev. B* **46**, 1033 (1992).
15. N. Bluzer, *J. Appl. Phys.* **71**, 1336 (1992); *IEEE Trans. Appl. Supercond.* **3**, 2869 (1993).

Quantum Detectors in Superconducting YBCO*

Nathan Bluzer

Westinghouse Advanced Technology Labs., Winterson & Nursery Rds., Linthicum, MD 21090 USA

Martin G. Forrester

Westinghouse Science and Technology Center, 1310 Beulah Rd., Pittsburgh, PA 15235 USA

Abstract---A superconducting quantum detector structure in YBCO is described with a directly coupled SQUID read out circuit. The detector geometry is optimized for maximum photoresponse with the use of a serpentine pattern. The serpentine pattern reduces quasiparticle diffusion effects and maximizes the photoinduced changes in the kinetic inductance. The operation of this sensor is analyzed in terms of geometry and quasiparticle lifetime to obtain expressions for the signal and noise of this detector. The background limited infrared performance of this detector is calculated to be about 5×10^{-17} NEP. The photoresponse is expected to be limited by the superconducting energy gap, about 30-40 μm .

I. INTRODUCTION

Since the discovery of High Temperature Superconductivity (HTS) by Bednorz and Muller [1] many proposals were offered for fabricating Infrared (IR) detectors in HTS. Enomoto and Murakami [2] measured the photoresponse in $\text{BaPb}_{0.7}\text{Bi}_{0.3}\text{O}_3$ and reported encouraging results. Many more photoresponse measurements were reported on HTS, however it was shown by Forrester et al. [3] that the results reported were consistent with a bolometric and not a quantum (or photon) detector response. This was disappointing for it has been long recognized that theoretically above 1K quantum detectors offer superior sensitivity over bolometric detectors [4]. Hence the expectation of replacing semiconductor based quantum detectors by bolometric superconductor based detectors was unreasonable. If superconducting detectors are to compete with semiconducting quantum detectors, superconducting detector structures are needed which provide photon noise limited performance.

At Westinghouse we have been pursuing, for several years, the development of superconducting quantum detectors. The superconducting quantum detectors are intended for imaging applications. In such applications the detector integration times are from several μsec to several msec long. And thus we alleviate the need for very fast readout circuits and very fast photoresponse

measurements to short laser pulses. The detectors are intended to operate in the superconducting current state (zero voltage) under static nonequilibrium conditions and in the Meissner state (below H_{C1}), to circumvent noise from fluxoid formations and movement. The detectors' performance is dependent on the quasiparticle lifetimes and these lifetimes are maximized as the detectors' operating temperature is lowered significantly below the superconducting transition temperature T_C . Additionally, the approach selected [5] does not use weak-links in the detector structure and thereby maximizes the quantum efficiency, and reduce the fabrication difficulties associated with making weak-links in YBCO. Weak-link based detectors are only sensitive to photoexcitations that occur within several coherence lengths ξ from the weak-link. Thus for good quantum efficiency, many weak-links need within each detector pixel because $\xi \approx 1.5 \text{ nm}$ is many times smaller than the typical detector pixel, 25-100 μm . The use of many weak-links for each detector imposes severe fabrication yield problems as well as sensitivity issues. Hence we have selected a simpler detector and readout approach for realizing superconducting quantum sensors.

II. SUPERCONDUCTING SENSOR

The superconducting quantum detector we are developing are based on the condensate's kinetic inductance and the changes in this kinetic inductance produced by photodepairing of Cooper pairs. Generically, the structure of Quantum Superconducting Kinetic Inductance Detector (QSKID) is shown in Fig. 1, where a thin (less than a London penetration depth) superconducting closed loop, operating in the current and Meissner states, divides a DC current $I_0 = I_L + I_R$ into a left branch current I_L and a right branch current I_R . The current division satisfies the Hamiltonian's minimum energy conditions [5][6] and is expressed by Equation 1 as:

$$L_L I_L = L_R I_R \quad (1)$$

Where the L_L and L_R are the total inductance terms for the left and right branches, respectively. The total inductance of a branch includes: the geometrical (or

* Manuscript received October 17, 1994. This work was supported by: the Naval Research Labs. under contract # N0014-92-C-2033, Innovative Science and Technology Office through the Army contract # DASG60-92-0140, and Westinghouse IR&D under task Z61601EHAA.

magnetic field) self inductance, the interbranch mutual inductance, and the kinetic inductance. For example, the total left branches inductance $L_L = L_{LG} - L_{LM} + L_{LK}$ includes the geometrical self inductance L_{LG} , the mutual inductance between the left and right branches (with negative coupling) L_{LM} , and the kinetic inductance L_{LK} .

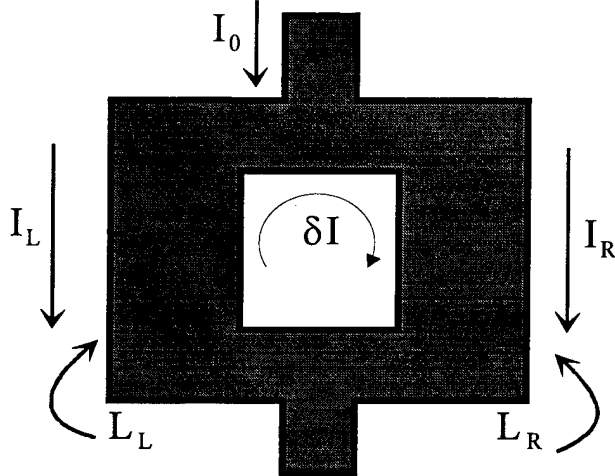


Figure 1. The generic diagram of a QSKID consisting of a superconducting loop dividing a DC current I_0 into I_L and I_R . Only one branch, the left, e.g., is exposed to a photon flux while the other is shielded. Changes in the kinetic inductance of the exposed branch causes a circulating current δI .

A photon flux Ψ on the left branch breaks up Cooper pairs and produces a decrease in the Cooper pair density ρ_L . The kinetic inductance $L_{LK} = [l_L m_{CP}] / [S_L q_{CP}^2 \rho_L]$ is inversely dependent on ρ_L , the length of the left branch l_L , the mass of a Cooper pair m_{CP} , the cross sectional area of the left branch S_L , and the Cooper pair charge q_{CP} squared. With photoabsorption the Cooper pair density in the exposed branch decreases and the kinetic inductance increases by ΔL_{LK} . The signal δI developed with photoabsorption in the left branch is calculated by taking the differential of Eq. 1 to obtain:

$$\delta I = \frac{\Delta L_{LK}}{(L_L + L_R)} \frac{I_0}{2} \quad (2)$$

The photoinduced signal δI depends on the QSKID geometry and quasiparticle lifetime and these are addressed below.

A. Detector Structure

With a serpentine geometry shown in Fig. 2 the performance of the QSKID is improved over the simple superconducting loop shown in Fig. 1. The improvements occur because for a given photon flux Ψ the change in ΔL_{LK} is larger and because improved isolation is achieved between the illuminated and masked branches

A serpentine geometry QSKID with N vertical segments in each branch, has the lengths of the left and right branches l_{SL} and l_{SR} increased about N times over a nonserpentine QSKID. For the QSKID in Fig. 2, $l_{SL} / l_L \approx 7$ and $l_{SR} / l_R \approx 7$. A similar scaling occurs for the left and right cross sectional areas S_{SL} and S_{SR} resulting in $S_{SL} / S_L \approx S_{SR} / S_R \approx 7$. Also the bias current I_0 decrease by a factor of 7, to provide a desirable reduction for operating integrated circuits. The serpentine geometry results in a significant increase in the kinetic inductance relative to the geometrical inductance. Combining all these factors, we calculate that for the serpentine QSKID under a given photon flux Ψ , the signal δI increases approximately 7 fold.

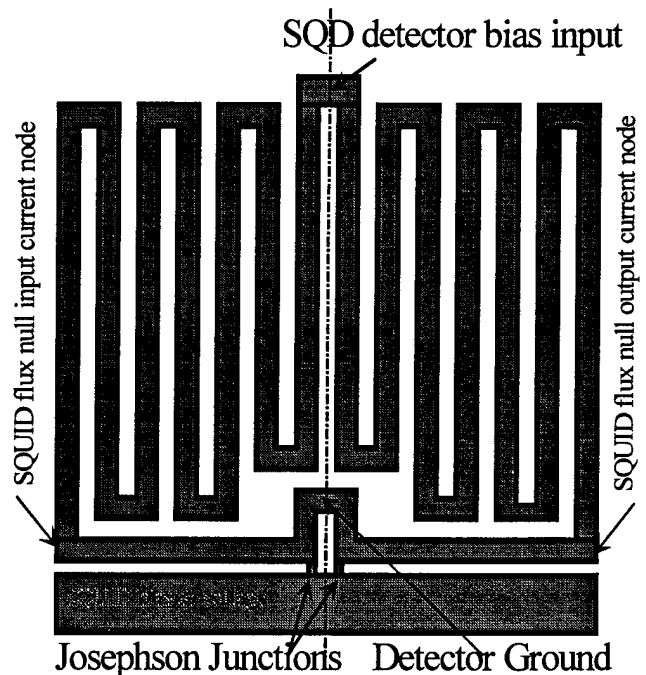


Figure 2. The YBCO superconducting quantum detector is shaped into a serpentine pattern with the directly coupled SQUID readout circuit located at the bottom. The photon flux only illuminates the left half of the serpentine patterned detector.

An additional benefit with the serpentine structure is interbranch isolation to maintain maximum signal. With photoillumination L_{LK} and the quasiparticle population increase. Interbranch quasiparticle and Cooper pair diffusion between the illuminated and the masked branches will reduce the signal. Interbranch diffusion is facilitated with quasiparticle having long lifetimes and this occurs by phonon trapping and low temperature operation. For YBCO, the quasiparticle diffusion length is estimated to be: $2\mu\text{m}$ for 1nsec, $10\mu\text{m}$ for 10nsec, and $60\mu\text{m}$ for 1μsec lifetimes respectively. These diffusion lengths are significant relative to the QSKID pixel size. A serpentine structure significantly increases the interbranch

path lengths and thereby resulting in improved interbranch isolation, i.e. less signal loss.

B. Detector's Photoresponse

Photoabsorption in the left branch of the serpentine QSKID in Fig. 2 produces a change in the inductance L_{1L} . The photoresponse is calculated in terms of the change in L_{1L} using the electrical equivalent circuit in Fig. 3. The equivalent circuit includes two loops each supplied with a DC current generator. The top loop, supplied by current I_0 , represents the serpentine detector structure. Below it, a second loop, supplied by a DC current I_{SQ} , represents the detector's SQUID readout circuit. Each inductor in the equivalent circuit includes: the self, the mutual, and the kinetic inductance terms associated with the structure in Fig. 2. The equivalent circuit is symmetrical and the left (right) side inductors and weak links are indicated by a subscript which includes the letter L (R).

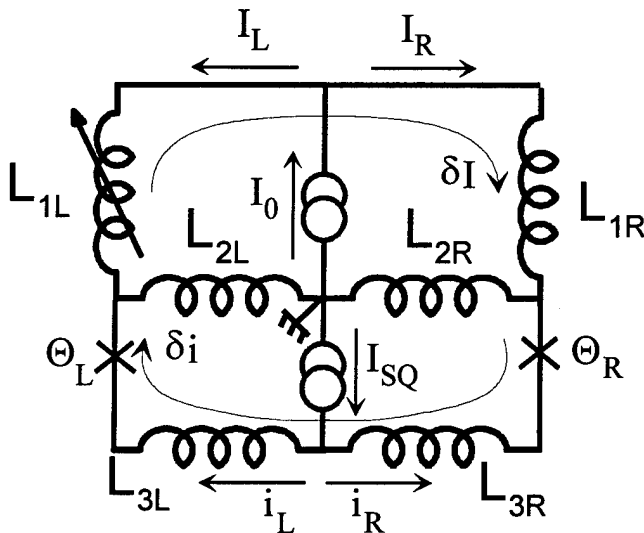


Figure 3. Equivalent circuit diagram for a directly coupled SQUID readout circuit to a YBCO superconducting quantum detector. There are two DC bias currents, one for the detector I_0 , and one for the SQUID readout device I_{SQ} .

The photoresponse is calculated by relating the photoinduced currents in the detector δI with the SQUID current δi . Before illumination, and under initial conditions, currents δI and δi are set equal to zero. Minimum energy conditions [5][6], represented by Eq. 1, yield the equilibrium conditions equation as:

$$I_L [L_{1L} + L_{2L}] + i_L L_{2L} = I_R [L_{1R} + L_{2R}] + i_R L_{2R} \quad (3)$$

The total SQUID loop inductance ($L_{2L} + L_{2R} + L_{3L} + L_{3R}$) is designed to be small to achieve good critical current modulation with flux. For QSKID with a large serpentine geometry results in $L_{1L} \gg L_{2L}$ and $L_{1R} \gg L_{2R}$. Therefore,

currents i_L and i_R are shunted to ground primarily through L_{2L} and L_{2R} , respectively, and we can neglect the flow of currents i_L and i_R through L_{1L} and L_{1R} . Integrating around the SQUID loop and requiring a zero or a multiple of 2π , the phase change, we obtain an equation for the SQUID under equilibrium conditions, i.e.

$$\begin{aligned} \frac{\Phi_0}{2\pi} \Theta_L + L_{3L} i_L + L_{2L} [I_L + i_L] = \\ \frac{\Phi_0}{2\pi} \Theta_R + L_{3R} i_R + L_{2R} [I_R + i_{LR}] \end{aligned} \quad (4)$$

Where Φ_0 is a fluxoid, Θ_L and Θ_R represent the phase shift across the left and right weak links.

With the application of a flux Ψ , photodepairing increases L_{1L} by δL and establishes new static conditions with currents δI and δi circulating in the detector and SQUID loops, respectively. Making the following substitutions in Eq. 3: $I_L = I_L - \delta I$, $I_R = I_R + \delta I$, $L_{1L} = L_{1L} + \delta L$, $i_L = i_L + \delta i$, $i_R = i_R + \delta i$, and keeping only first order terms, the nonequilibrium equation for the detector is:

$$\delta L I_L = \delta I [L_{1R} + L_{2R} + L_{1L} + L_{2L}] - \delta i [L_{2R} + L_{2L}] \quad (5)$$

Incorporating the same substitutions into Eq. 4 and keeping only the first order terms, the nonequilibrium equation for the SQUID becomes:

$$\begin{aligned} \frac{\Phi_0}{\pi} \delta \Theta + \delta i [L_{3R} + L_{3L} + L_{2L} + L_{2R}] \\ = \delta I [L_{2R} + L_{2L}] \end{aligned} \quad (6)$$

Eq. 5 is readily solved by recognizing that since $L_{1L} \gg L_{2L}$ and $L_{1R} \gg L_{2R}$ the last term can be neglected, and we obtain a solution similar to Eq. 2. Similarly, Eq. 6 is solved by recognizing that when operating in the voltage state, the leading term is the smallest since on average $\delta \Theta \approx 0$ and the phase angle across the weak link remains very close to $\pi/2$. Combining Eq. 5 and 6 we obtain a relationship between the SQUID and detector signal currents, specifically,

$$\delta i = \delta I \frac{[L_{2R} + L_{2L}]}{[L_{3R} + L_{3L} + L_{2L} + L_{2R}]} \quad (7)$$

The signal coupling efficiency between the QSKID's δI and the SQUID's δi is optimized by making the relative sizes of $[L_{3R} + L_{3L}] \ll [L_{2L} + L_{2R}]$. The detector

geometry, illustrated in Fig. 2, is designed for achieving a maximum coupling efficiency

The SQUID's voltage signal, produced by the QSKID's signal δI , is obtained from the RSJ model [7] [8] in the limit as the weak link's shunting capacitance C goes to zero. The SQUID's average output voltage signal δV , with weak links that each have an equivalent shunting resistance of R , is:

$$\delta V = \frac{\alpha R}{\sqrt{\alpha^2 - 1}} \frac{[L_{2R} + L_{2L}]}{[L_{3R} + L_{3L} + L_{2L} + L_{2R}]} \delta I \quad (8)$$

where $\alpha = I_{SQ}/2I_C$ and I_C is equal to the weak link's critical current. The sensitivity of the QSKID is examined next.

C. Detector's Sensitivity

Since the mechanism of HTS is not well understood, it is difficult to provide accurate predictions of static nonequilibrium phenomena in these materials. However, using the BCS model and the Rothwarf-Taylor equations, sensitivity predictions have been made. An extensive analysis has been made [9] [10] and here we shall only give highlights of these results

The noise in the QSKID, due to fluctuations in the Cooper pair population, is calculated to be much less than the Johnson noise in voltage state SQUID. The QSKID sensitivity is limited by: the current noise in the SQUID readout circuit. This noise can be minimized by using SQUIDS that have a smaller I_C and a larger loop inductance, but at the cost of noise rounding in the SQUID's I-V characteristics.

The photoresponse was modeled for Background (photon noise) Limited Infrared Performance (BLIP) where the photon noise is larger than the detector and readout circuit noises, added in quadrature. Hence, the ultimate performance level is achieved by minimizing the detector and the readout circuit noises. For BLIP, the photogenerated quasiparticle population needs to be larger than the thermal equilibrium quasiparticle population. Also, the detectors responsivity, dependent on the quasiparticle lifetime, needs to be maximized to overcome readout circuit noise. The δI is maximized by operating the detector at lower temperatures (30K e.g.) and utilizing phonon trapping to realize large effective quasiparticle lifetimes. In YBCO Pair Breaking (PB) phonon are trapped because anisotropy naturally confines the movement of PB phonons in the ab plane. Such phonon trapping is limited by anharmonic decay lifetime of PB phonons into non-pair breaking phonons.

We have calculated the BLIP sensitivity of a 100x100 μ m QSKID with a directly coupled SQUID readout circuit. The calculated sensitivity, for a 100 μ m square detector operating in a 30Hz bandwidth, in terms of Noise Equivalent Power is about 10^{-16} - 10^{-17} Watts. This calculated level of performance is limited by the detector's SQUID readout circuit. The QSKID projected spectral response is limited by the Cooper pair binding energy, predicted for YBCO to be about 30- μ m

III. CONCLUSIONS

A QSKID structure with a directly coupled SQUID readout circuit were described and the performance analyzed. The operation of this sensor structure is based on photoinduced changes in the QSKID kinetic inductance. A serpentine pattern is used for maximizing the photoresponse. The detectors sensitivity is limited by the current noise in the directly coupled SQUID readout circuit. The predicted BLIP NEP is 10^{-16} - 10^{-17} Watts with a cut-off wavelength between 30-40 μ m. The predicted performance makes the QSKID attractive and competitive particularly for detection at very long IR wavelength of cold objects.

IV. REFERENCES

- [1] J. G. Bednorz and K. A. Muller, "Possible high T_C superconductivity in the Ba-La-Cu-O system," *Z. Phys. B* vol. 64, pp 189-193, 1988.
- [2] Y. Enomoto and T. Murakami, "Optical detector using superconducting $BaPb_{0.7}Bi_{0.3}O_3$," *J. Appl. Phys.* vol. 59 No. 11, pp 3807-3814, 1986.
- [3] M. G. Forrester, M. Gottlieb, J. R. Gavaler, and A. I. Braginski, "Optical response of epitaxial and granular films of $YBa_2Cu_3O_{7.8}$ at temperatures from 25 and 100K," *IEEE trans. Magnet.* vol. 25, pp 1327-1330, 1989.
- [4] R. A. Smith, F. E. Jones, and R. P. Chasmar, *The Detection and Measurement of Infra-red Radiation*, Clarendon Press, Oxford 1958, pp 206-215.
- [5] N. Bluzer, "Multispectral superconducting quantum detector," U.S. Patent No. 5,179,072 (Jan. 12 1993) and 5,185,527 (Feb. 9, 1993).
- [6] N. Bluzer, and M. G. Forrester, "Superconducting quantum detectors" *J. Optical Engr.* vol. 33, No. 3, pp 697-703, March 1994; N. Bluzer and M. G. Forrester, "Superconducting quantum detectors in YBCO," *J. of Superconductivity*, vol. 7 No. 2, pp 395-398, 1994.
- [7] W. C. Stewart, "Current-voltage characteristics of Josephson junctions," *Appl. Phys. Lett.*, vol. 12, pp. 277-280, 15 April 1968.
- [8] D. E. McCumber, "Effects of ac impedance on the dc voltage-current characteristics of superconducting weak link junctions," *J. Appl. Phys.*, vol. 39, pp 3113-3118, June 1968.
- [9] N. Bluzer, "Quantum Superconducting Kinetic Inductance Detectors," unpublished.
- [10] A. V. Sergeev and M. Yu. Reizer, "Nonequilibrium Superconducting Detectors of Electromagnetic Radiation", unpublished.